LEVEL II

SYSTEMS, SCIENCE AND SOFTWARE

AD A093096

SSS-R-80-4216

A REVIEW OF AVAILABLE FREE-FIELD SEISMIC DATA FROM
UNDERGROUND NUCLEAR EXPLOSIONS IN ALLUVIUM, TUFF,
DOLOMITE, SANDSTONE-SHALE AND INTERBEDDED LAVA FLOWS

J. R. MURPHY
T. J. BENNETT

TOPICAL REPORT

DTIC

DEC 1 9 1980

SPONSORED BY

ADVANCED RESEARCH PROJECTS AGENCY   **A**
ARPA ORDER No. 2551

SEPTEMBER 1979

80 12 19 005

DDC FILE COPY

P. O. BOX 1620, LA JOLLA, CALIFORNIA 92038, TELEPHONE (714) 453-0060

AFTAC Project Authorization No. VT/9712/B/PMP

ARPA Order No. 2551, Program Code No. 6H189

Effective Date of Contract: November 17, 1978

Contract Expiration Date: September 30, 1979

Amount of Contract: $847,285

Contract No. F08606-79-C-0008

Principal Investigator and Phone No.
   Dr. Thomas C. Bache, (714) 453-0060, Ext. 337

Project Scientist and Phone No.
   Captain Michael J. Shore, (202) 325-7581

REPORT DOCUMENTATION PAGE		READ INSTRUCTIONS BEFORE COMPLETING FORM
1. REPORT NUMBER	2. GOVT ACCESSION NO. AD A093 096	3. RECIPIENT'S CATALOG NUMBER
4. TITLE (and Subtitle) A REVIEW OF AVAILABLE FREE-FIELD SEISMIC DATA FROM UNDERGROUND NUCLEAR EXPLOSIONS IN ALLUVIUM, TUFF, DOLOMITE, SANDSTONE-SHALE AND INTERBEDDED LAVA FLOWS.		5. TYPE OF REPORT & PERIOD COVERED Topical Report
		6. PERFORMING ORG. REPORT NUMBER SSS-R-80-4216
7. AUTHOR(s) J. R. Murphy T. J. Bennett		8. CONTRACT OR GRANT NUMBER(s) F08606-79-C-0008, ARPA Order - 2551
9. PERFORMING ORGANIZATION NAME AND ADDRESS Systems, Science and Software P.O. Box 1620 La Jolla, California 92038		10. PROGRAM ELEMENT, PROJECT, TASK AREA & WORK UNIT NUMBERS Program Code No. 6H189 ARPA Order No. 2551
11. CONTROLLING OFFICE NAME AND ADDRESS VELA Seismological Center 312 Montgomery Street Alexandria, Virginia 22314		12. REPORT DATE September, 1979
		13. NUMBER OF PAGES 143 154
14. MONITORING AGENCY NAME & ADDRESS(if different from Controlling Office)		15. SECURITY CLASS. (of this report) Unclassified
		15a. DECLASSIFICATION DOWNGRADING SCHEDULE

16. DISTRIBUTION STATEMENT (of this Report)

Approved for Public Release, Distribution Unlimited.

17. DISTRIBUTION STATEMENT (of the abstract entered in Block 20, if different from Report)

18. SUPPLEMENTARY NOTES

19. KEY WORDS (Continue on reverse side if necessary and identify by block number)

Seismology   Source Function
Nuclear Explosion
Ground Motion
Free-Field Observations

20. ABSTRACT (Continue on reverse side if necessary and identify by block number)

    This report summarizes the results of efforts to collect and organize the available free-field ground motion data from underground nuclear tests in alluvium, tuff, dolomite, sandstone-shale and interbedded lava flows. The primary objective of this effort has been to reformat the published data into a homogeneous form which will serve as a useful reference for researchers who are attempting to define theoretical seismic source functions for contained explosions in these media. (over)

DD FORM 1473 EDITION OF 1 NOV 65 IS OBSOLETE

388507

ABSTRACT (Continued)

The report describes the available free-field data for 13 events: the Fisher, Hognose, Haymaker, Merlin, Hupmobile and Packard events in alluvium; the Rainier, Mud Pack and Discus Thrower events in tuff; the Handcar event in dolomite; the Gasbuggy event in sandstone-shale; and the Milrow and Cannikin events in interbedded lava flows. Relevant geologic data is presented for each event to illustrate the environment of the ground motion measurements. The data presented include 53 RDP's: 14 for sources in alluvium, 24 for tuff, 11 for dolomite and 4 for sandstone-shale. However, some of these derived RDP's appear to be affected by secondary arrivals from media boundaries or have been developed from measurements within the strongly inelastic region and therefore may not accurately represent the radiated seismic field.

Free-field data from Handcar, Discus Thrower and Merlin are analyzed in greater detail in an effort to discern additional information about the seismic source characteristics of these events. As a result of these studies, the free-field data from the Handcar event are found to be consistent with low seismic coupling efficiency and the corresponding small cavity radius observed for the event. Data from Discus Thrower show little evidence of significant nonlinear effects which could arise from proximity of the source to the tuff-Paleozoic boundary. Late time, low frequency signals on the free-field records for Merlin are reasonably well explained as being caused by spall closure.

TABLE OF CONTENTS

LIST OF FIGURES

LIST OF TABLES

I. INTRODUCTION

Modeling the source of underground nuclear explosions in various emplacement media has been the subject of extensive research efforts. A primary control on explosive source models is their ability to accurately represent observed free-field ground motion. Unfortunately, these free-field ground motion data have not been easily accessible to the researcher because they are dispersed in a variety of reports. It is our objective to provide a summary of subsurface ground motion data from underground nuclear tests which is useful for researchers who are attempting to define the seismic source function for teleseismic compressional and surface waves. Murphy (1978) focused on the free-field data from tests emplaced in salt and granite; the current report summarizes the data from tests in tuff, alluvium, dolomite, sandstone-shale and interbedded lava flows.

As was the case in the previous effort (Murphy, 1978), the data presented here, with the exception of some recently derived reduced displacement potentials (RDP), have been extracted from the original post shot reports and other referenced publications and simply reformatted into a more homogeneous presentation which employs a single set of measurement units throughout. The report is primarily a data summary and interpretations of the observations in terms of particular source models have purposely been kept to a minimum.

Murphy (1978) identified the various parameters which are typically used to define the nuclear seismic source functions. He also summarized the assumptions underlying interpretation of free-field data and difficulties associated with its measurement. In this report we will draw upon these previous definitions and assessments; more detailed descriptions

1

of explosive source parameters and general considerations on interpretation of free-field data can be found in the previous report. In particular, where RDP's have been derived in this report, they were determined from

$$\phi \; (\tau) = r \; \alpha \; e^{-\frac{\alpha}{r}\tau} \int_{0}^{\tau} Z \; (n) \; e^{\frac{\alpha}{r}n} \; dn$$

where $\phi \; (\tau)$ is the RDP at retarded time $\tau = t - (r-r_{el})/\alpha$, r is radial distance from the source, r_{el} is the elastic radius, α is the propagation velocity of the compressional wave in the source medium, Z is the radial displacement and n is a dummy integration variable. The integral expression has been evaluated numerically for radial displacement time histories recorded at distances where it was thought infinitesimal strain theory might approximate the actual rheological conditions.

Section II summarizes the observed free-field data for six events in alluvium, three in tuff, two in interbedded lavas, one test in dolomite and one in a sequence of sandstone and shale layers. This section includes descriptions of the geometry of the experiments, the subsurface geology at the sites, observed peak ground motion data and reduced displacement potentials which have been derived for these events. A total of 220 peak ground motion measurements are presented. Fifty-three examples of computed reduced displacement potentials are shown; 29 of these had been previously published elsewhere and 24 were derived for the first time here. Table 1.1 summarizes the data which are presented. Forty-nine of the peak motion observations were for events emplaced in alluvium; 14 RDP's are shown for the alluvium events eight of which had not been previously published. Ninety of the peak motion observations are for a tuff emplacement medium;

2

TABLE 1.1

NUCLEAR EXPLOSION FOR WHICH FREE-FIELD
DATA ARE REPORTED

EVENT (DATE)	MEDIUM	YIELD** (KT)	DEPTH (M)	NO. OF RDP's
FISHER (12/3/61)	ALLUVIUM	12.4	363	3
HOGNOSE (3/15/62)	ALLUVIUM	L*	239	3
HAYMAKER (6/27/62)	ALLUVIUM	46	408	1
MERLIN (2/16/65)	ALLUVIUM	10	296	5
HUPMOBILE (1/18/68)	ALLUVIUM (DRY)	7.4	247	1
PACKARD (1/15/69)	ALLUVIUM (DRY)	10	247	1
RAINIER (9/19/57)	TUFF	1.7	274	3
MUD PACK (12/16/64)	TUFF	2.7	156	3
DISCUS THROWER (5/27/66)	TUFF (DRY)	21	338	18
HANDCAR (11/5/64)	DOLOMITE	12	402	11
GASBUGGY (12/10/67)	SANDSTONE/ SHALE	29	1292	4
MILROW (10/2/69)	PILLOW LAVA	~1000	1220	0
CANNIKIN (11/6/71)	PILLOW LAVA	~5000	1791	0

*L indicates yield in the range from 0 to 20 kt.

**Perret and Bass (1975).

24 RDP's, five of which were not previously published, are presented here. For the test in dolomite 40 peak motion measurements and 11 RDP's, none of which had been previously published, are presented. For the event emplaced in the sandstone-shale sequence, 12 peak motion measurements and four RDP's all previously published, are shown. Twenty-nine peak motion measurements are presented for two events emplaced in interbedded lava flows; no RDP's are available for these events. Regression relationships between the logarithms of peak motion parameters and logarithms of slant ranges were determined for events except when the data were so sparse that such determinations were precluded. In several cases these relationships are compared with previously published regression equations; but it should be noted that the regression equations which we show were derived from the data and do not represent simple conversions of the previously published equations to metric units. The peak motions enumerated above do not include all of the peak ground motion measurements identified in shot reports. The motions in the original reports frequently include data which is clearly contaminated by free surface effects or is in the strongly inelastic regime. We have attempted to separate such measurements in the data base; however, that information can still be found in this report where our regression relationships are compared with those from the original shot reports. As was the case in the previous report (Murphy, 1978), our primary emphasis here has been on ground motion measured near shot depth beyond the strongly inelastic region. We have taken a particle velocity of about a thousand cm/sec as a criterion for distinguishing the strongly inelastic region though this value would clearly depend on the source medium.

Section III focuses more detailed consideration on three of the nuclear tests: Merlin, Discus Thrower and Handcar. The "free-field" ground motion data from these events bear on some

4

important issues concerning the seismic source characteristics for underground nuclear explosions.

In particular, teleseismic data for the Handcar event which was emplaced in carbonate rock indicate that seismic coupling was below predicted levels for an event of that yield. The near-source, free-field seismic ground motions from Handcar have been analyzed, as described in Section III, to determine whether they are also indicative of low coupling. In this analysis the cavity radius and elastic radius for the explosion were estimated using the free-field data. By comparing the seismic source function for Handcar with that predicted for other source media we have been able to infer how the coupling anomaly is likely to behave for events of higher yield in similar media.

The source region for the Discus Thrower event was rather strongly layered with the boundary between the tuff and Paleozoic rocks located only about 60 m below the shot. It was anticipated that the ground motion records near shot depth from Discus Thrower would reveal any nonlinear effects or source asymmetry due to proximity to such interfaces. In Section III we describe studies of elastic wave propagation which we performed using a geologic model of the Discus Thrower site region. We have sought to determine the degree to which this elastic wave propagation model can explain the observed "free-field" ground motions and thereby reveal any nonlinear behavior. In the course of this study, we have tentatively identified the free surface reflection, pP, on the ground motion records near shot depth.

Free-field ground motions from the Merlin event are important because they contain a relatively low frequency signal which appears to be related to spall. In the past seismic signals generated by spall closure observed near the explosion

5

source have been restricted to accelerograms recorded in close proximity to the spall plate. These signals appear as high frequency spikes and therefore their contribution to our understanding of the teleseismic waves generated by spall closure is minimal. The late time signals observed at shot depth for the Merlin event are in the passband of normal teleseismic observations (1 to 2 Hz) and therefore are potentially significant to our understanding of spall closure as a seismic source. In Section III we describe efforts to provide a more definitive identification of the late time, low frequency signal observed in the Merlin event. We have used an analytical model of spall closure to investigate whether such a model can adequately explain the observed signal.

II. MEASURED FREE-FIELD DATA FROM EXPLOSIONS IN ALLUVIUM, TUFF, DOLOMITE, SANDSTONE-SHALE AND INTERBEDDED LAVA FLOWS

2.1 Overview

In this chapter the free-field data from the nuclear tests shown in Table 1-1 will be reviewed and summarized. The data are discussed in the order shown in Table 1.1 with the alluvium events first, the tuff events second, next the test in dolomite, followed by that emplaced in the sandstone-shale sequence, and finally the two events in the interbedded lava flows. Where necessary, the originally reported data were converted to a common system of units: range and depth in meters, peak particle accelerations, velocities and displacements in g, cm/sec and cm respectively; and RDP's in m^3. For each event the following information is provided: (1) a surface map of the site showing the geometry of the experiment, (2) a vertical section through the detonation point showing the relationship between the instrument location and the local subsurface geology, (3) displays of the free-field peak motion data and (4) displays of the currently available RDP's which have been derived from the measured ground motion data. It should be noted that the RDP's shown below have in many cases been redrafted and may not be suitable as input to digital processing. However, enough care has been taken in their reproduction to insure that the rise time, peak amplitude and steady state amplitude are accurate to within a few percent.

2.2 Fisher

The Fisher event was a 12.4 kt contained explosion which was detonated at a depth of 363 m ($h/W^{\frac{1}{3}} = 157$ m/kt$^{\frac{1}{3}}$) in alluvium (disintegrated tuff) at the Nevada Test Site (NTS) on December 3, 1961. Fisher was the first in a series of three events reported here located in the same area and utilizing several of the same

ground motion instruments. Other events in the series were Hognose and Haymaker. Ground motion measurements for Fisher were made at shot depth in four drill holes. Instruments at the bottom of each hole included accelerometers and velocity gages oriented to respond to radial motion. The four stations covered a distance range from 92 to 549 m and were the responsibility of Sandia Corporation (Perret, 1965). Recorded acceleration levels were generally lower than the range predicted resulting in low signal-to-noise ratios and negating the usefulness of the radial acceleration measurements. This was attributed to more rapid attenuation of the acceleration in the disintegrated tuff emplacement media over what had been predicted assuming more competent rock at shot depth. Radial particle velocity measurements were apparently not so severely affected by this difference in media and therefore provided records with good signal-to-noise ratios at the four stations. Displacements were derived by integrating these velocities.

Figure 2.1 is a surface map of the site (Perret, 1965) showing the locations of the instrument holes relative to ground zero. Figure 2.2 shows the location of the stations on a vertical plane through the shot point. An approximate subsurface geologic profile is shown on the left side of the figure and consists of a simple alluvium medium extending from the surface to below shot depth. The compressional velocity in the alluvium is taken to be equal to the propagation velocity determined for first signal arrivals on the shot-depth stations (Perret, 1965). Propagation velocities to stations at the ground surface are somewhat lower indicating that compressional velocities nearer the surface are lower. The velocity and density are typical of those for alluvium at NTS.

The available peak radial ground motions for the Fisher event are shown in Figure 2.3. Because of the low signal-to-noise for the acceleration data, only a single measurement was available so that no regression could be performed. Regressions

8

N

100 m

STATION 8 ◯

GROUND ZERO ●

STATION 6 ◯

STATION 4 ◯

◯ STATION 2
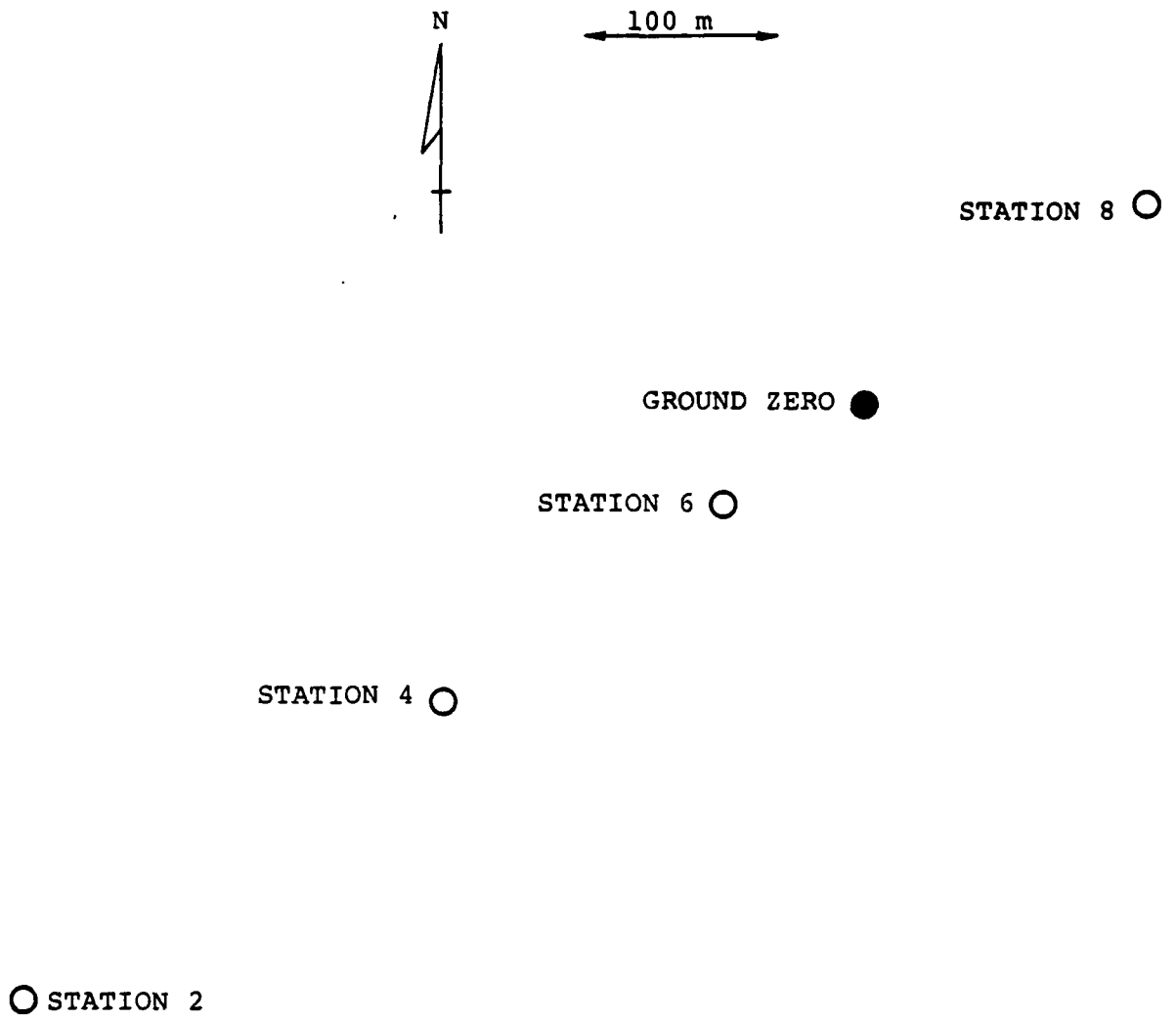
Figure 2.1 Surface Map of the Fisher Site.

Figure 2.2 Vertical Section Through the Fisher Detonation Point Showing the Relationship Between the Instrument Locations and the Subsurface Geology at the Site.
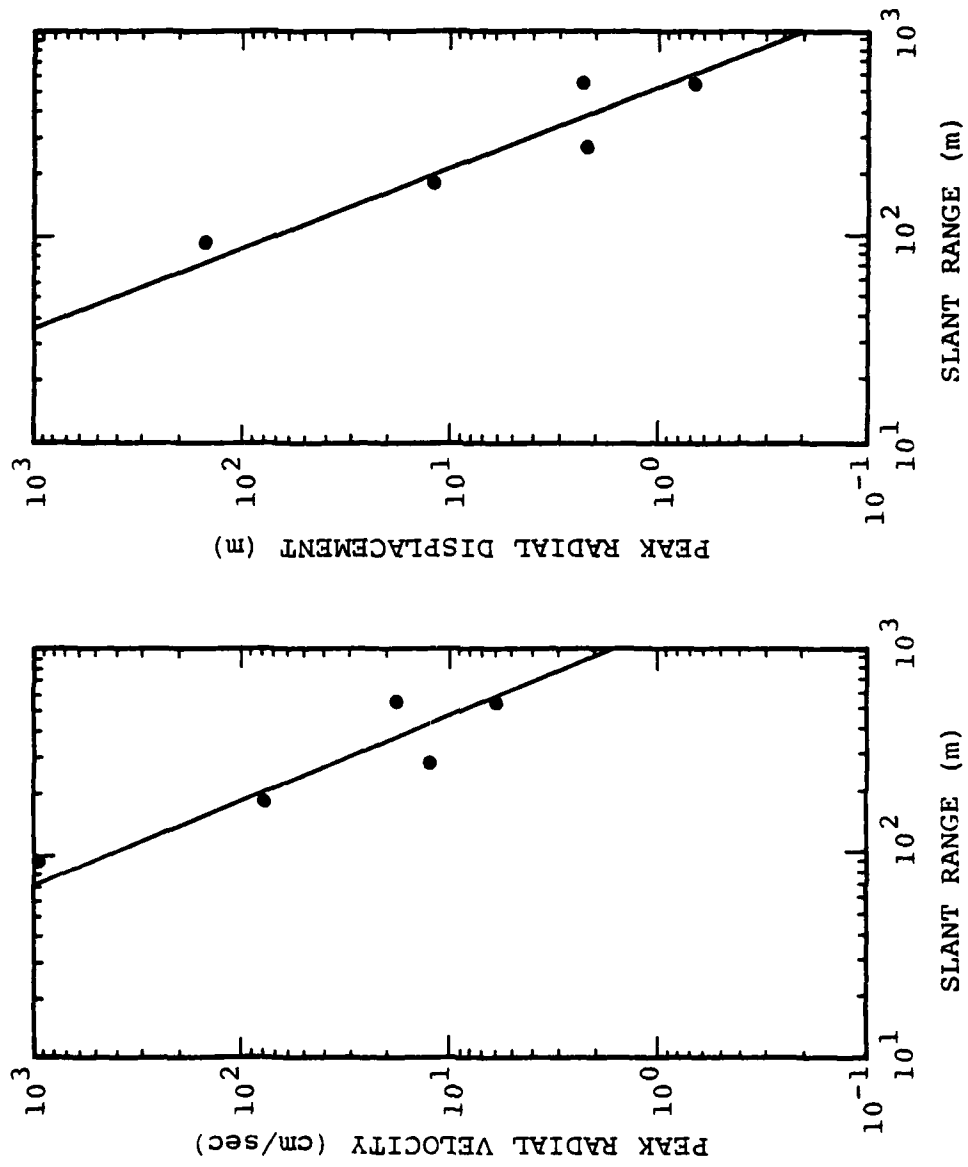
Figure 2.3 Observed Fisher Peak Motion Data as a Function of Range.

11

were performed on the peak radial velocities and displacements. These resulted in

$$v_r = 3.02 \times 10^7 \; R^{-2.42}$$

for radial velocity, v_r, in cm/sec, R in meters and

$$d_r = 8.51 \times 10^6 \; R^{-2.55}$$

for radial displacement, d_r, in cm. Perret (1965) scaled all the peak motion data from the Fisher, Hognose and Haymaker series of events by dividing all ranges by the cube root of the yield, multiplying peak accelerations by the cube root of the yield and dividing peak displacements by the cube root of the yield. He performed independent regressions on the data for scaled ranges less than about 105 m/kt$^{\frac{1}{3}}$ and for scaled ranges greater than 105 m/kt$^{\frac{1}{3}}$. These resulted in

$$a_r \cdot W^{\frac{1}{3}} = 2.24 \times 10^9 \; (R/W^{\frac{1}{3}})^{-4.5}$$

$$v_r = 8.50 \times 10^8 \; (R/W^{\frac{1}{3}})^{-3.75}$$

$$d_r/W^{\frac{1}{3}} = 3.55 \times 10^7 \; (R/W^{\frac{1}{3}})^{-3.66}$$

for $(R/W^{\frac{1}{3}})$ less than 105 m/kt$^{\frac{1}{3}}$ and

$$a_r \cdot W^{\frac{1}{3}} = 7.95 \times 10^3 \; (R/W^{\frac{1}{3}})^{-1.9}$$

$$v_r = 1.07 \times 10^4 \; (R/W^{\frac{1}{3}})^{-1.32}$$

$$d_r/W^{\frac{1}{3}} = 9.69 \times 10^2 \; (R/W^{\frac{1}{3}})^{-1.39}$$

for $(R/W^{\frac{1}{3}})$ greater than 105 m/kt$^{\frac{1}{3}}$ where a_r is radial acceleration in g's, v_r is radial velocity in cm/sec, d_r is radial displacement in cm and W is yield in kilotons.

Presumably the higher attenuation rate at scaled range less than 105 m/kt$^{\frac{1}{3}}$ is indicative of the strongly inelastic regime for the alluvium emplacement medium. For the Fisher event this range would be 243 m. Such a distinction based on the Fisher data alone is not obvious as can be seen from Figure 2.3. Thus our regression equations which neglected this distinction tend to have slopes intermediate between those which Perret (1965) identifies for the larger, scaled data base.

Werth and Herbst (1962) published a RDP developed from the radial displacement for the Fisher event recorded at a range of 183 m. This RDP is shown in Figure 2.4. We also computed a RDP from the Gage 8 displacement time history recorded at a range of 183 m. Comparison of these two RDP's in Figure 2.4 indicates a close match from $\tau = 0$ out to $\tau = .6$ sec. Beyond that time additional signals appear on the RDP which we derived; these arrivals appear to have been smoothed out in the RDP presented by Werth and Herbst. Perret (1965) attributed secondary arrivals to oscillations of gases within the explosion cavity. It also appears that the RDP continues to show some decay in amplitude out to beyond $\tau = 2.0$ sec. As noted above the attenuation studies by Perret (1965) suggest that Gage 8 is within the nonlinear regime - i.e. R < 243 m. We computed a RDP from the radial displacement recorded on Gage 4 at a range of 274 m. This RDP is considerably lower in amplitude than that at 183 m though the shape is similar.

2.3 Hognose

Hognose was a low (L) yield contained explosion which was detonated at a depth of 239 m in alluvium at NTS on March 15, 1962. The instrumentation was the same as that for Fisher except the source for Hognose was located at a different position along the line of stations and was also emplaced at a
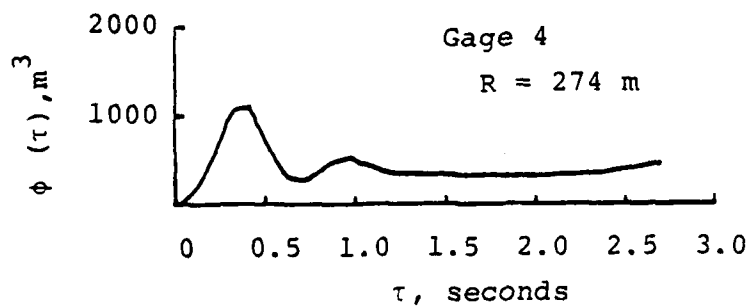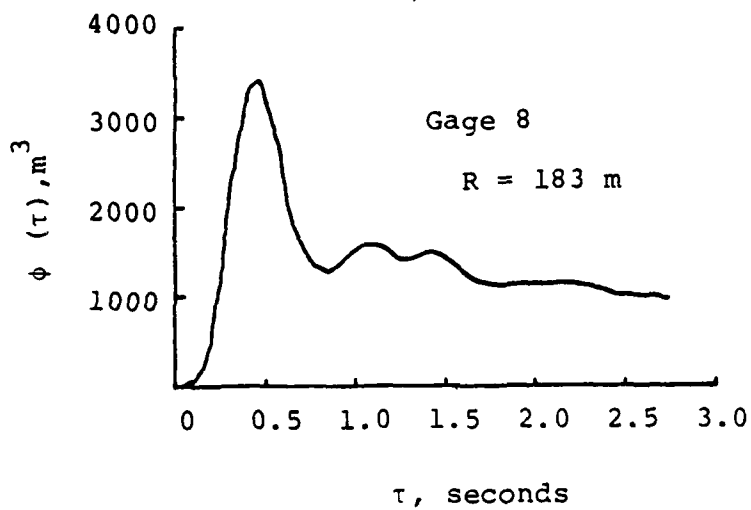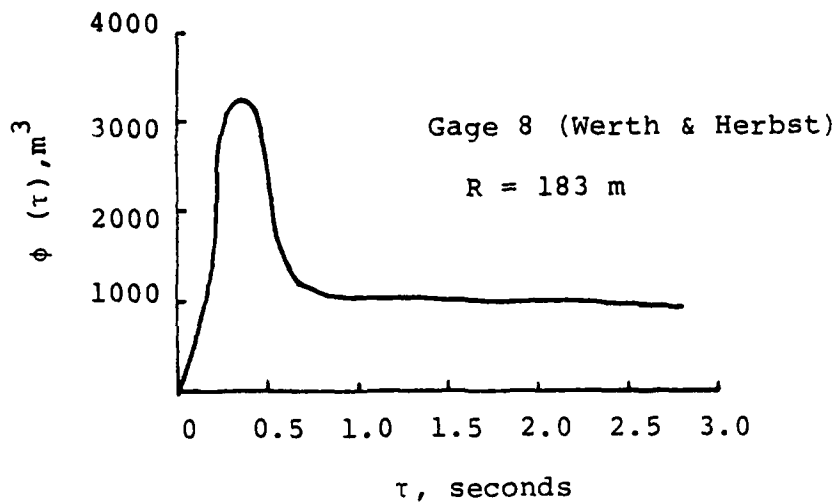
Figure 2.4   Observed Fisher Reduced Displacement Potentials
Gage 8 (simplified after Werth & Herbst), Gage
8 and Gage 4.

shallower depth in the alluvium section. The four stations covered a range from 152 to 562 m and were the responsibility of Sandia Corporation (Perret, 1965). Good signals were recorded on all gages. Velocities were obtained directly from velocity gages and also by integrating the accelerometer records. Displacements were computed by integrating the velocity records and doubly integrating the accelerometer records.

Figure 2.5 is a surface map of the site (Perret, 1965) showing the locations of the instrument holes relative to ground zero. Figure 2.6 shows the locations of the stations on a vertical plane through the shot point. An approximate subsurface geologic profile is shown on the left side of the figure and is essentially the same as that for Fisher except the velocity and density of the emplacement medium are taken to be somewhat lower in the case of Hognose reflecting its shallower depth of burial. These lower values are consistent with the propagation velocities for Hognose determined from the first arrivals.

The available peak radial ground motions for the Hognose event are shown in Figure 2.7. Values shown in this figure have been corrected to a radial vector motion to account for differences in elevation between the shot and instruments. This correction was accomplished by assuming the observed component of motion to be the projection of the radial vector motion onto the axis of the measurement. Regressions were performed on these corrected values for peak radial accelerations, velocities and displacements. These resulted in

$$a_r = 1.95 \times 10^6 \, R^{-2.67}$$

$$v_r = 3.72 \times 10^4 \, R^{-1.39}$$

$$d_r = 1.26 \times 10^4 \, R^{-1.56}.$$

15

100 m

N

STATION 8 ◯

STATION 6 ◯

STATION 4◯

● GROUND ZERO

◯ STATION 2

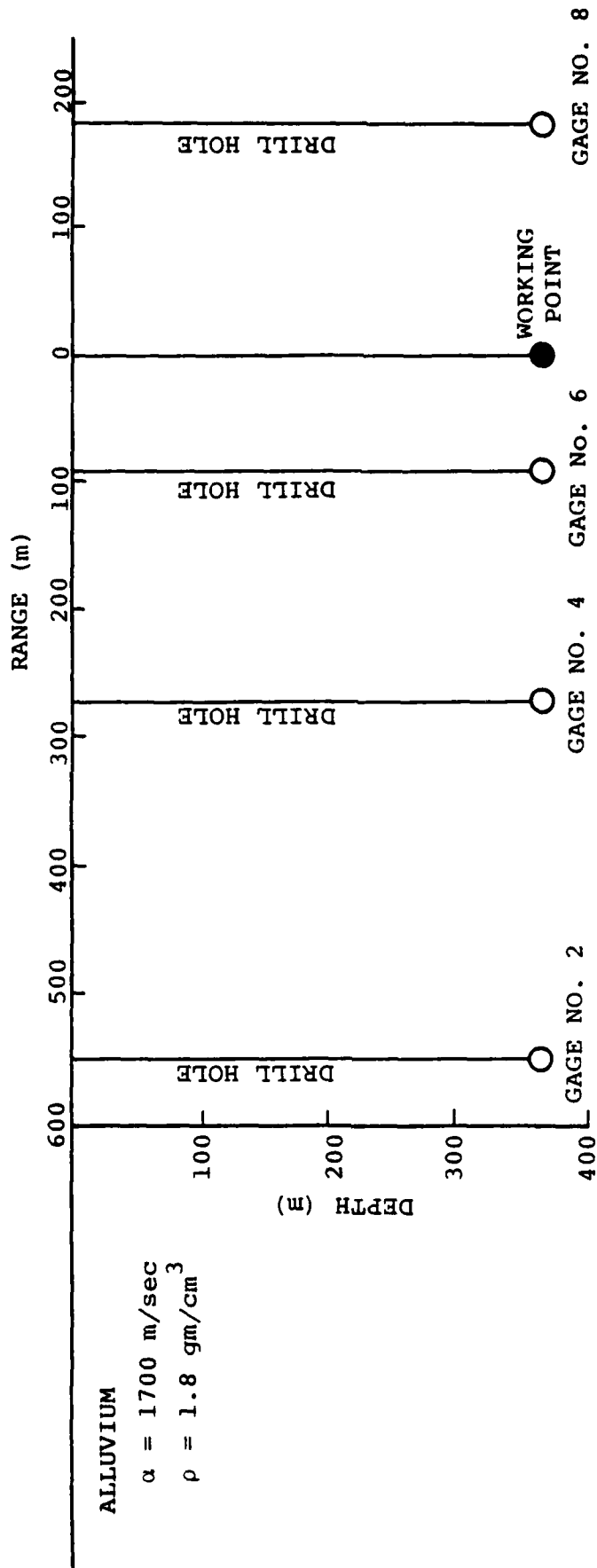Figure 2.5   Surface Map of the Hognose Site.

Figure 2.6 Vertical Section Through the Hognose Detonation Point Showing the Relationship Between the Instrument Locations and the Subsurface Geology at the Site.

17
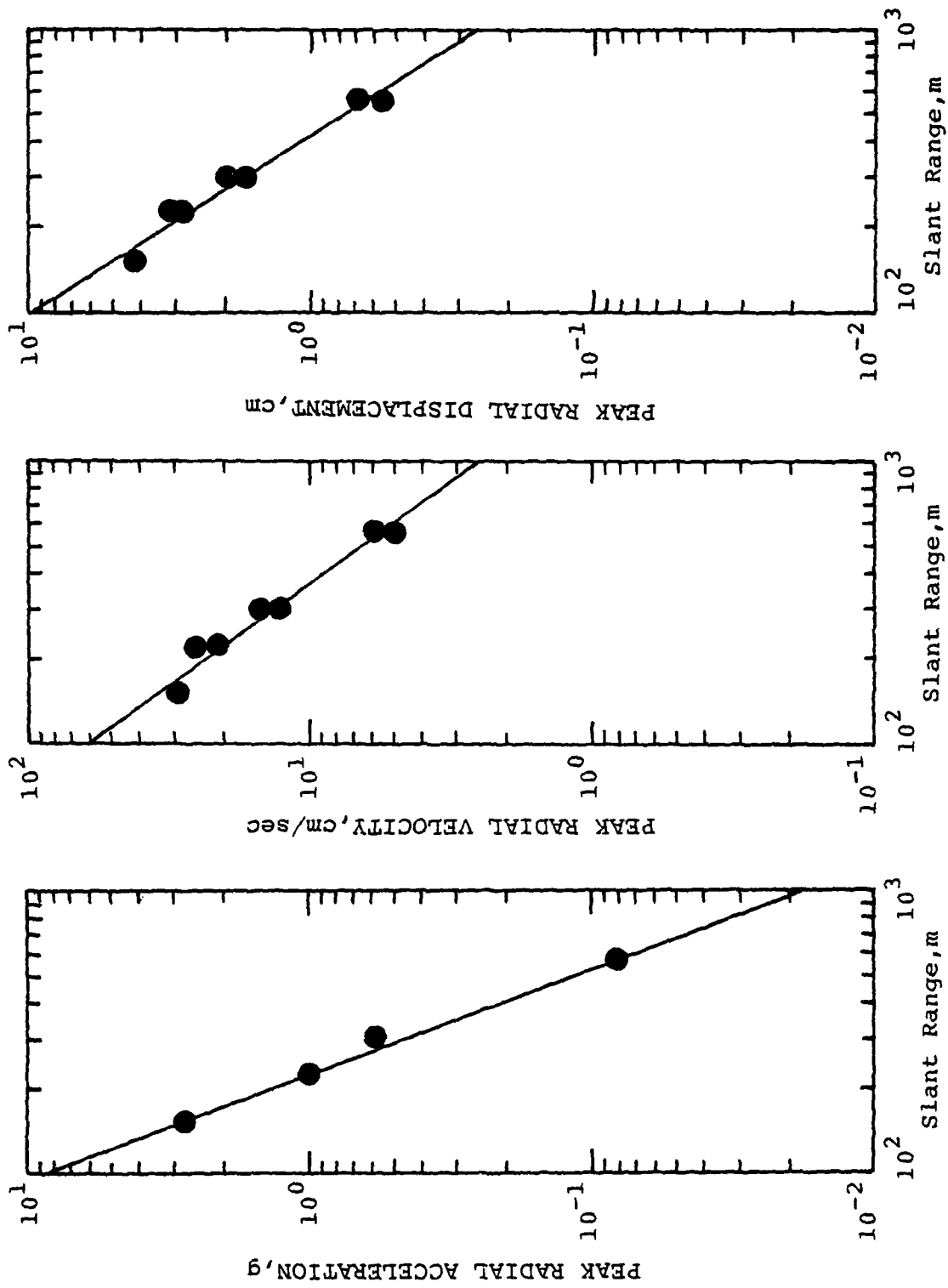
Figure 2.7 Observed Hognose Peak Motion Data as a Function of Range.

18

Again the slopes of the attenuation relationships derived for the Hognose data appear to be intermediate between those which Perret (1965) derived for short and far distance ranges using the larger, scaled data base. In this case, the slopes appear to be closer to those for the more distant data group suggesting that most of the Hognose measurements shown in Figure 2.7 were obtained outside the strongly inelastic region.

We derived three RDP's from the radial displacement time histories for the Hognose event. These were for ranges of 152 m, 219 m and 300 m and are shown in Figure 2.8. It should be noted that the displacements used to compute these RDP's were not corrected to the radial vector motion as described above. This accounts, at least in part, for the low amplitude of the RDP at 152 m relative to that for the other two stations (i.e. applying ьne same projection correction used for the peak motions increases the amplitude of the Gage 4 RDP by about a factor of 1.5 relative to the other two). The RDP's after about .5 seconds also appear to be contaminated somewhat by additional arrivals. The large arrival near $\tau = 1$ sec on the RDP for Gage 6, which also may be present to some degree on the other two RDP's, is similar in appearance to late time arrivals identified below for the Merlin event and may be associated with spall closure. Note that the general character of the Gage 4 and Gage 2 RDP's shown here are quite similar to that of the Fisher RDP's shown in Figure 2.4.

2.4 Haymaker

The Haymaker event was a 46 kt contained explosion which was detonated at a depth of 408 m ($h/W = 114$ m/kt$^{\frac{1}{3}}$) in alluvium (disintegrated tuff) at NTS on June 27, 1962. The instrumentation was again similar to that for Fisher except that the source was emplaced deeper in the alluvium section and only two stations recorded the ground motion at depth. The two stations were the

19
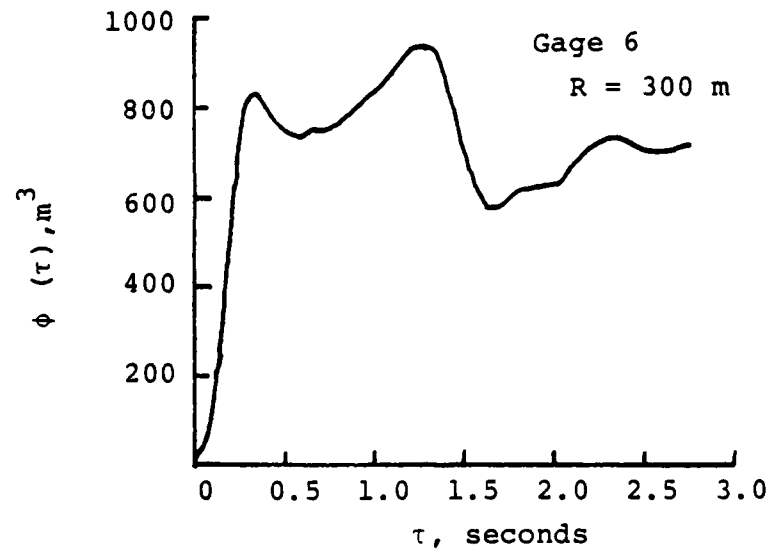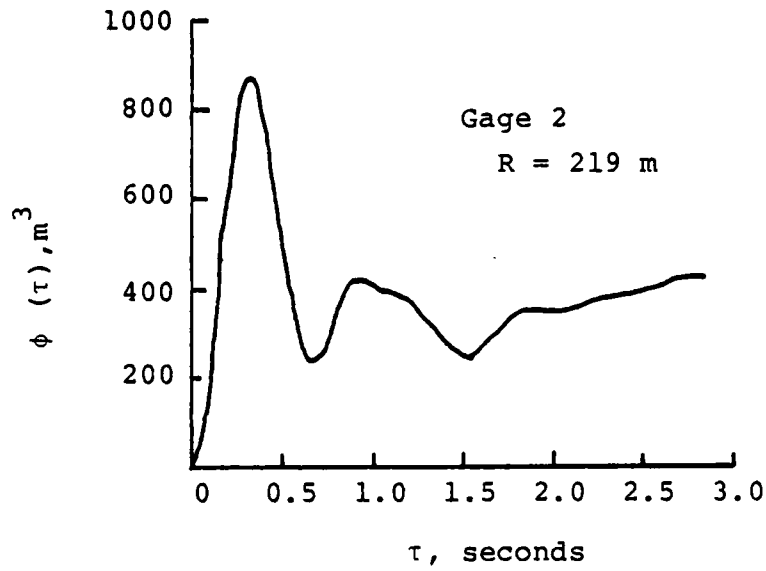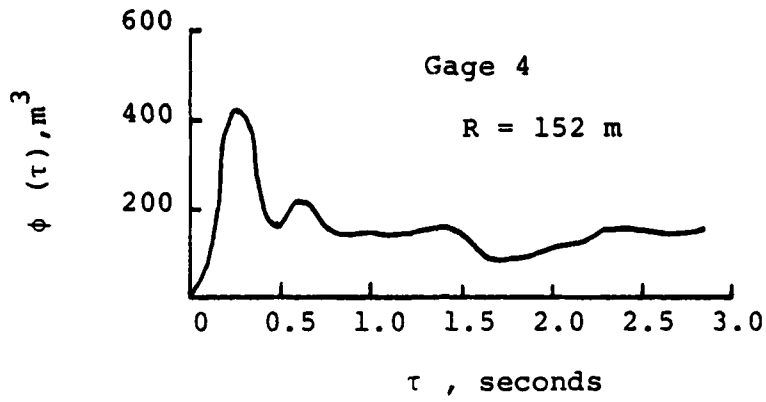
Figure 2.8   Observed Hognose Reduced Displacement Potentials
Gages 4, 2 and 6.

responsibility of Sandia Corporation (Perret, 1965) and were at
ranges of 278 and 550 m. No accleration data was obtained at
the 550 m station. Velocity measurements were obtained directly
and by integrating the acceleration time histories and displace-
ments were obtained by integrating the velocity records and
doubly integrating the acceleration records.

Figure 2.9 is a surface map of the site (Perret, 1965)
showing the locations of the instrument holes relative to ground
zero. Figure 2.10 shows the locations of the stations on a
vertical plane through the shot point. An approximate subsur-
face geologic profile is shown on the left side of the figure
and is taken to be the same as that for Fisher.

The available peak radial ground motion data for the
Haymaker event are shown in Figure 2.11. The correction to
radial vector motion to account for differences in elevation
between the shot and instruments is only about one percent or
less. No regression could be performed on the acceleration
data. Regressions on the three velocity and displacement data
points resulted in:

$$v_r = 2.29 \ R^{-.21}$$

$$d_r = 1.91 \times 10^8 \ R^{-2.88} \ .$$

Little reliance can be placed on these curves because of the
paucity of data.

We derived a RDP from the displacement time history re-
corded at a range of 278 m; this is shown in Figure 2.12. In
general, the shape of this RDP is similar to that derived for
Fisher. In fact, if the Fisher RDP from Gage 8 is scaled to
the Haymaker yield assuming a direct linear relationship between
RDP amplitude and yield, the scaled RDP would tend to over-
estimate the peak in the RDP observed for Haymaker by only about
30% and slightly underestimate the late time RDP level. On the

21

N

|← 100 m →|

STATION 4 ○

STATION 2 ○

● GROUND
  ZERO

Figure 2.9   Surface Map of the Haymaker Site.

RANGE (m)

100   200   300   400   500   600

DEPTH (m)

100
200
300
400
500

WORKING
POING

GAGE NO. 2

GAGE NO. 4

ALLUVIUM

α = 1700 m/sec

ρ = 1.8 gm/cm^3

Figure 2.10   Vertical Section Through the Haymaker Detonation Point Showing the Relation-
ship Between the Instrument Locations and the Subsurface Geology at the Site.

23
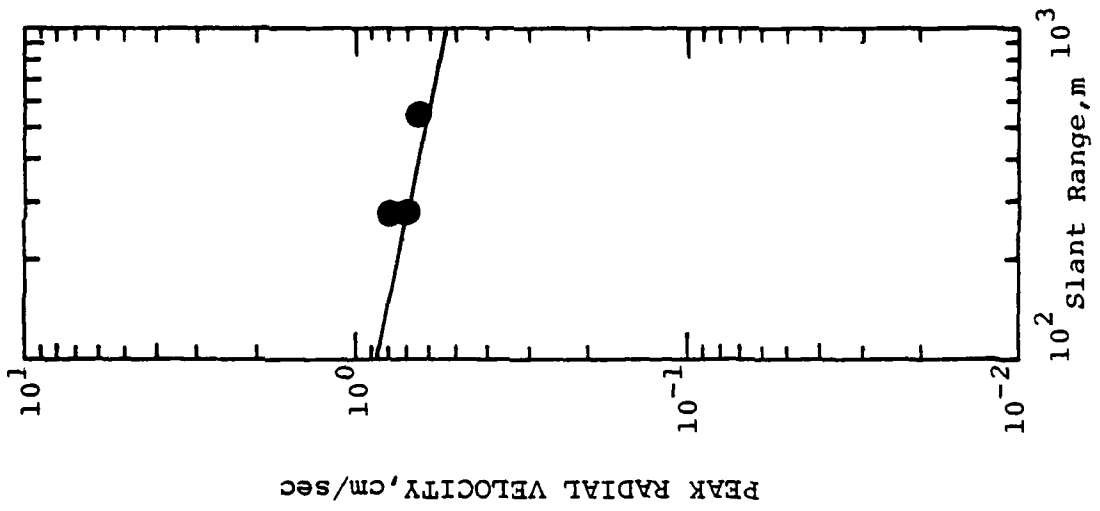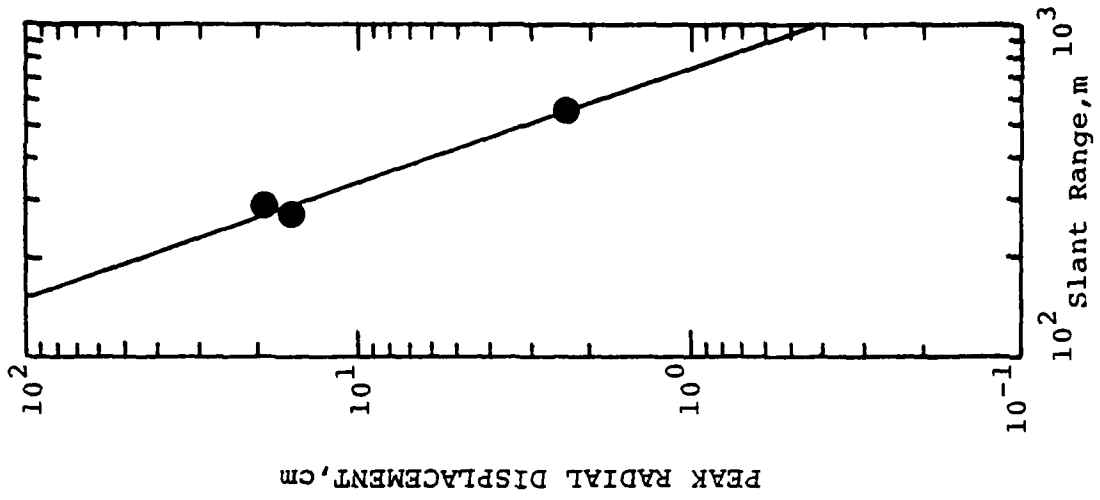
Figure 2.11 Observed Haymaker Peak Motion Data as a Function of Range.
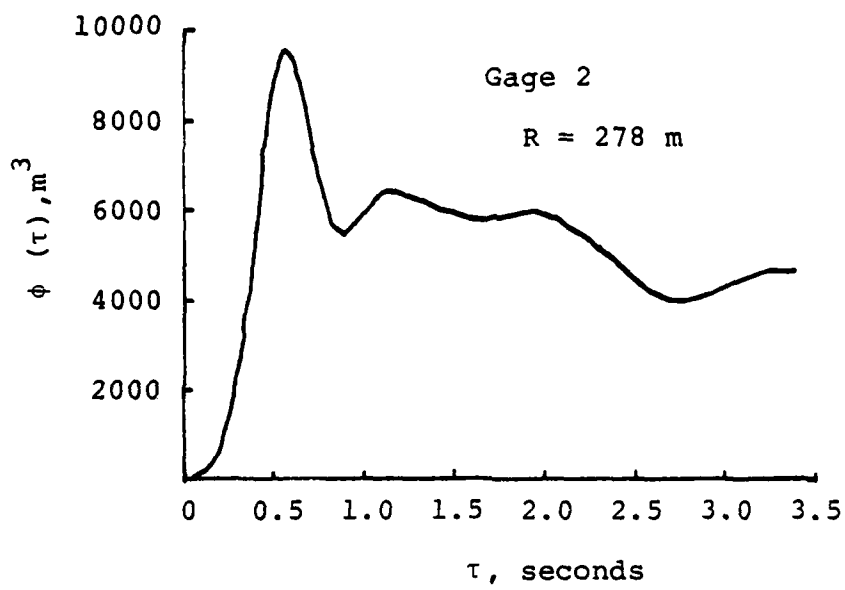
Figure 2.12 Observed Haymaker Reduced Displacement
Potential Gage 2.

other hand, if we scale the Fisher RDP from Gage 4 to the Haymaker yield, it substantially underestimates the observed Haymaker RDP at all times. It should be noted that the derived Haymaker RDP, like that for Fisher Gage 8, was obtained at a range which Perret (1965) identifies to be inside the zone of higher attenuation associated with strongly inelastic behavior; for the Haymaker yield this zone would extend to 376 m. However, the scalability of the Fisher and Haymaker data may be an indication that the radius of this zone is actually somewhat smaller than that estimated by Perret.

2.5 Merlin

The Merlin event was a 10 kt contained explosion which was detonated at a depth of 296 m ($h/W^{\frac{1}{3}} = 137$ m/kt$^{\frac{1}{3}}$) in alluvium at NTS on February 16, 1965. Ground motion measurements for Merlin were made at shot depth in five drill holes. The instruments at the bottom of the four holes nearest the shot were accelerometers and velocity gages oriented to respond to radial motion. The instrument at the bottom of the hole furthest from the shot was an accelerometer oriented to respond to radial motion. The instruments covered a distance range from 107 to 763 m and were the responsibility of Sandia Corporation (Perret, 1971). Only the accelerometer closest to the source failed to provide useful data. For the other stations velocities and displacements were derived by performing the appropriate integrations of the acceleration and velocity time histories.

Figure 2.13 is a surface map of the site (Perret, 1971) showing the locations of the instrument holes relative to ground zero. Figure 2.14 shows the locations of the stations on a vertical plane through the shot point. An approximate subsurface geologic profile is shown on the left side of the figure and consists of a simple alluvium medium extending from ground surface to below shot depth. A somewhat higher velocity material,

26

STATION U7 ◯   N   ◄── 100 m ──►

STATION U6 ◯

STATION U5◯

STATION U4 ◯

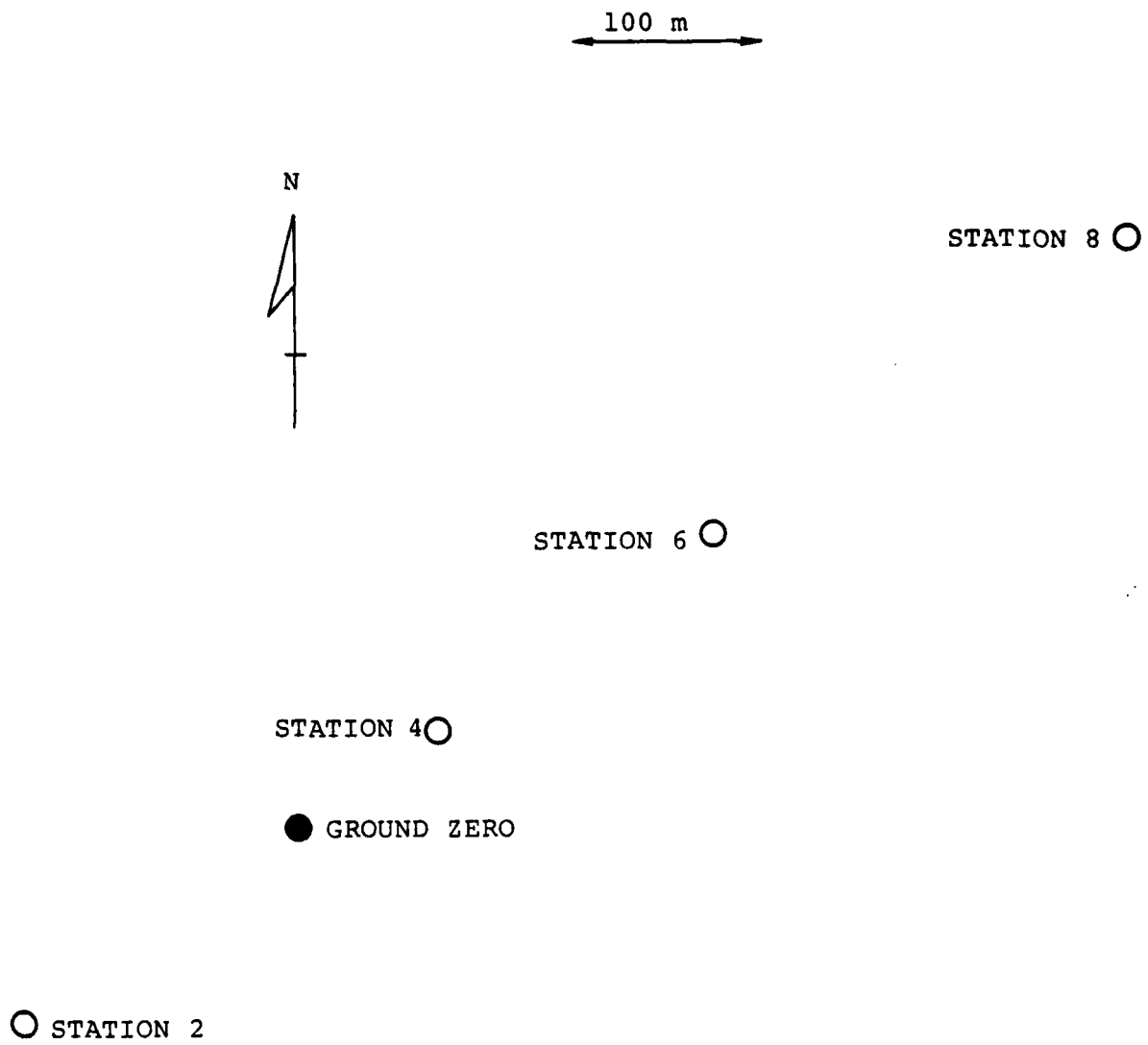STATION U3 ◯

● GROUND ZERO

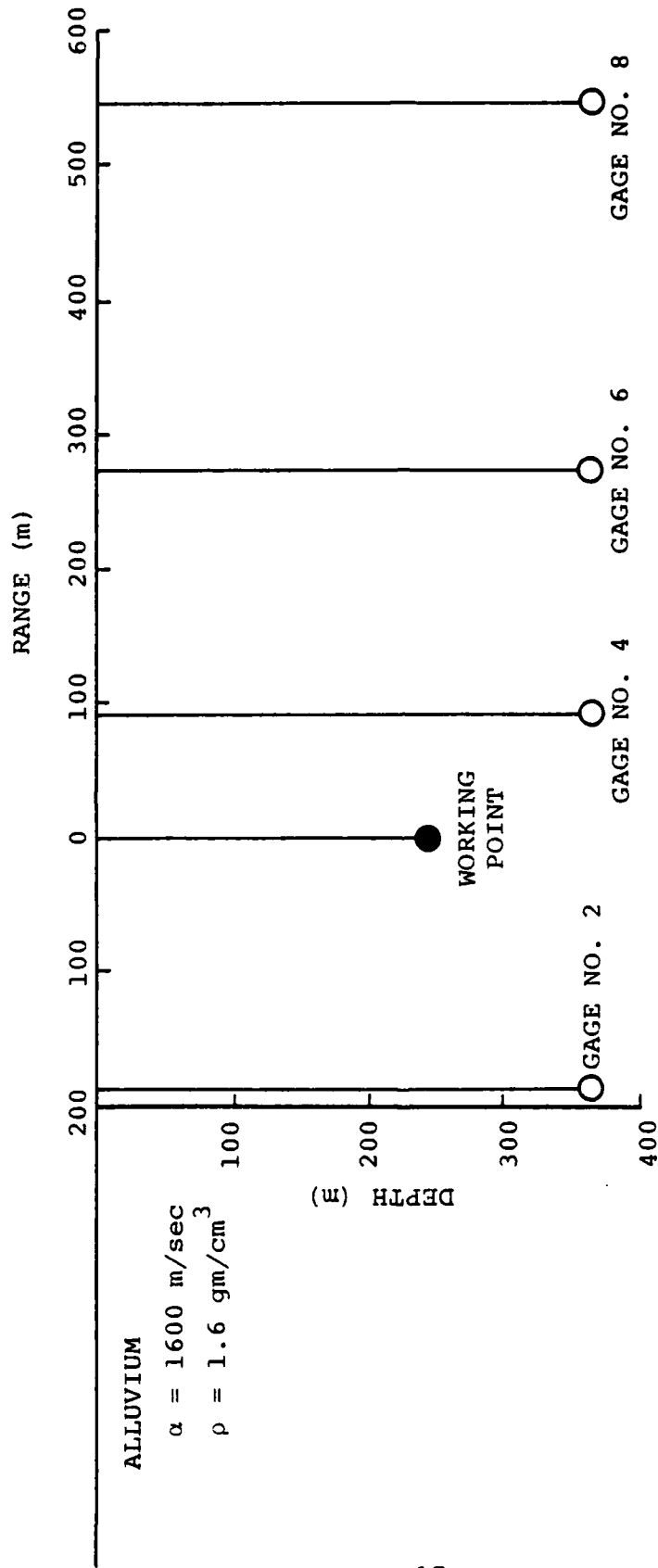Figure 2.13 Surface Map of the Merlin Site.
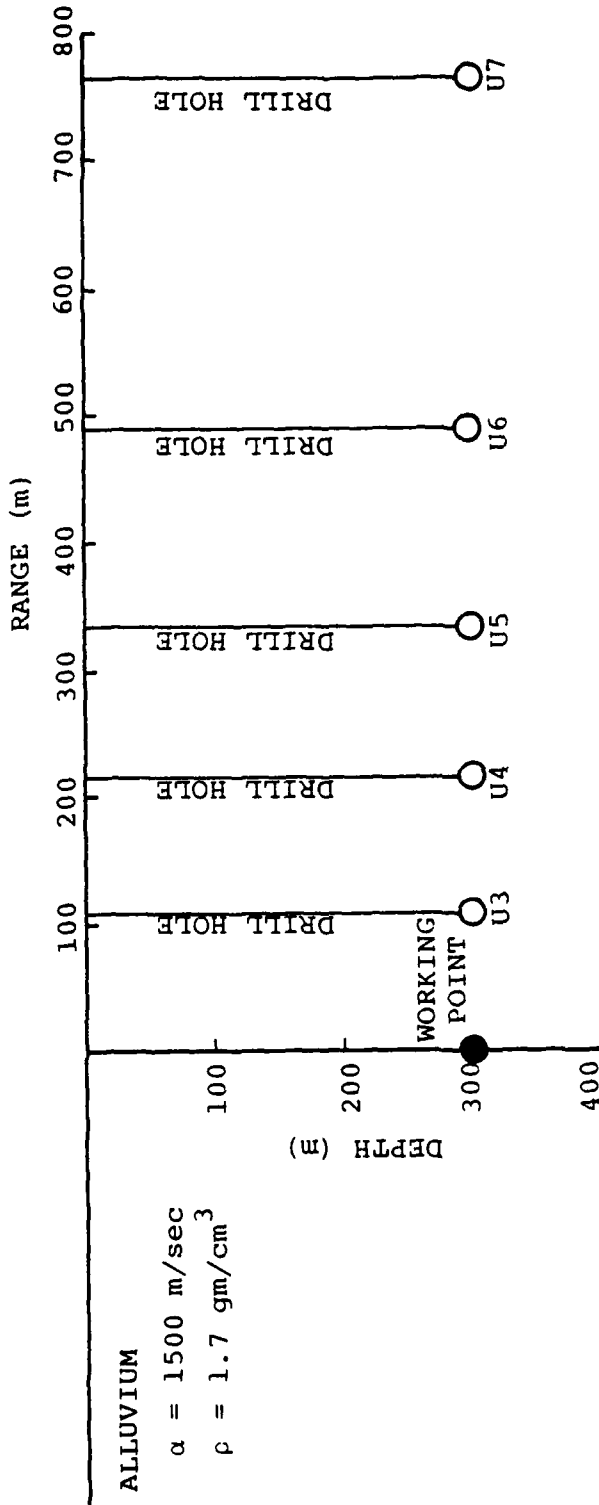
Figure 2.14 Vertical Section Through the Merlin Detonation Point Showing the Relation-ship Between the Instrument Locations and the Subsurface Geology at the Site.

28

apparently unwelded tuff is present 58 m below shot depth. The compressional velocity was estimated from the propagation velocity determined for first signal arrivals on the shot-depth stations (Perret, 1971). Propagation velocities to stations above shot depth and on the surface indicate a decrease in compressional velocity nearer the surface. The observed velocity and density are typical of those for NTS alluvium.

Available peak radial motion for the shot-depth stations from the Merlin event are shown in Figure 2.15. Regressions were performed on the peak radial motion data; these resulted in:

$$a_r = 8.71 \times 10^4 \ R^{-2.08}$$

$$v_r = 3.98 \times 10^4 \ R^{-1.39}$$

$$d_r = 1.91 \times 10^4 \ R^{-1.55}$$

Perret included data from above the shot in his regression analyses of acceleration data (cf. Figure 2.16). For the elastic precursor his analysis after converting to metric units gives

$$a = 7.27 \times 10^4 \ R^{-2.02}.$$

For peak velocities Perret performed a regression analysis on the shot level data (Figure 2.16) resulting in

$$v = 4.10 \times 10^4 \ R^{-1.39}.$$

For peak displacements Perret included data from above the shot (cf. Figure 2.16) as well as measurements of secondary peaks in his regression. The resulting relation is:

$$d = 1.26 \times 10^7 \ R^{-2.64}$$

where d is in cm and R is in m. The acceleration and velocity
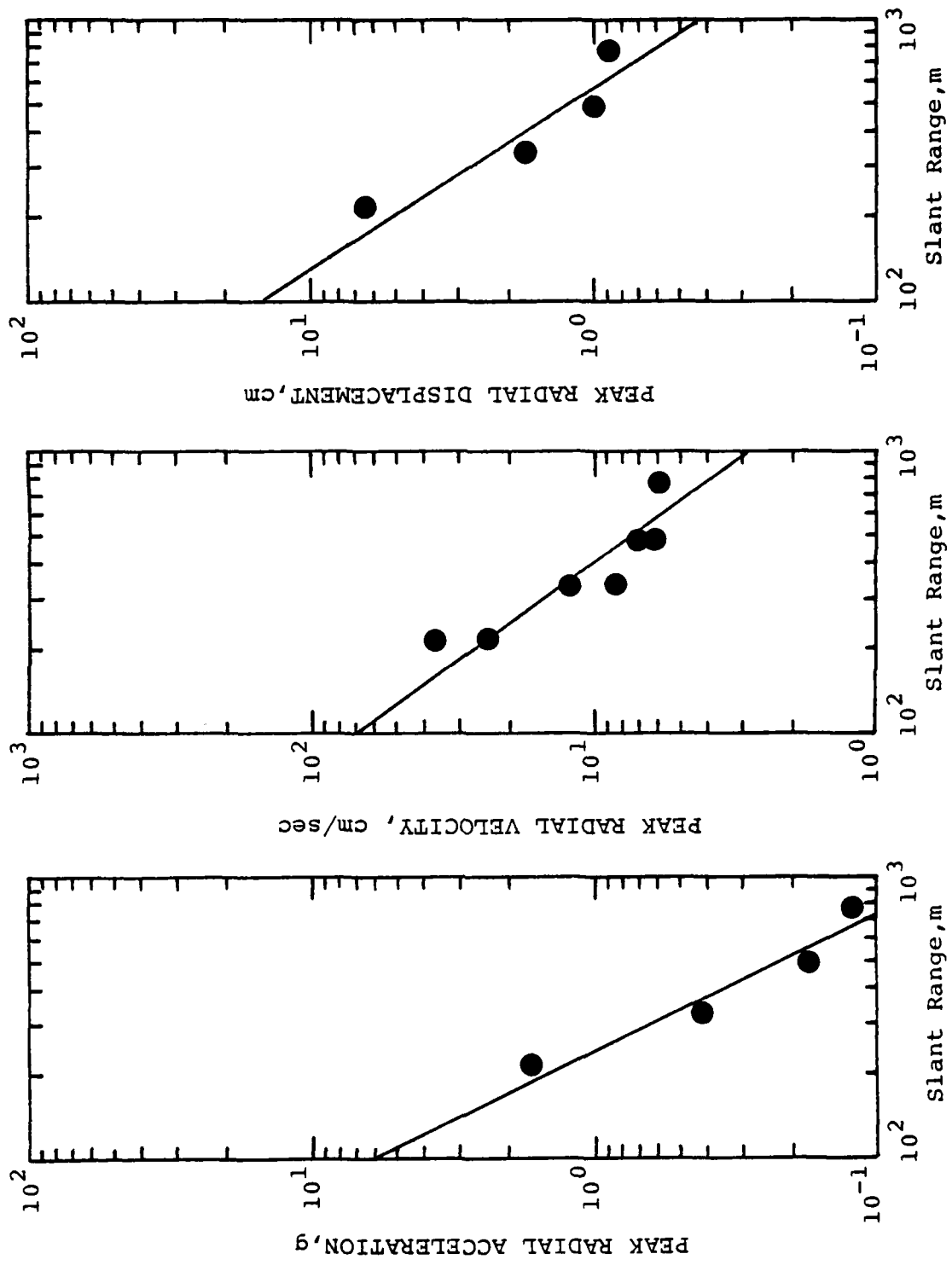
Figure 2.15 Observed Merlin Peak Motion Data as a Function of Range.

30
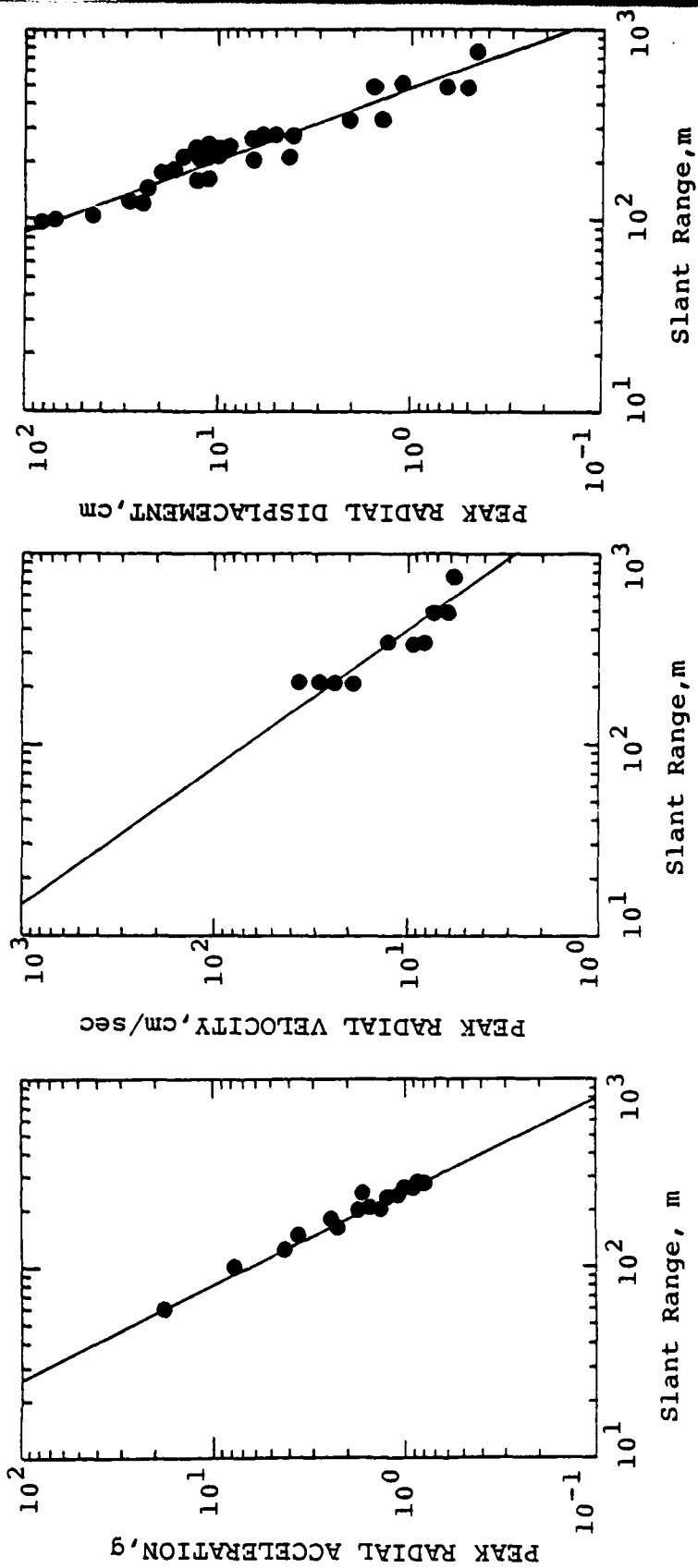
Figure 2.16 Observed Merlin Peak Motion Data as a Function of Range as Used by Perret.

regression relationships derived by Perret are not much different
from those which we derived. However, the regression relation-
ships for displacement are quite different. While the data used
in our derivation is rather sparse, it does have the advantage
of being consistent. On the other hand, Perret's displacement
data base is large but the procedure for picking the data was
not particularly consistent. Thus, the meaning of the attenuation
relationship in this latter case is ambiguous.

Five RDP's (cf. Figures 2.17 and 2.18) have been published
for Merlin (Perret, 1971). The RDP derived from the displacement
recorded at 107 m (3UR) is substantially larger than the other
four derived RDP's. This suggests that this measurement may have
been obtained within the strongly inelastic zone and therefore
does not accurately represent radiated seismic energy. Perret
(1971) also notes more rapid attenuation of peak motions for the
Merlin event for distances less than about 200 m which also tends
to support the idea that the 3UR RDP represents motion within the
strongly inelastic region. The published RDP's at late time
(near $\tau = 1.3$ sec) are contaminated particularly at the more
distant stations by a relatively long period motion which appears
to be generated by spall closure. This signal will be discussed
in detail in Chapter III below.

2.6   Hupmobile

The Hupmobile event was a 7.4 kt contained explosion
which was detonated at a depth of 247 m ($h/W^{\frac{1}{3}} = 127$ m/kt$^{\frac{1}{3}}$) in
dry alluvium at NTS on January 18, 1968. Instrumentation for
the Hupmobile event included a single station recording radial
acceleration and radial velocity at shot depth. The station was
at a range of 180 m and was the responsibility of Lawrence
Radiation Laboratory (Preston and Wheeler, 1969). Displacements
and velocities were derived by appropriate integrations of the
original velocity and acceleration time histories.
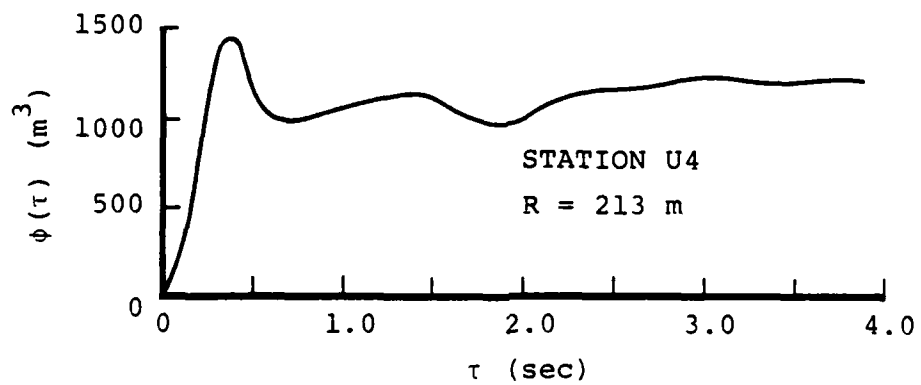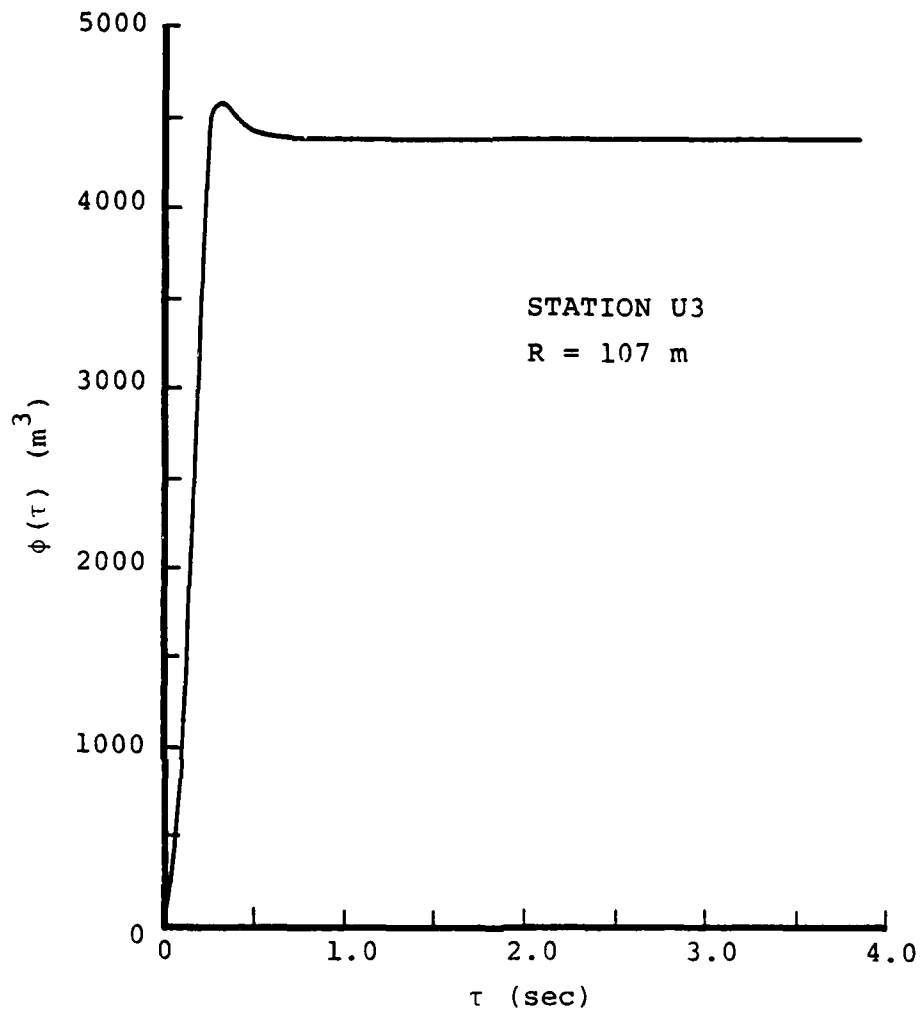
Figure 2.17   Observed Merlin Reduced Displacement Potentials
Stations U3 and U4.
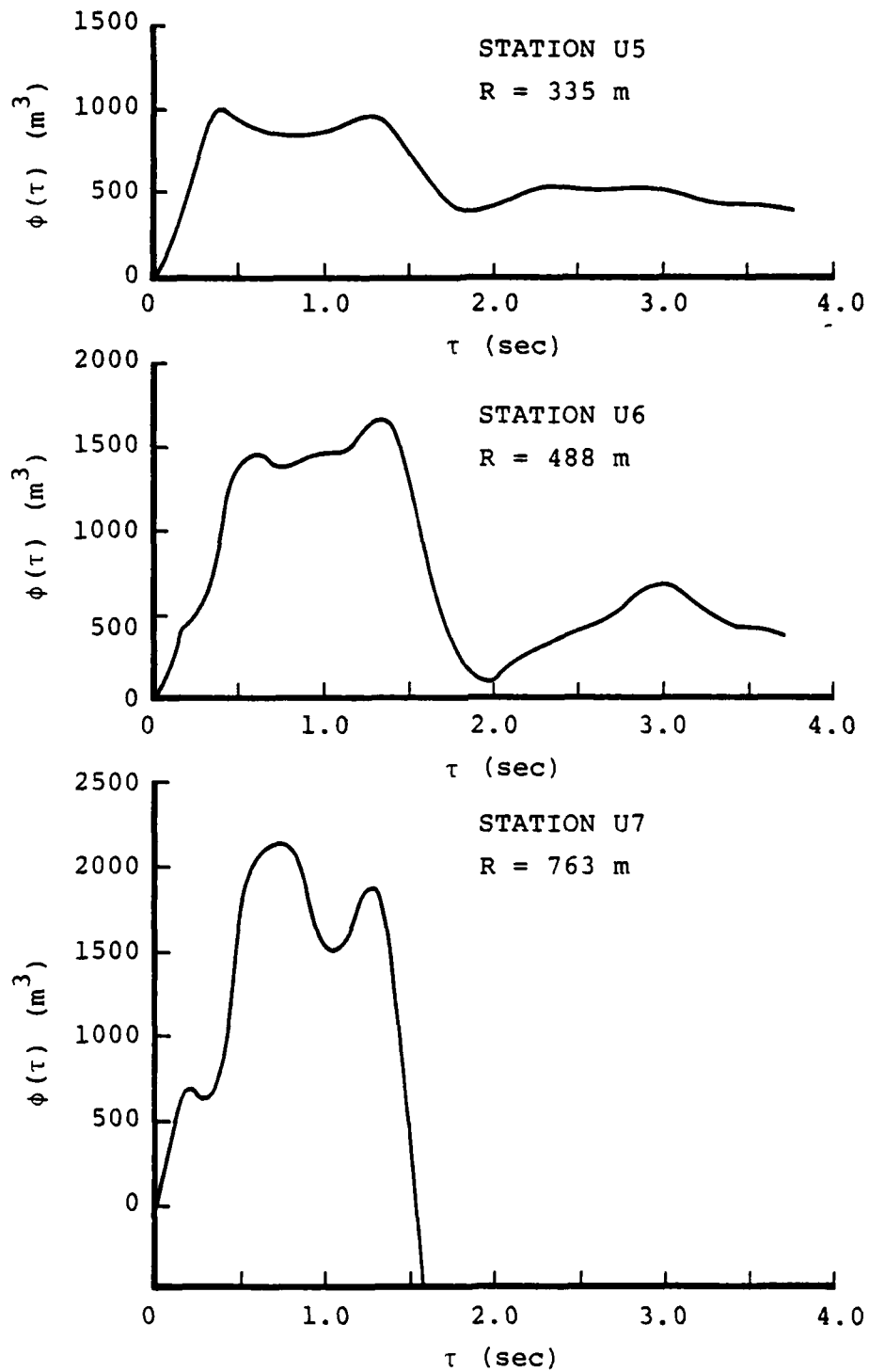
Figure 2.18   Observed Merlin Reduced Displacement Potentials
             Stations U5, U6 and U7.

Figure 2.19 is a surface map of the site showing the location of the deep instrument hole relative to ground zero. Figure 2.20 shows the location of the station on a vertical plane through the shot point. An approximate subsurface geologic profile is shown on the left side of the figure and consists of a simple alluvium medium extending from the surface to below shot depth. The compressional velocity and density in the alluvium was obtained from preshot geophysical logs of the instrument hole. These velocities were also consistent with the propagation velocities observed for the shot on the uphole stations.

Preston and Wheeler (1969) identify additional motion recordings obtained on uphole stations as being in the explosion free-field based on the calculated arrival times at the stations of the free-surface reflection. However, the only displacement record identified to be in the free-field is that from the station at shot depth. No regression analyses have been performed on the data in this study.

We derived a RDP from the radial displacement time history observed at shot depth at a range of 180 m; this RDP is shown in Figure 2.21. The lack of other free-field records from which RDP's could be computed makes it difficult to assure that this motion is representative of the radiated seismic ground motion for the Hupmobile event. Nevertheless, the RDP derived here appears to be reasonably consistent in shape and level with other RDP's derived for alluvium. If the RDP derived here were scaled to the Fisher yield assuming a linear relationship between RDP amplitude and event yield, the scaled RDP would underestimate the peak in the Fisher RDP (Gage 8, derived here) by only about 20 percent and matches it even more closely at later times. However, as noted above, it is not clear that the Fisher motion to which we are comparing is outside the strongly inelastic region.

35

N

100 m
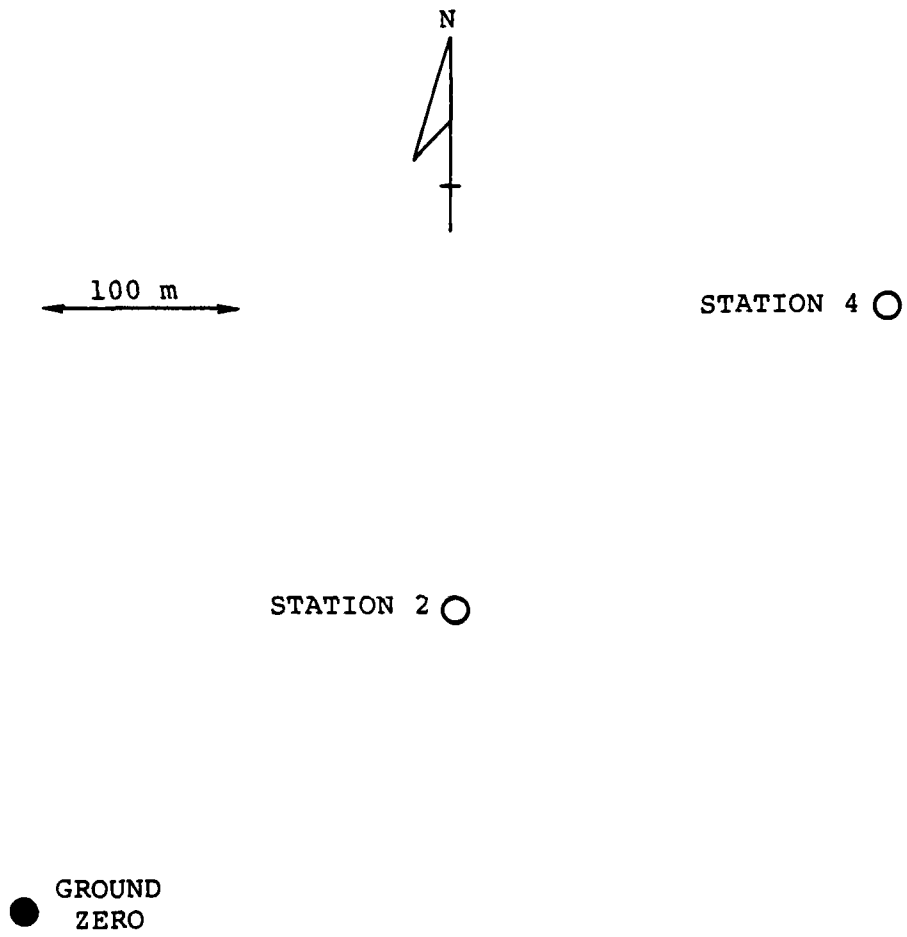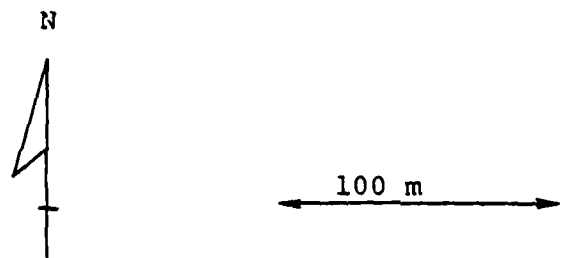
○ HOLE UE-2y

● GROUND ZERO
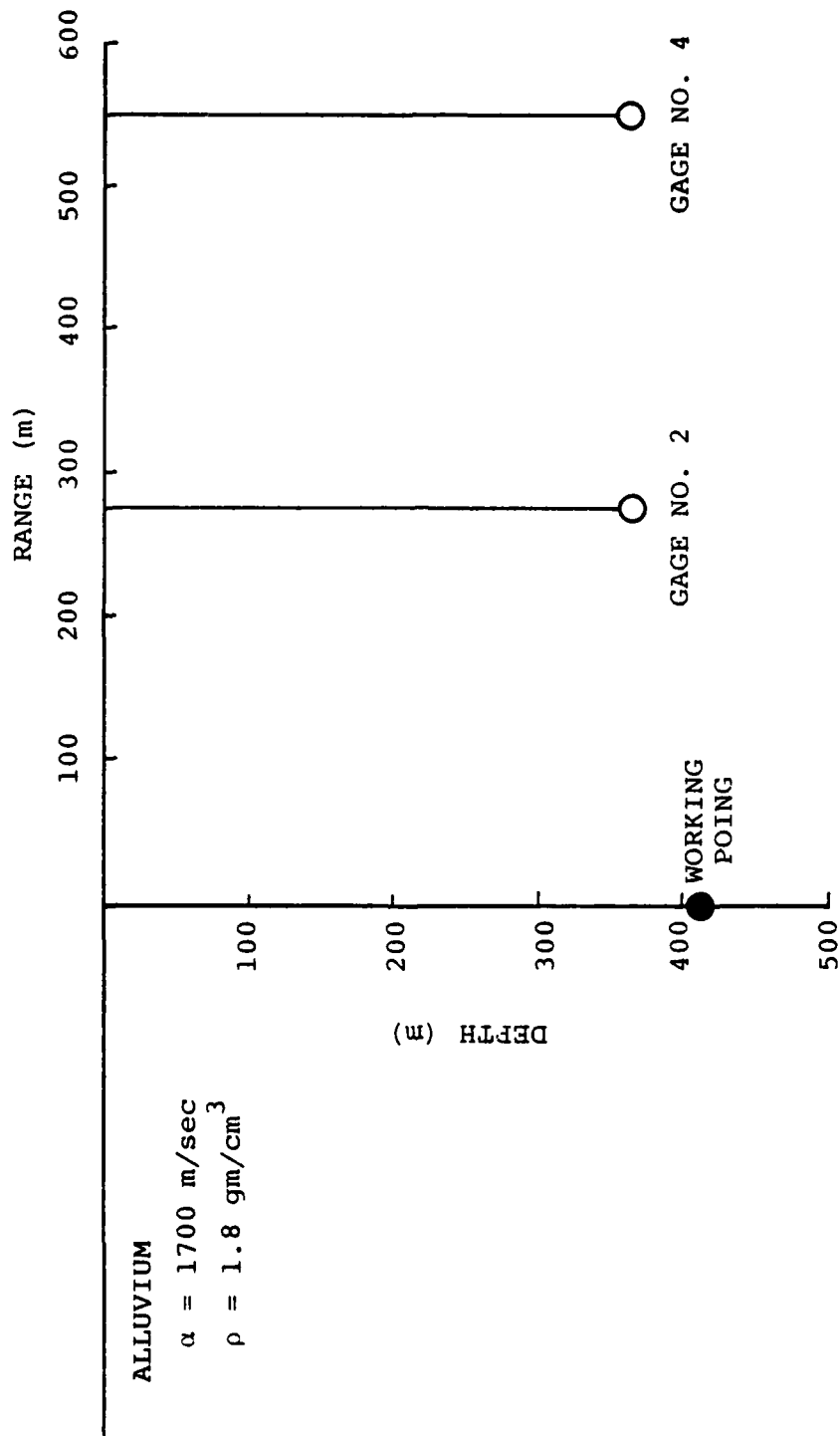
Figure 2.19. Surface Map of the Hupmobile Site.

Figure 2.20 Vertical Section Through the Hupmobile Detonation Point Showing the Relationship Between the Instrument Location and the Subsurface Geology at the Site.
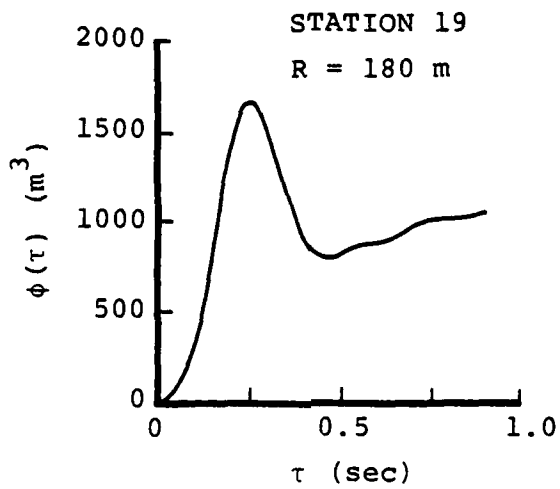
STATION 19
R = 180 m

Figure 2.21   Observed Hupmobile Reduced Displacement
Potential Station 19.

2.7 Packard

The Packard event was a 10 kt contained explosion which was detonated at a depth of 247 m ($h/W^{\frac{1}{3}} = 115$ m/$kt^{\frac{1}{3}}$) in dry alluvium at NTS on January 15, 1969. Instrumentation for the Packard event included a single station recording radial acceleration and velocity at shot depth. The instrument hole was the same as that used in the Hupmobile test. This station was at a range of 90 m and was the responsibility of Lawrence Livermore Laboratory (Wheeler and Preston, 1971). Displacements and velocities were derived by appropriate integrations of the original velocity and acceleration time histories.

Figure 2.22 is a surface map of the site showing the location of the deep instrument hole relative to ground zero. Figure 2.23 shows the location of the station on a vertical plane through the shot point. An approximate subsurface geologic profile is shown on the left side of the figure and is identical to the model for the Hupmobile event consisting of a simple alluvium medium extending to below shot depth. The compressional velocity and density were taken from the geophysical logs of the instrument emplacement hole and are consistent with observed propagation velocities for the event first motion.

Only the single station at shot depth could be considered to be in the free-field for measuring displacement and only a few of the stations above shot depth recorded peak velocities and accelerations at times prior to the predicted arrival of the free surface reflection. Because only these few free-field data points existed, no regression analysis was performed on the data.

Figure 2.24 shows a RDP derived from the radial displacement time history for the station at shot depth at a range of 90 m. Again, the lack of other free-field records from which RDP's could be computed makes it difficult to validate this motion as being representative of the radiated seismic field for the Packard event. In this case, the level of the RDP seems too large considering the event yield; the level is three to four times that which would be predicted on the basis of scaling the Hupmobile RDP assuming linear scaling of the RDP amplitude with yield. In addition, the Packard RDP shows little of the

N

50 m
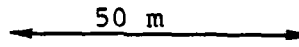
● GROUND ZERO

○ HOLE UE-2y

Figure 2.22 Surface Map of the Packard Site.
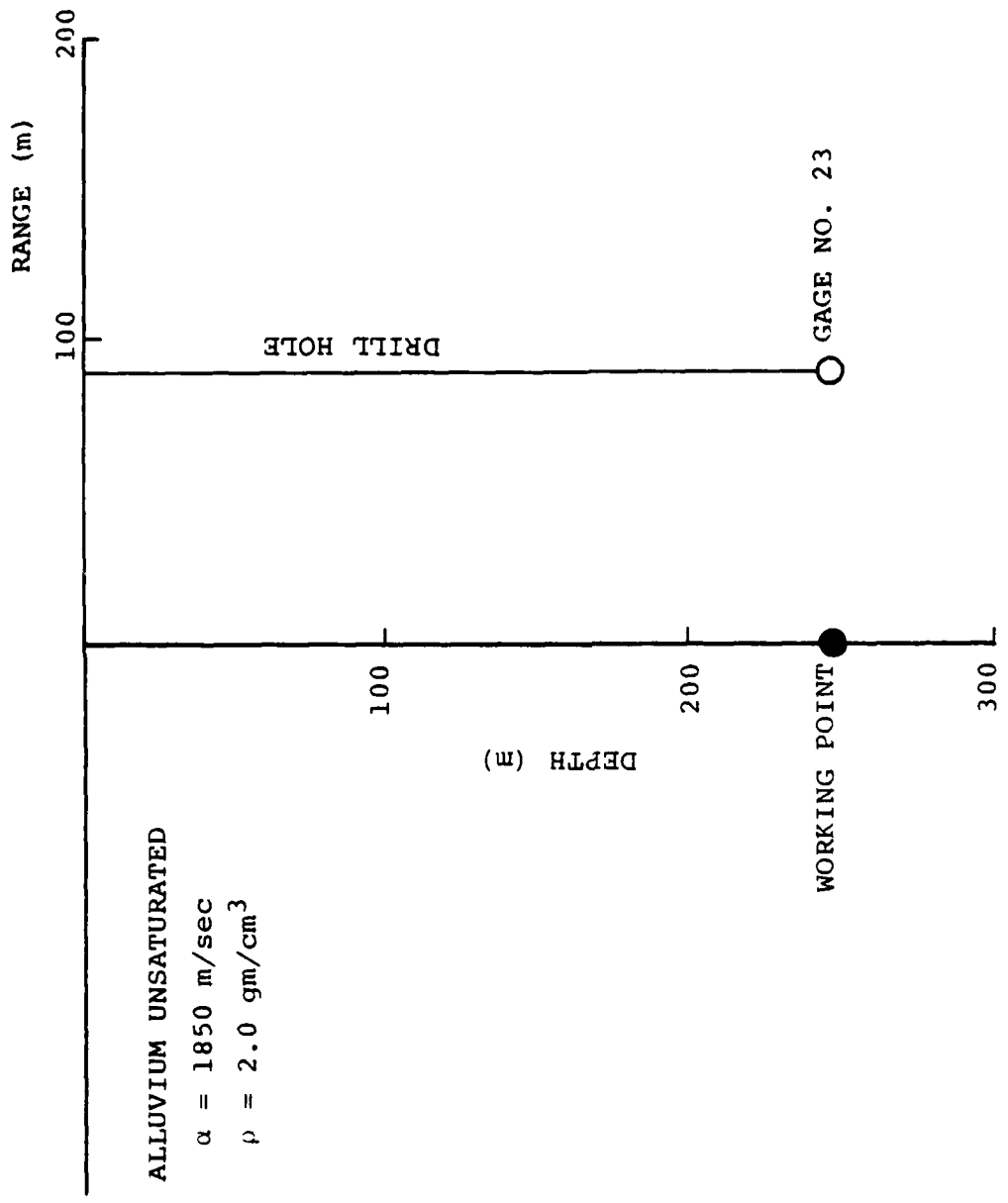
Figure 2.23 Vertical Section Through the Packard Detonation Point Showing the Relationship Between the Instrument Location and the Subsurface Geology at the Site.

41
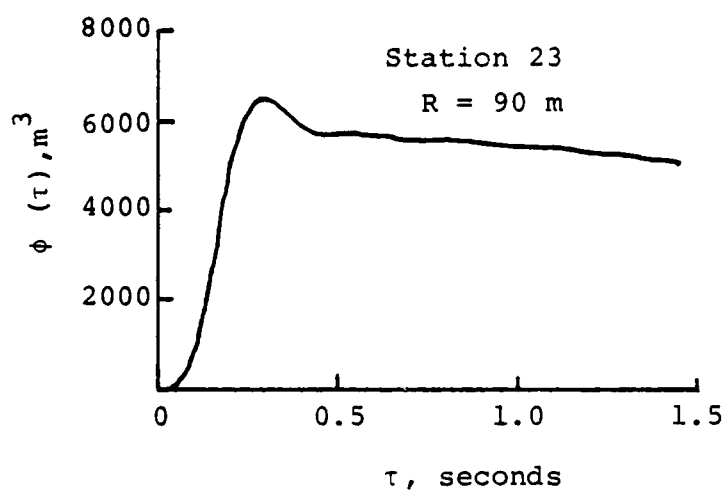
Figure 2.24   Observed Packard Reduced Displacement
Potential Station 23.

overshoot common to other alluvium RDP's. This, together with
the fact that the measurement was made at a very small scaled
range suggests that this RDP is not representative of the elastic
source function for this event.

2.8   Rainier

The Rainier event was a 1.7 kt contained explosion deton-
ated in a tunnel at a depth of 274 m ($h/W^{\frac{1}{3}}$ = 230 $m/kt^{\frac{1}{3}}$) in tuff
at NTS on September 19, 1957. Instrumentation for this event
was positioned at shot depth along the tunnel at various ranges
and also in a hole drilled from the surface of Rainier mesa
down toward the source. Measurements discussed here were obtained
from three stations near shot depth at ranges from 153 to 413 m and
four stations in the hole vertically above the source at ranges
from 112 to 205 m. All stations except the most distant were the
responsibility of Sandia Corporation (Perret, 1961). The instru-
ments at 413 m were located in a nearby tunnel and were the respon-
sibility of the U.S. Coast and Geodetic Survey (Perret, 1961).
The instruments consisted of accelerometers aligned to record
radial motion along the horizontal radius for the tunnel station
and along the vertical radius through the shot for the drill hole
stations. The acceleration time histories were integrated to
obtain velocity time histories and doubly integrated to obtain
displacement time histories.

Figure 2.25 is a plan map of the site (Perret, 1961)
showing the locations of the instruments relative to ground
zero. Figure 2.26 shows the locations of the stations on a
vertical plane through the shot point. An approximate subsurface
geologic profile is shown on the left side of the figure. It
consists of a rather thin layer of welded tuff (rhyolite) near
the mesa surface overlying less competent tuff extending to
below shot depth. The compressional velocities were estimated
from propagation velocities for the first arrivals from the test

N

100 m

GROUND
ZERO ● VERTICAL HOLE

○ AHP-6

○ AHP-7

TUNNEL
○ U-12d
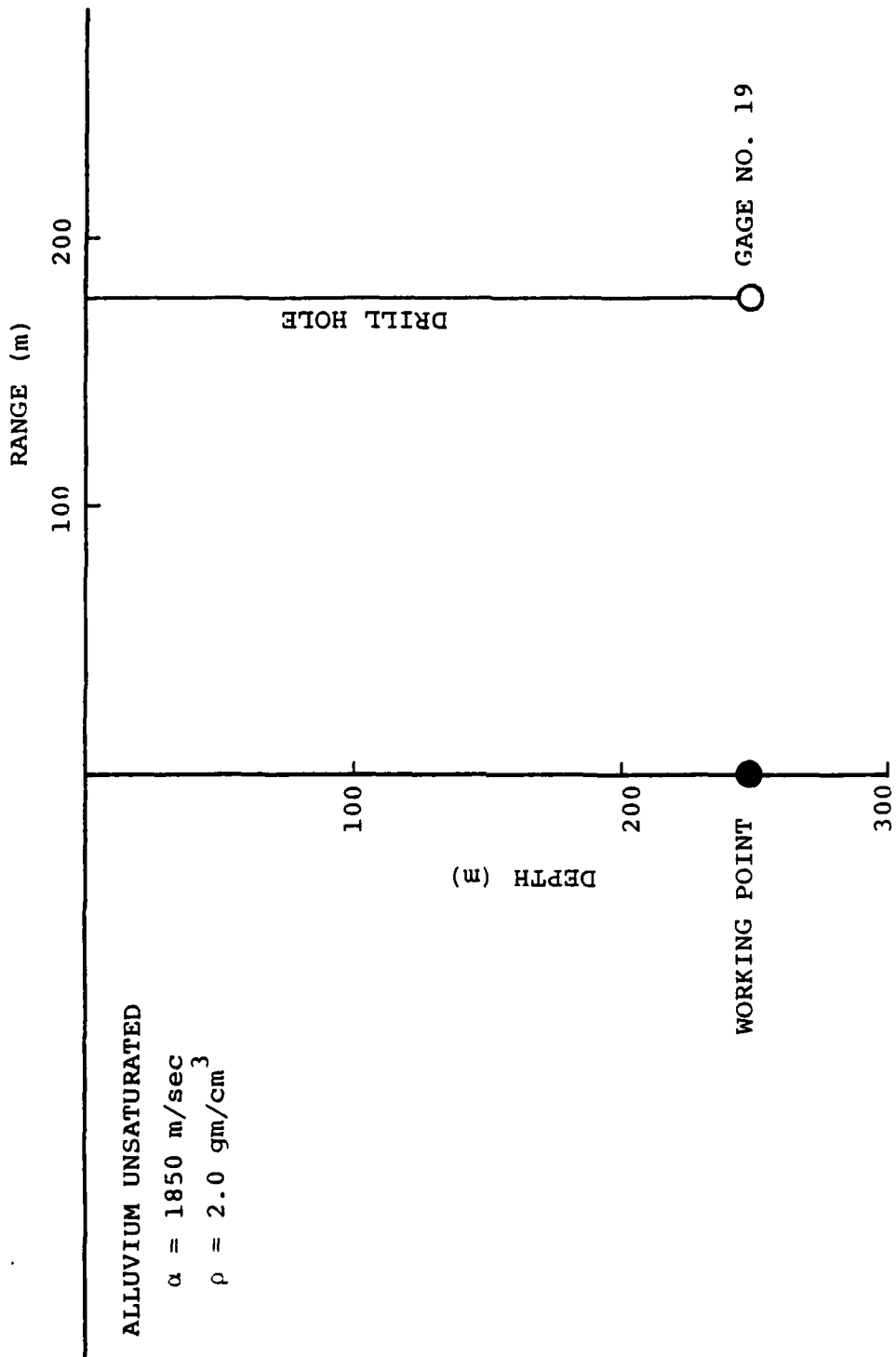INSTRUMENTATION

Figure 2.25 Surface Map of the Rainier Site.

Figure 2.26 Vertical Section Through the Rainier Detonation Point Showing the Relationship Between the Instrument Locations and the Subsurface Geology at the Site.

45

(Perret, 1961). In actuality, Perret (1961) describes a more complex velocity structure with lateral variations in velocity through the section and decreasing velocity from the base of the welded tuff layer to the surface.

Peak radial ground motion measured at the recording stations described above are shown in Figure 2.27. Regression analyses were performed on the peak acceleration, velocity and displacement data; these resulted in:

$$a_r = 5.13 \times 10^3 \; R^{-1.37}$$

$$v_r = 2.57 \times 10^4 \; R^{-1.05}$$

$$d_r = 5.75 \times 10^3 \; R^{-1.22}$$

Perret (1961) looked at all the peak motion data disregarding proximity to the source and to the free surface; these are shown in Figure 2.28. Though no formal regression analysis was performed on the data, slopes were estimated and are superimposed on the figure. The peak acceleration and peak velocity data suggest more rapid attenuation for ranges less than 180 m and 100 m respectively which could indicate that strongly inelastic behavior extends to these distances.

Werth and Herbst (1962) published a RDP developed for the displacement time history for the Rainier event recorded above the shot at a range of 112 m. This is shown in Figure 2.29 along with two RDP's which we derived. The one RDP which we derived used the same displacement time history as that used by Werth and Herbst, but extended the integration to later time. The reason for the difference is that Werth and Herbst fixed the steady state level of the RDP beyond about $\tau = .35$ sec on the basis of the measured cavity radius for the Rainier event (assuming incompressibility); so that:

$$\phi \; (\tau > .35) = 1750 \; m^3.$$
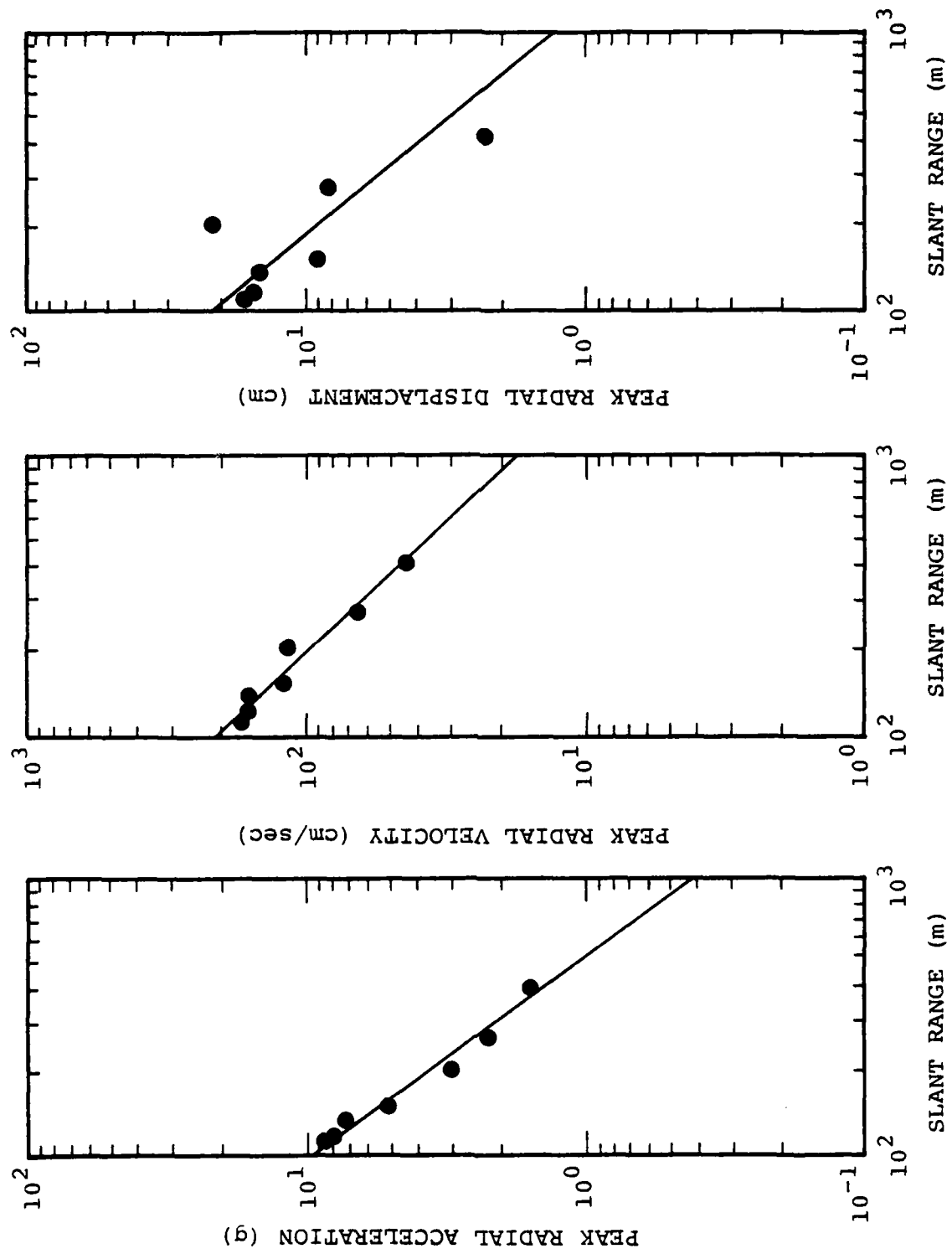
Figure 2.27 Observed Rainier Peak Motion Data as a Function of Range.

47
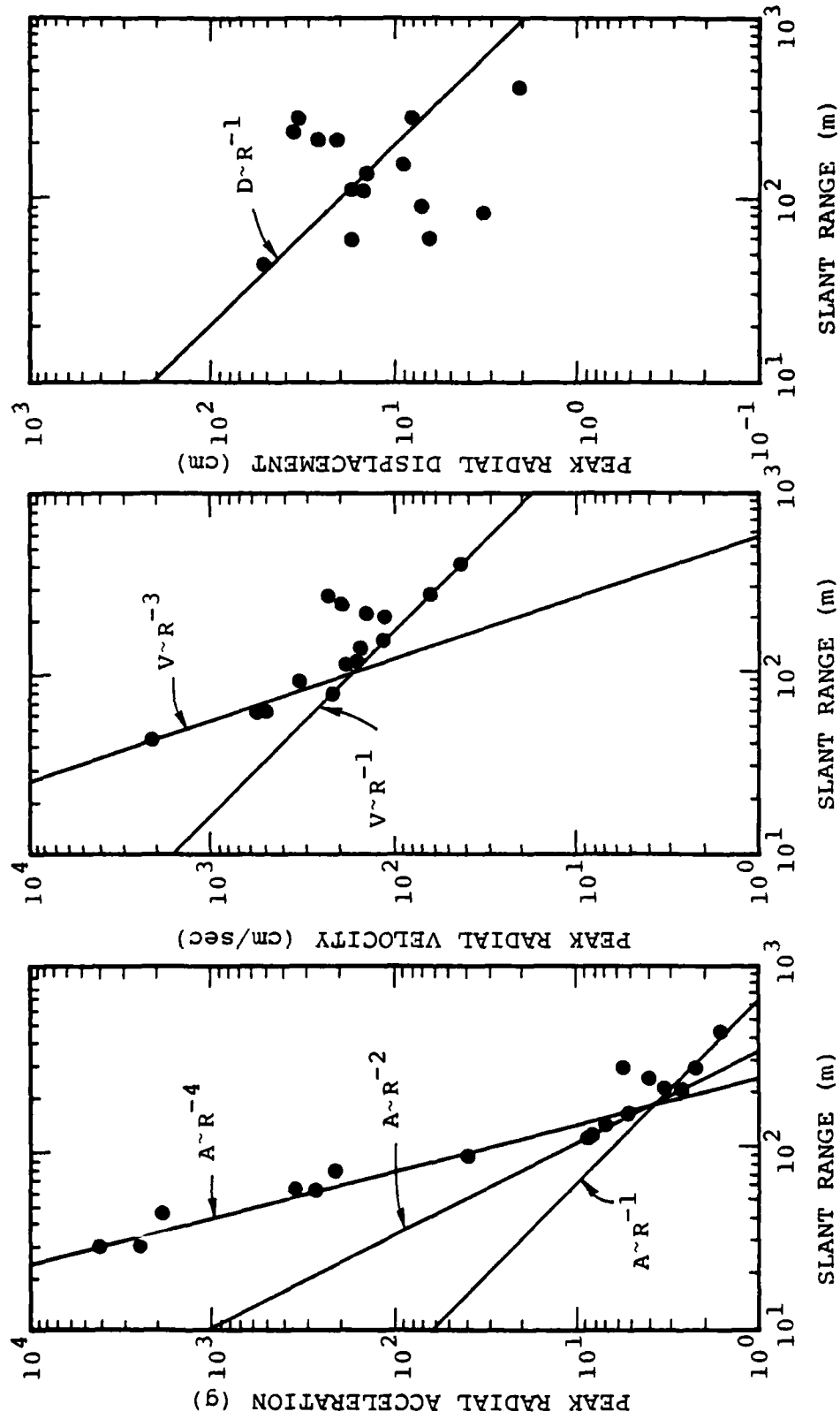
Figure 2.28 Observed Rainier Peak Motion Data as a Function of Range as Used by Perret.

48
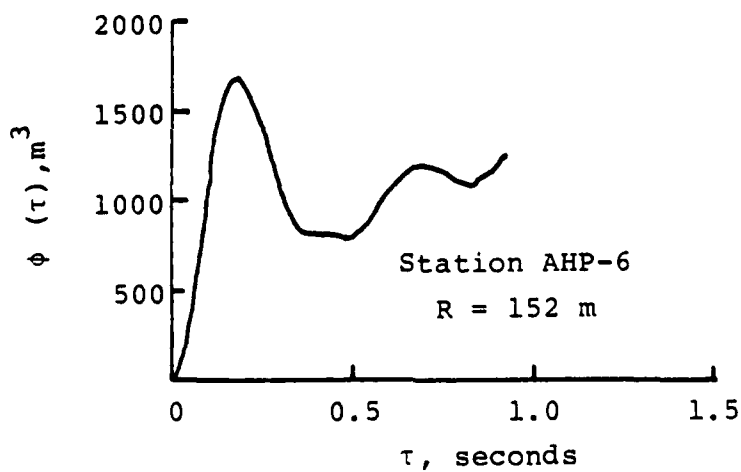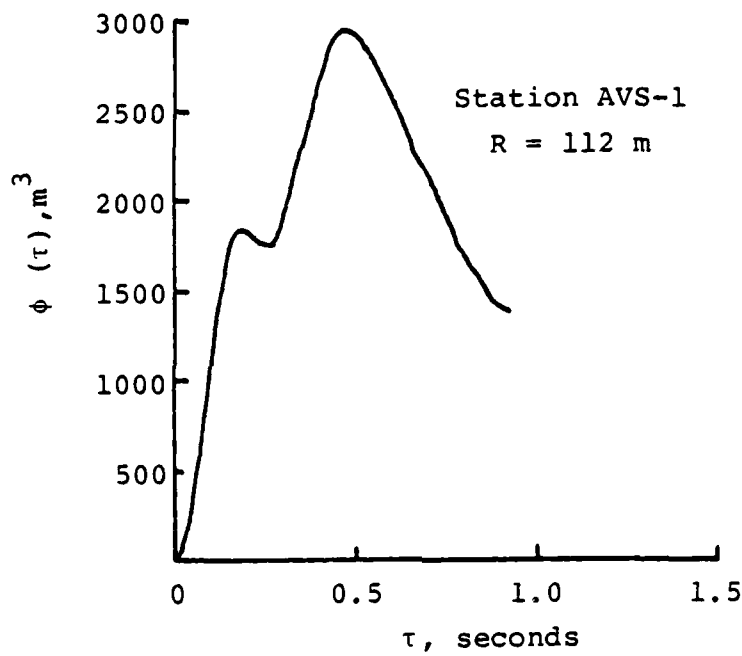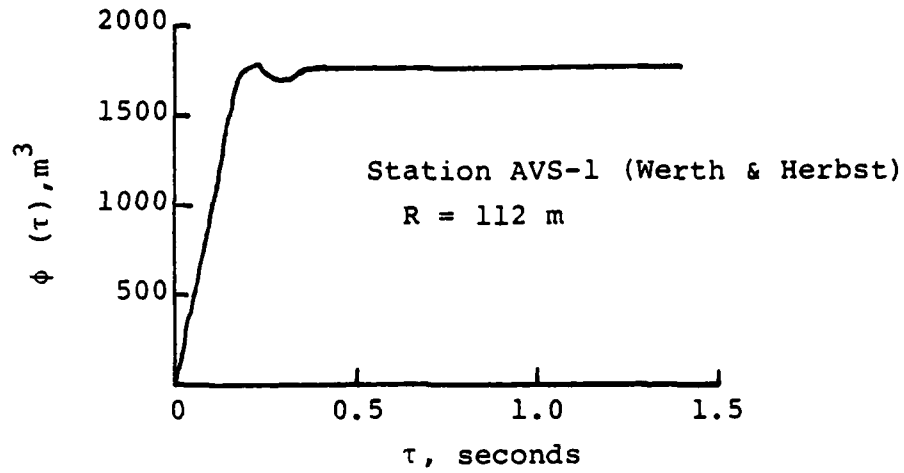
Figure 2.29   Observed Rainier Reduced Displacement Potentials
Station AVS-1 (simplified after Werth & Herbst),
Station AVS-1 and Station AHP-6.

49

For the RDP derived from the actual time history at the 112 m range, reflections from the free surface contaminate the motion shortly after the arrival of the peak near τ = .25 sec. Thus, motion after this time probably does not accurately represent free-field motion. We also derived a RDP for the displacement recorded at shot depth at a range of 152 m. This is shown in Figure 2.29. While the RDP amplitude at early time (τ < .25 sec) is comparable to that computed above, the amount of over-shoot and level at late time make this RDP appear quite different from that derived for the AVS-1 station. This may be an indication that the incompressibility assumption invoked by Werth and Herbst is not appropriate for porous media such as tuff. The RDP from the shot-depth station does not seem to be contaminated by the free-surface reflection and is therefore probably more representative of the radiated seismic field, at least for times less than about 0.5 sec.

2.9 Mud Pack

The Mud Pack event was a 2.7 kt contained explosion which was detonated at a depth of 156 m ($h/W^{\frac{1}{3}}$ = 112 m/kt$^{\frac{1}{3}}$) in tuff at NTS on December 16, 1964. This event was located near the Handcar event described below and has much of the same instrumentation as used for that event. Measurements discussed here were obtained from ten stations all of which were located below shot depth at ranges from 103 to 280 m. The stations were the responsibility of Sandia Corporation (Perret, 1970c). The instruments were located in drill holes and consisted of accelerometers and velocity gages. These were oriented to provide measurements of the horizontal radial component and the vertical component of ground motion. These motions were corrected to motions along a radial vector from the shot to the recording station by resolving the horizontal and vertical motions in that direction. Acceleration and velocity measurements were obtained directly; displacements were obtained by integrating the radial vector velocity time histories.

Figure 2.30 is a surface map of the site (Perret, 1970c) showing the locations of the instrument holes relative to ground zero. Figure 2.31 shows the locations of the stations on a vertical plane through the shot point. An approximate subsurface geologic profile is shown on the left side of the figure and consists of an alluvium layer overlying the tuff emplacement medium. Below shot level near the elevation of the recording instruments a thin shale layer overlies a thick dolomite bed. A fault not shown on the figure causes a repetition of shale and dolomite layers below the shale-dolomite interface in the vicinity of drill hole U10b-4. Compressional velocities in the various layers were estimated from propagation velocities of direct and refracted arrivals (Perret, 1970c). The densities shown are typical of those determined for these media at NTS.

Peak radial vector ground motions measured at the recording stations described above are shown in Figure 2.32. Regression analyses were performed on the peak acceleration, velocity and displacement data. These resulted in:

$$a_r = 1.25 \times 10^6 \, R^{-2.90}$$

$$v_r = 8.32 \times 10^3 \, R^{-1.25}$$

$$d_r = 4.79 \times 10^2 \, R^{-1.18}$$

Perret (1970c) performed similar regression analyses including additional peak acceleration and velocity data for drill hole U10b-5 at ranges from 61 to 261 m; these data are relatively noisy and of short duration so that no displacement time histories could be derived. Perret's regression analyses give:

$$a_r = 3.07 \times 10^5 \, R^{-2.64}$$

$$v_r = 2.61 \times 10^3 \, R^{-1.49}$$

$$d_r = 4.96 \times 10^2 \, R^{-1.19}.$$

N

● GROUND ZERO

100 m
○ HOLE U10n-1
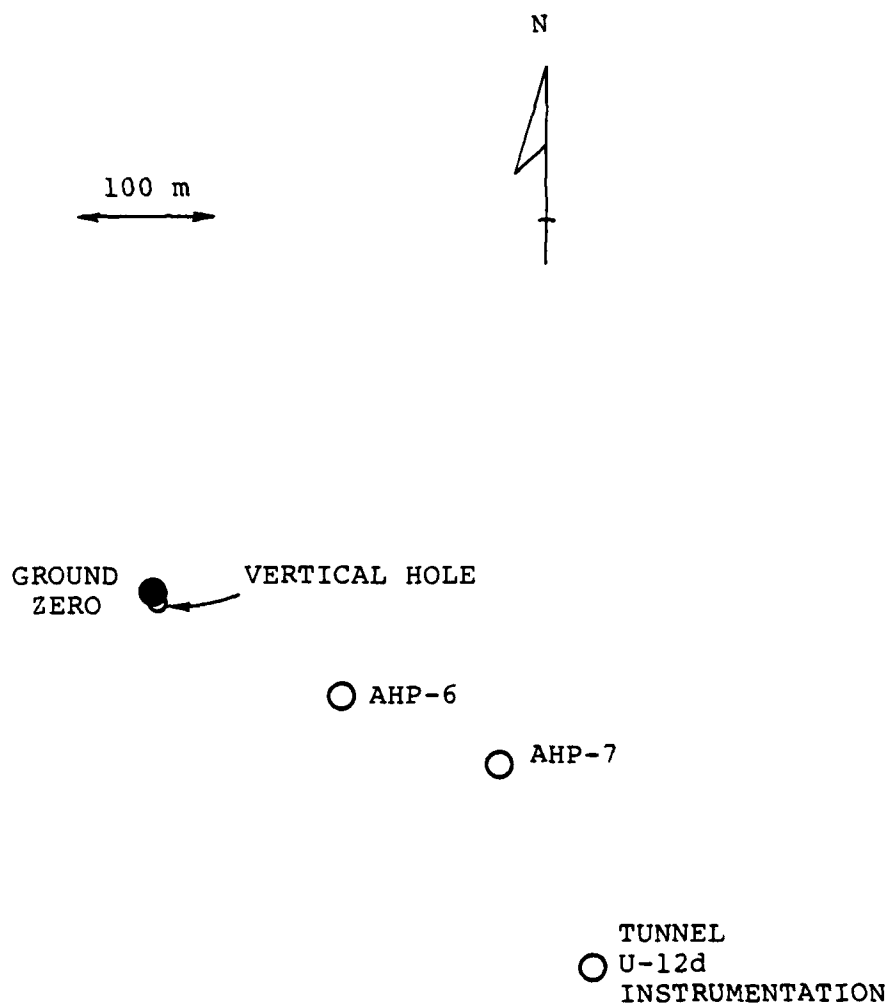
○ HOLE U10b-4

○ HOLE U10b-2

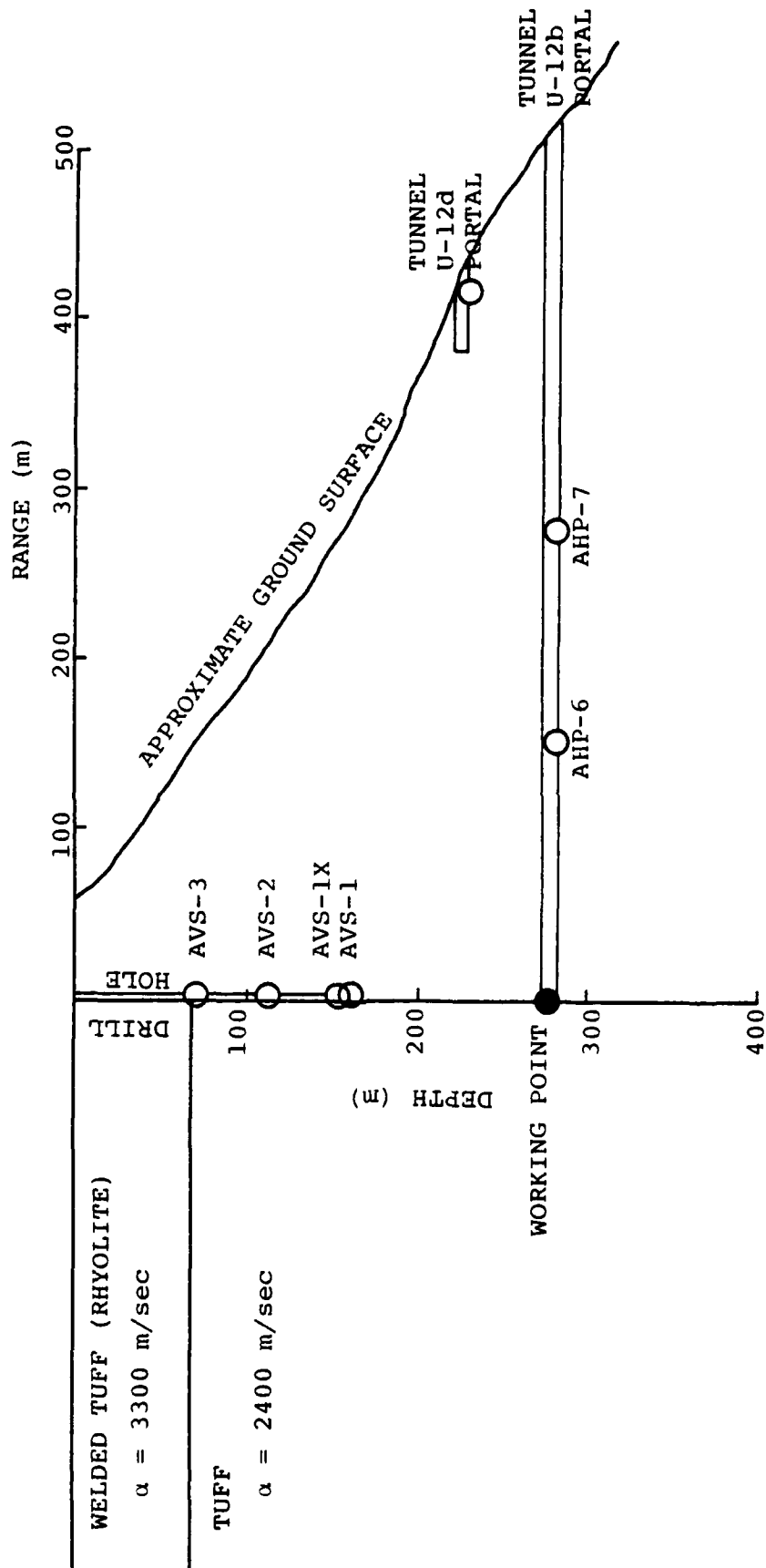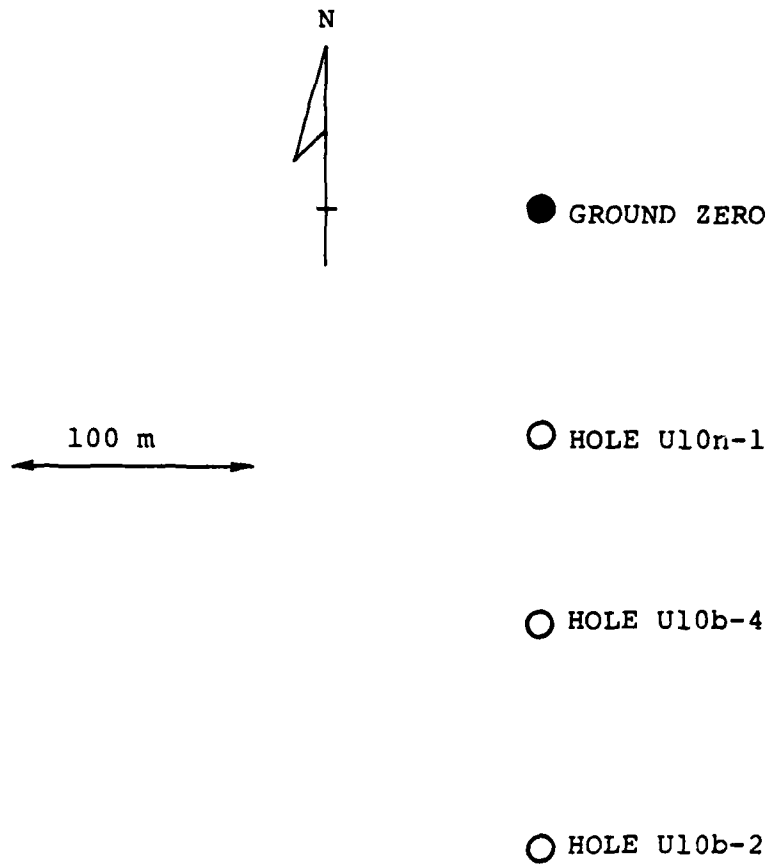Figure 2.30. Surface Map of the Mud Pack Site.

Figure 2.31   Vertical Section Through the Mud Pack Detonation Point Showing the Relationship Between the Instrument Locations and the Subsurface Geology at the Site.
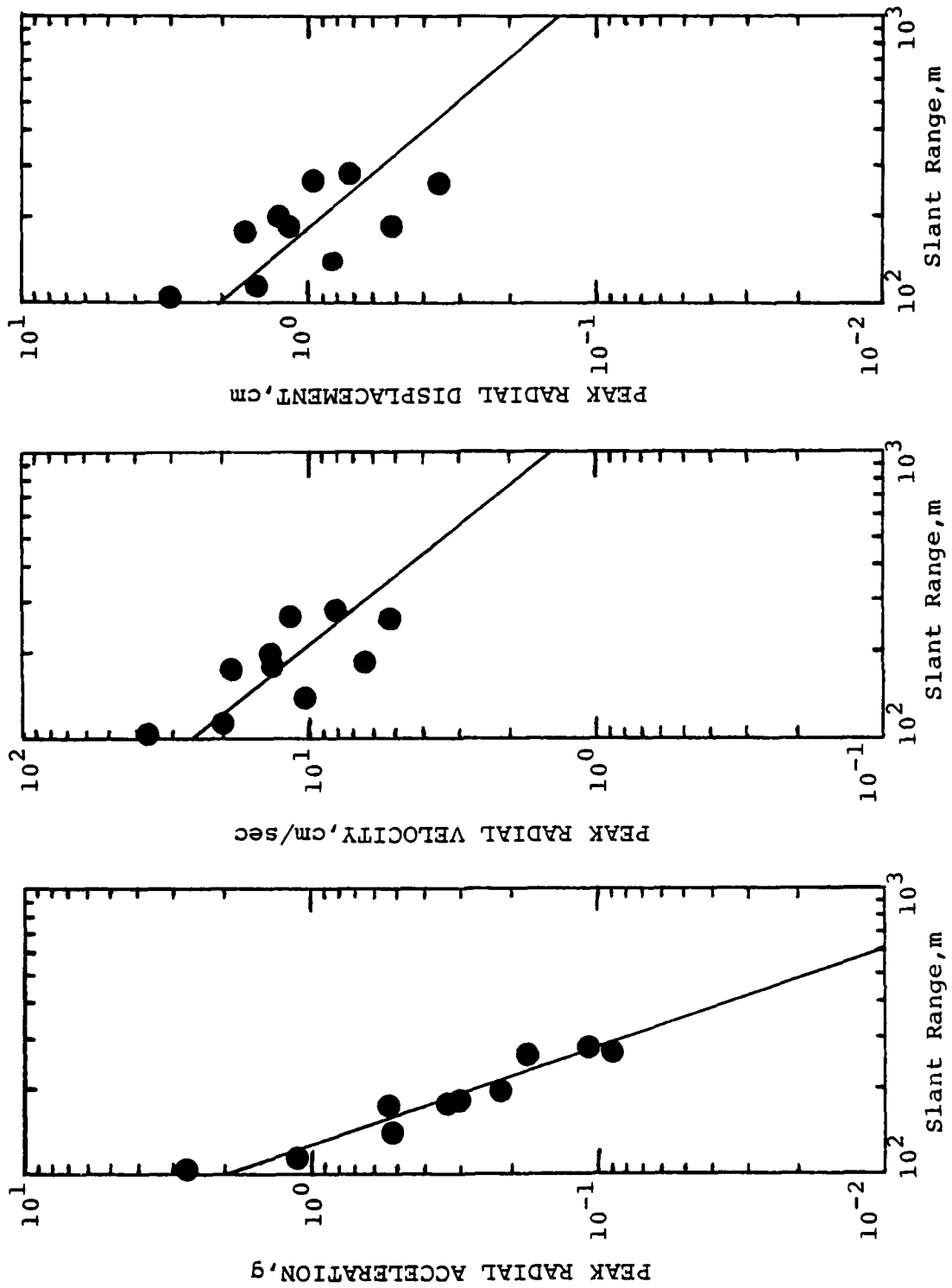
Figure 2.32 Observed Mud Pack Peak Motion Data as a Function of Range.

54

These regression relations are close to those which we derived over the range of observations presented in Figure 2.32. The fit of the regression lines to the data is regarded as poor except for the peak acceleration data (Perret, 1970c); scatter in the data can possibly be attributed to the influence of layering.

We computed three RDP's from the radial vector displacement time histories recorded at ranges of 175 m, 181 m and 197 m; these are shown in Figure 2.33. The derived RDP's are quite similar to one another but are generally more complex than RDP's determined for more homogeneous source media. Moreover, the amplitude levels of these RDP's are considerably lower then would be expected from scaling either the Rainier data or the Discus Thrower data described below. We have not looked at the motions in detail but several of the arrivals after the initial peak can probably be explained as waves reflected in the layered geology. More detailed considerations of this problem is provided in Chapter III for the Discus Thrower and Handcar events. One feature particularly notable in the RDP is the trough following the initial peak. Comparison of the radial and vertical component displacement records with the radial vector displacement record used to compute the RDP indicates that this trough was probably enhanced in resolving the radial vector motion and that it corresponds to motion which is primarily vertical. This coupled with the arrival time of this motion suggests that it represents a free surface reflection. A similar effect was noted for Handcar and will be discussed below.

2.10 Discus Thrower

The Discus Thrower event was a 21 kt contained explosion which was detonated at a depth of 338 m ($h/W^{\frac{1}{3}}$ = 123 $m/kt^{\frac{1}{3}}$) in tuff at NTS on May 27, 1966. Measurements discussed here were obtained from nine stations located near and somewhat below shot depth in two drill holes. This instrumentation covered ranges from 488 to 1344 m (mainly in two clusters near these ranges)

55
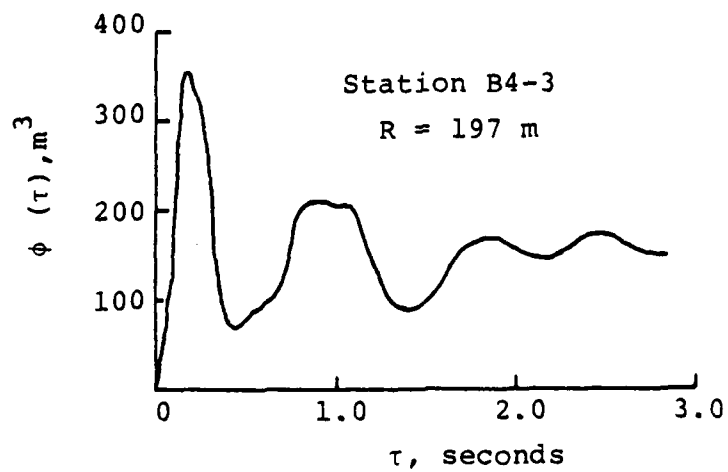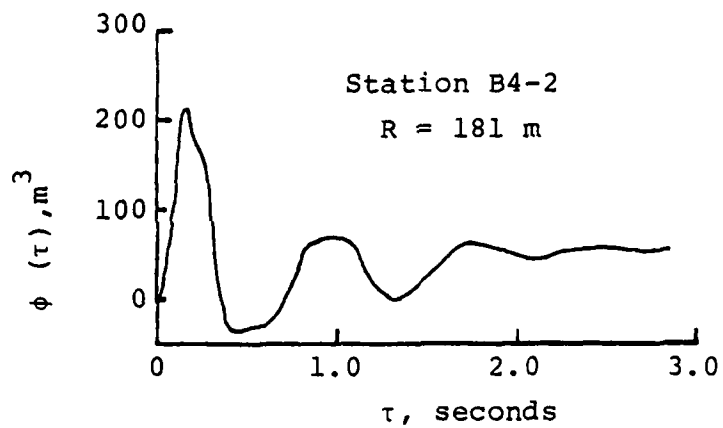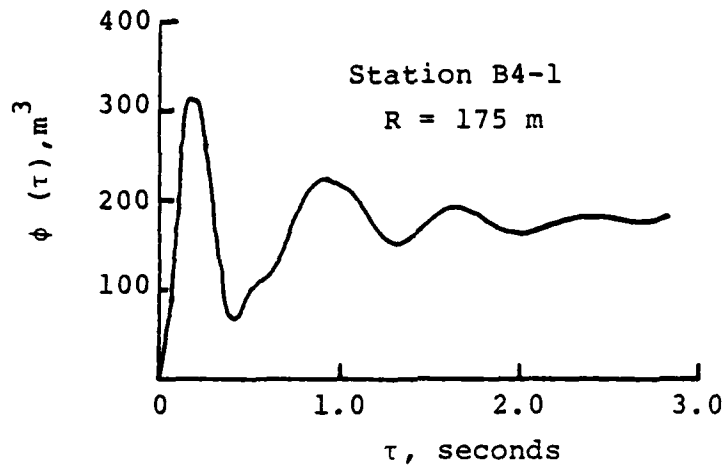
Figure 2.33 Observed Mud Pack Reduced Displacement
Potentials Stations B4-1, B4-2 and B4-3.

56

and was the responsibility of Sandia Corporation (Perret and Kimball, 1971). Each station included vertical and radial accelerometers and vertical and radial velocity gages. Thus, acceleration and velocity were measured directly and additional velocity and displacement time histories were derived by appropriate integrations of the acceleration and velocity records. Additional ground motion time histories representing radial vector motion were derived from the velocity records by resolving the horizontal radial motion and the vertical motion in the direction of the vector from the shot to the stations. Finally, so-called "resultant" motions were derived by taking the square roots of the sums of the squares of the horizontal and vertical motions as a function of time for each station.

Figure 2.34 is a surface map of the site (Perret and Kimball, 1971) showing the locations of the instrument holes relative to ground zero. Figure 2.35 shows the locations of stations on a vertical plane through the shot point. An approximate subsurface geologic profile is shown on the left side of the figure. The section consists of a 180 m thick alluvium layer overlying tuff which extends to about 60 m below shot level where Paleozoic rocks including carbonates, argilite and dolomite are present. In the actual section the tuff layer thickens by about 60 m and the underlying carbonate layer approaches a thickness of 70 m midway between the shot emplacement hole and boring 12. Compressional velocities and densities were estimated from average values determined from seismic refraction surveys and geophysical logs of the instrument holes.

Figure 2.36 shows the peaks for the horizontal components of the radial ground motions. Considering the angles of incidence these values would be expected to differ from the radial vector peak motion by less than ten percent. Regression analyses were performed on the peak acceleration, velocity and displacement data resulting in:

200 m

N

● GROUND ZERO

O HOLE U8a-7

O HOLE U8a-9

O HOLE U8a-11

O HOLE U8a-12

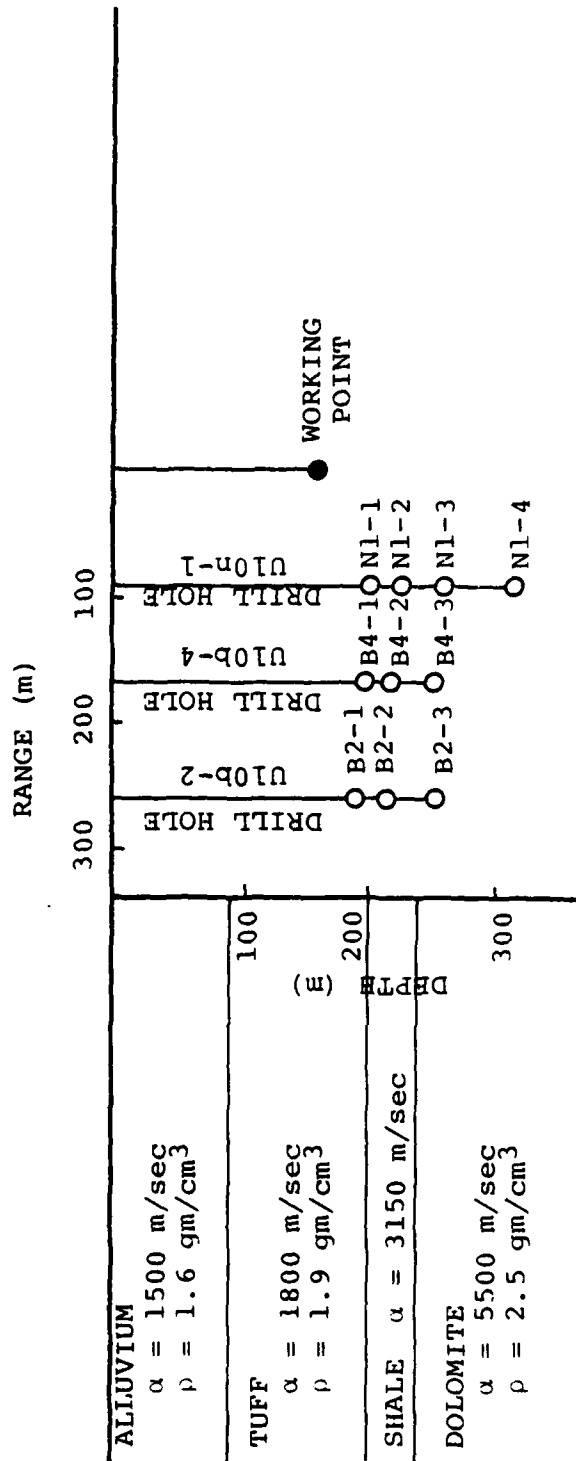Figure 2.34. Surface Map of the Discus Thrower Site.

Figure 2.35 Vertical Section Through the Discus Thrower Detonation Point Showing the Relationship Between the Instrument Locations and the Subsurface Geology at the Site.

59
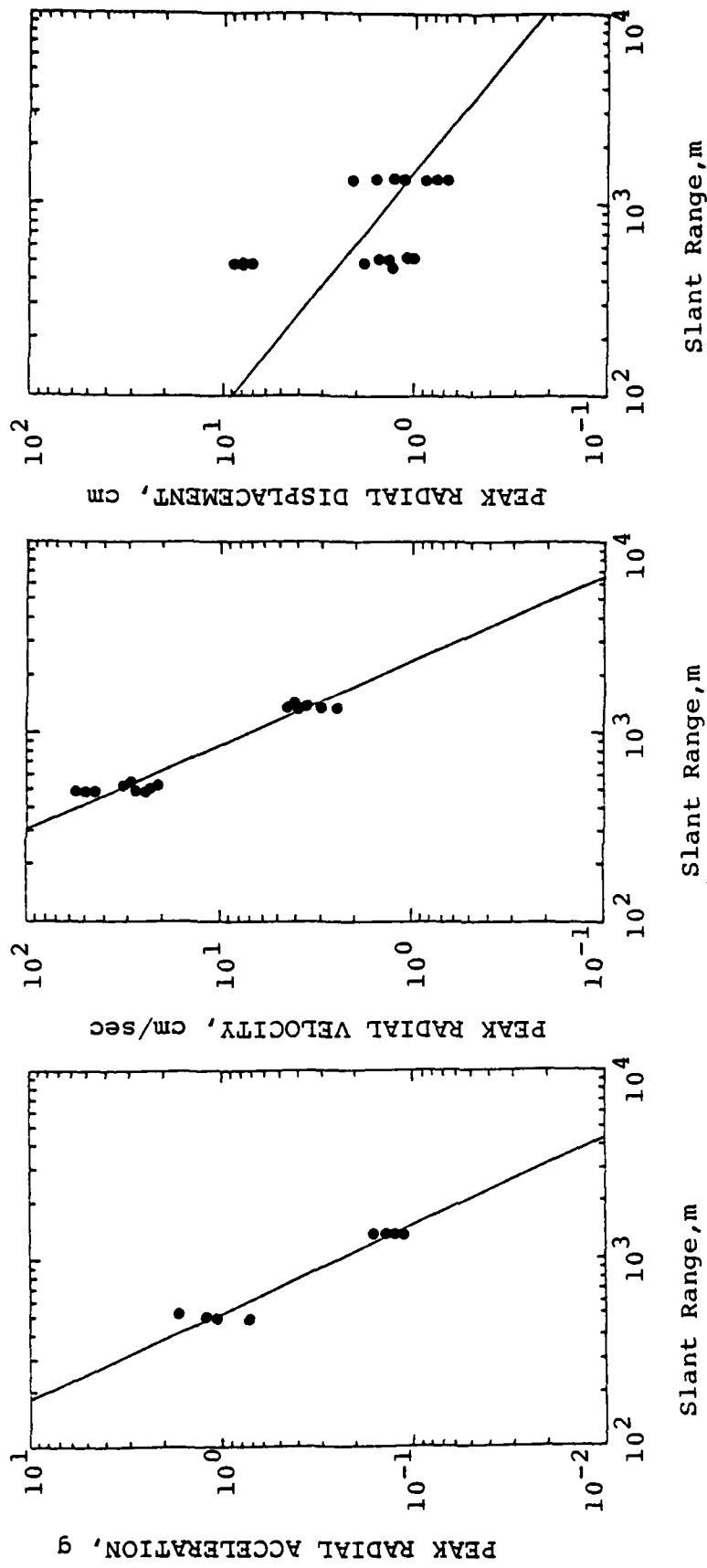
Figure 2.36   Observed Discus Thrower Peak Motion Data as a Function of Range.

$$a_r = 8.71 \times 10^5 \, R^{-2.18}$$

$$v_r = 4.07 \times 10^7 \, R^{-2.26}$$

$$d_r = 3.63 \times 10^2 \, R^{-.81}$$

Perret and Kimball (1971) performed a regression analysis on peak motions determined from the derived radial vector and resultant velocity time histories for recordings from stations in the Paleozoic rocks for instrument holes 9 and 12 supplemented by similar data from instruments in two other holes reported by Day and Vispi (1969). These data are shown in Figure 2.37 and the regression line which they derived (converted to metric units) is

$$v_r = 1.37 \times 10^7 \, R^{-2.08}.$$

In the range of the observations this regression line matches that which we derived quite closely. This is somewhat surprising considering that the data in our sample included diverse transmission paths while the Perret and Kimball data was only for stations in Paleozoic rocks and would be expected to better represent transmission in that type of rock. The similarity of our results to theirs suggests that for the Discus Thrower event the effects of attenuation in the Paleozoic rocks were not much different than in tuff.

Eighteen RDP's have been published for the Discus Thrower event (Perret and Kimball, 1971); these are shown in Figures 2.38 through 2.41. Nine RDP's were computed from the radial vector motions and nine from the resultant motions. The RDP's are quite different in level and shape. RDP's for the two tuff stations nearest the shot, 9AUR and 9BUR, closely match one another and exhibit some similarities in shape and level to RDP's derived for stations from boring 12. However, the RDP's derived for stations in the Paleozoic rocks for boring 9 are
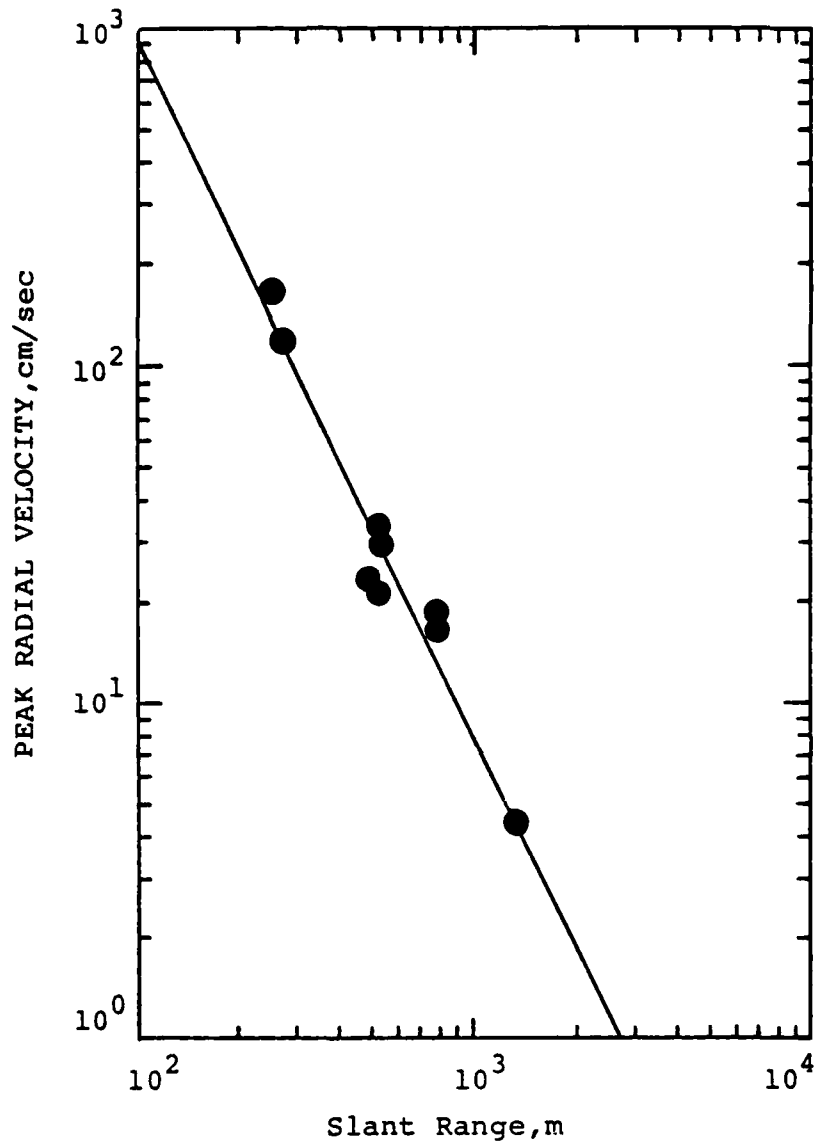
Figure 2.37   Observed Discus Thrower Peak Velocity
Data as a Function of Range as Used by
Perret and Kimball.

62
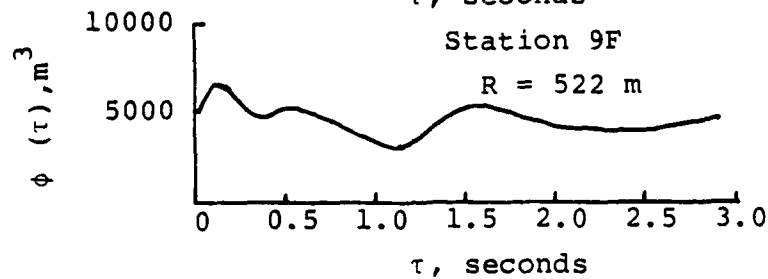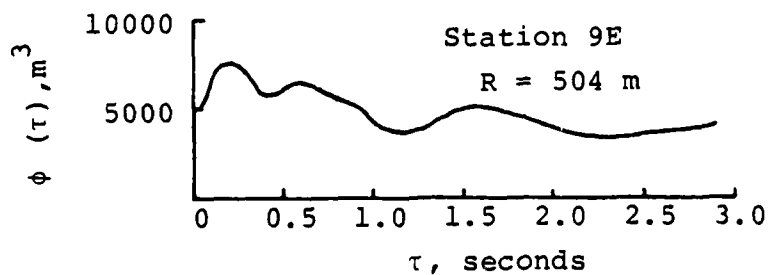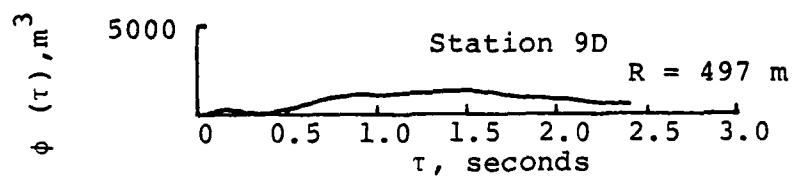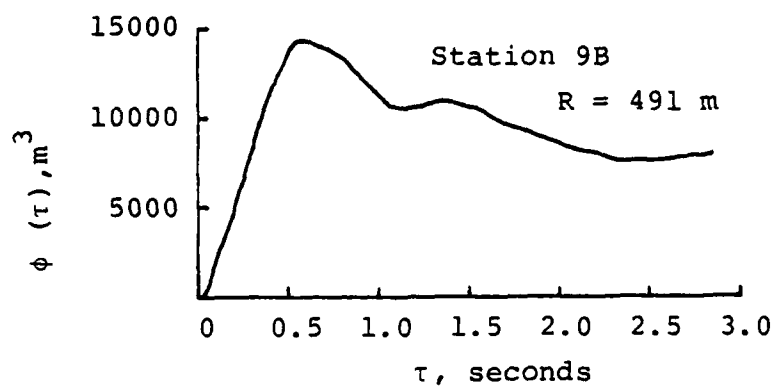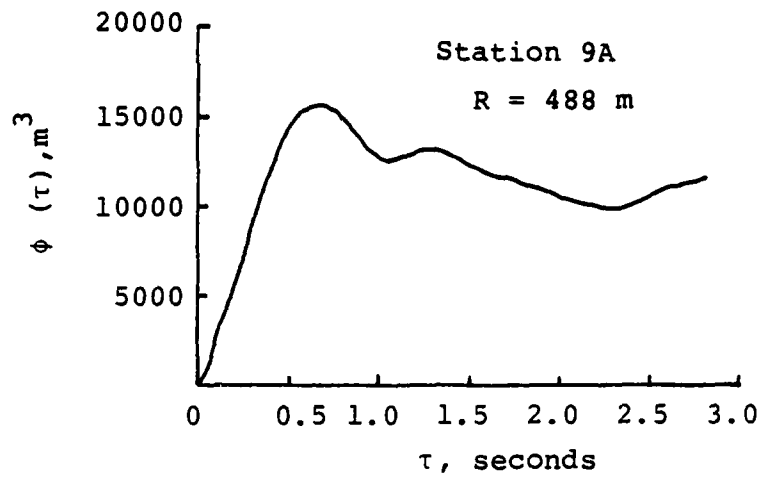
Figure 2.38 Observed Discus Thrower Reduced Displacement
Potentials Derived from Radial Vector Data
Stations 9A, 9B, 9D, 9E and 9F.
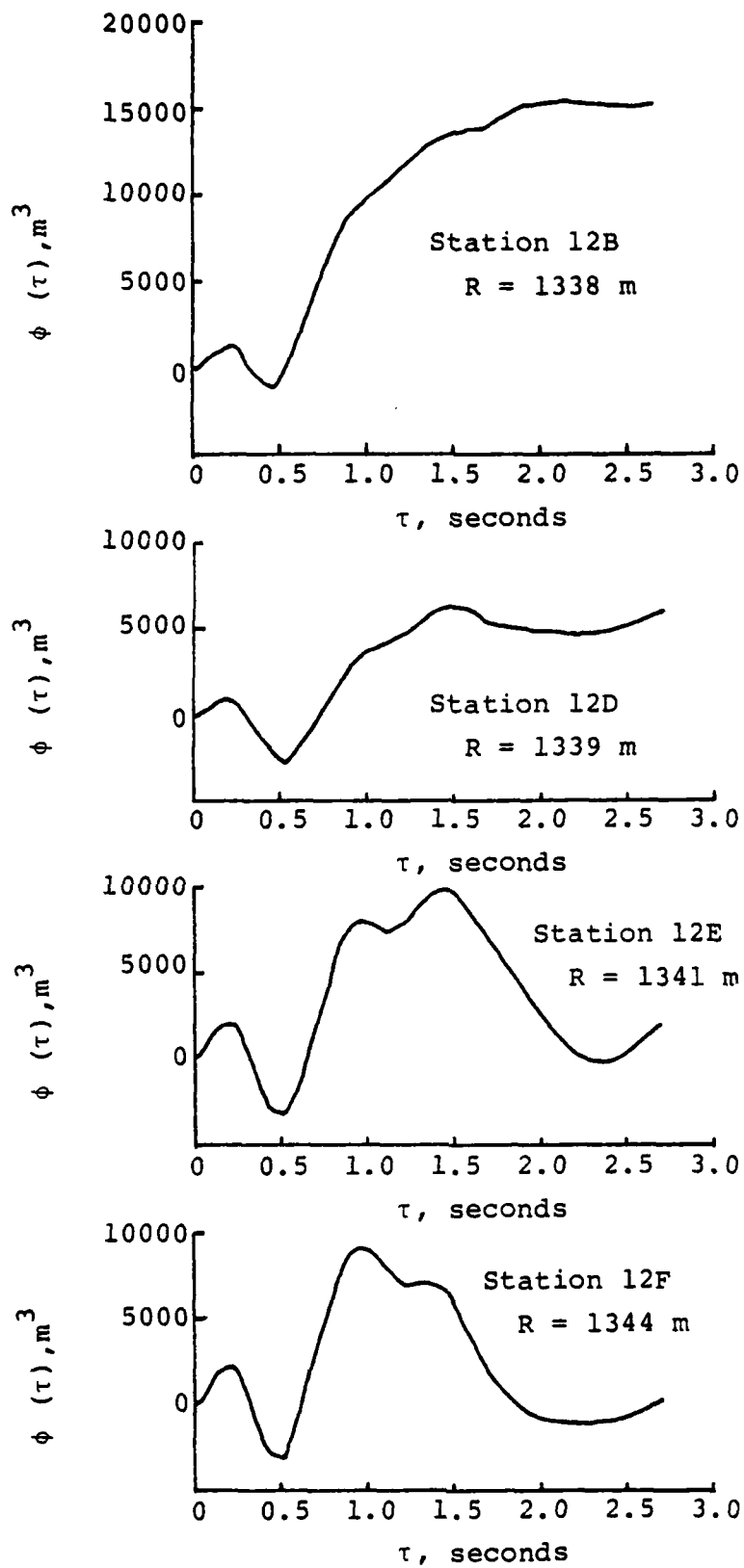
Figure 2.39   Observed Discus Thrower Reduced Displacement
Potentials Derived from Radial Vector Data
Stations 12B, 12D, 12E and 12F.

64
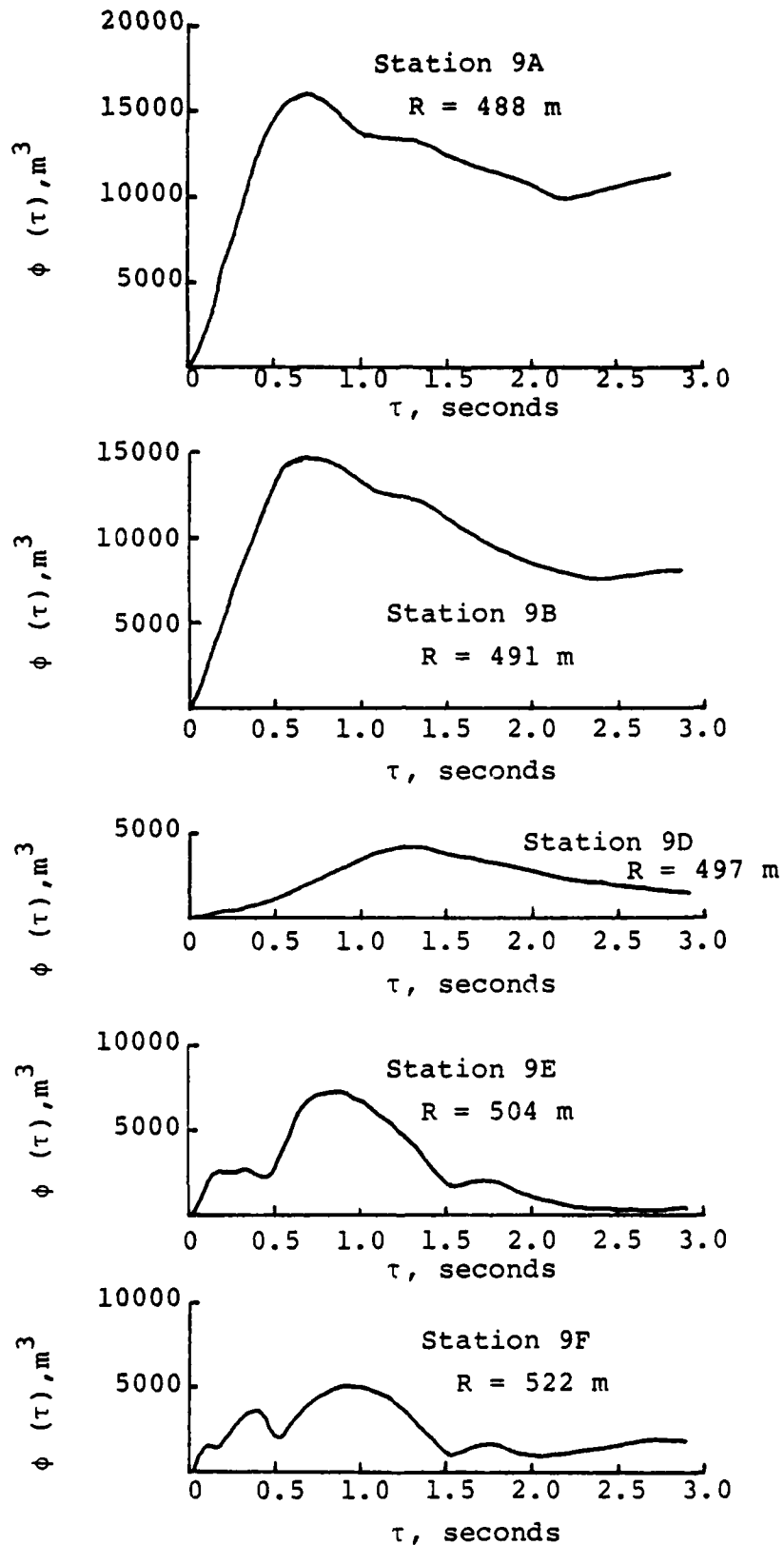
Figure 2.40 Observed Discus Thrower Reduced Displacement
Potentials Derived from Resultant Motion Data
Stations 9A, 9B, 9D, 9E and 9F.
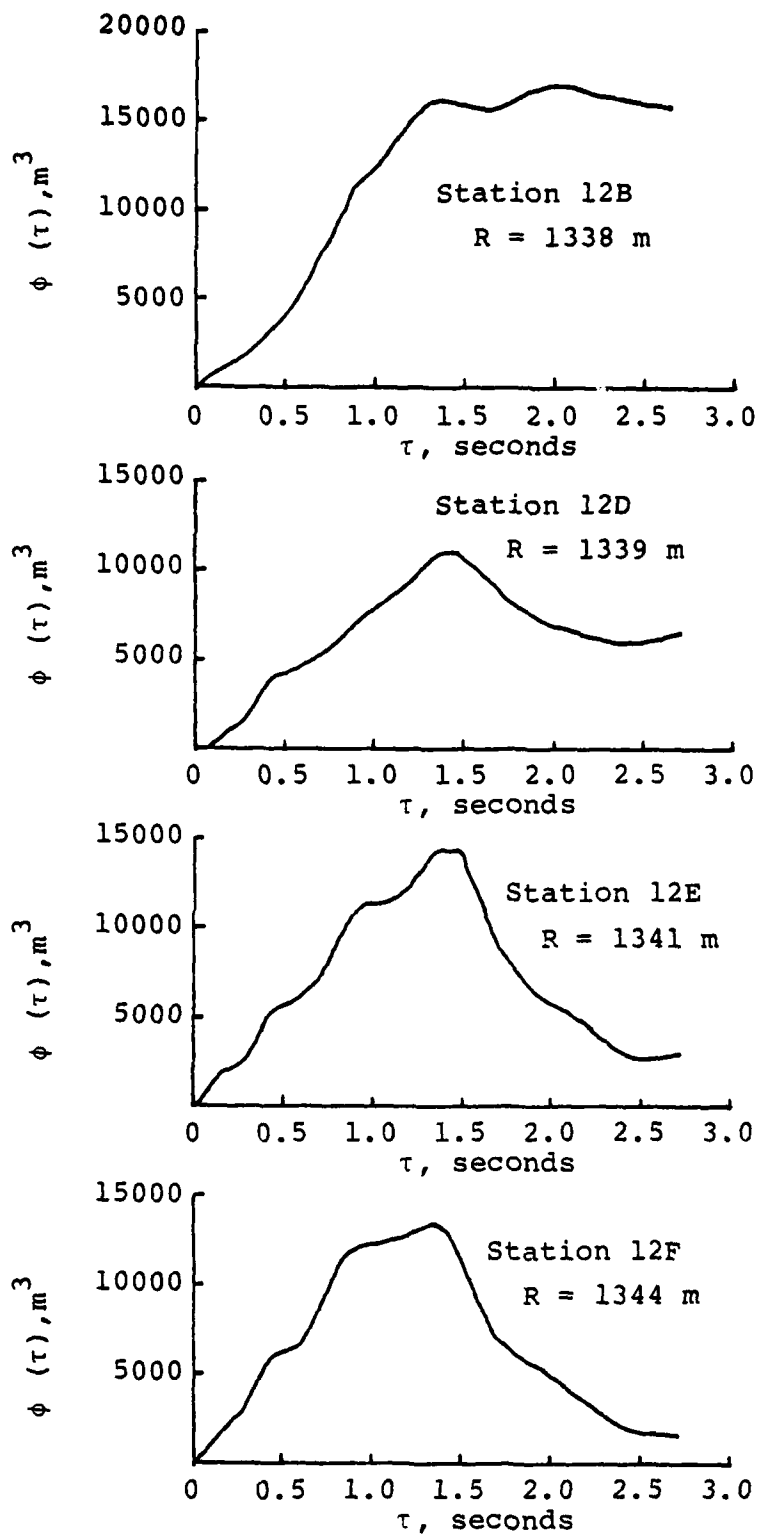
Figure 2.41   Observed Discus Thrower Reduced Displacement
              Potentials Derived from Resultant Motion Data
              Stations 12B, 12D, 12E and 12F.

much lower in amplitude level and different in shape. Possible
effects on the RDP of transmission in the layered geology of the
Discus Thrower site are discussed in detail in Chapter 3.

2.11   Handcar

The Handcar event was a 12 kt contained explosion which
was detonated at a depth of 402 m ($h/W^{\frac{1}{3}}$ = 176 $m/kt^{\frac{1}{3}}$) in dolo-
mite at NTS on November 5, 1964. The measurements discussed here
were obtained from instruments located in 4 drill holes. Three
stations were located at shot depth and the remainder at some-
what higher elevations. The instruments discussed here covered
a range from 122 m to 476 m and were the responsibility of Sandia
Corporation (Perret, 1970b). Radial and vertical components of
acceleration and velocity were measured at each station. Radial
vector motions were derived by resolving the horizontal radial
and vertical motion in the direction of the vector from the shot
to the station. Accelerations and velocities were obtained
directly; displacements were obtained by integrating the radial
vector velocity time histories.

Figure 2.42 is a surface map of the site (Perret, 1970b).
showing the locations of the instrument hole relative to ground
zero. Figure 2.43 shows the locations of the stations on a
vertical plane through the shot point. An approximate subsurface
geologic profile is shown on the left side of the figure. The
geology is the same as that shown above for Mud Pack and consists
of alluvium and tuff layers of nearly the same thickness over-
lying a thin shale layer. Dolomite extends from the bottom of
the shale to below shot depth. A fault not shown on the figure
causes repetition of shale and dolomite layers in the vicinity
of drill hole U10b-4. Except for the stations at shot depth,
the majority of recording instruments were located near the
shale layer: 3 in the shale, 3 just above in the tuff and 3 just
below in the dolomite. Compressional velocities in the layers

N

$\uparrow$

O HOLE U10b-6

100 m

$\longleftrightarrow$

O HOLE U10b-5

O HOLE U10b-4

O HOLE U10b-2

● GROUND ZERO
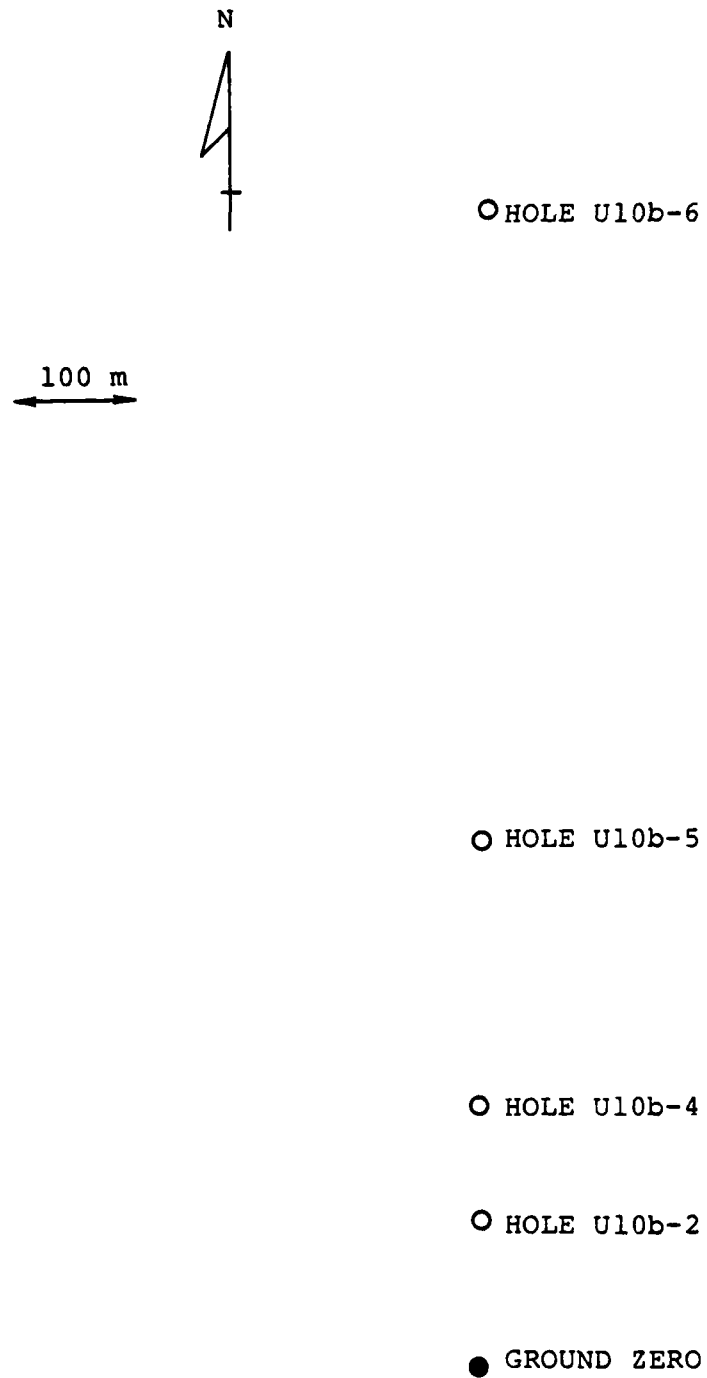
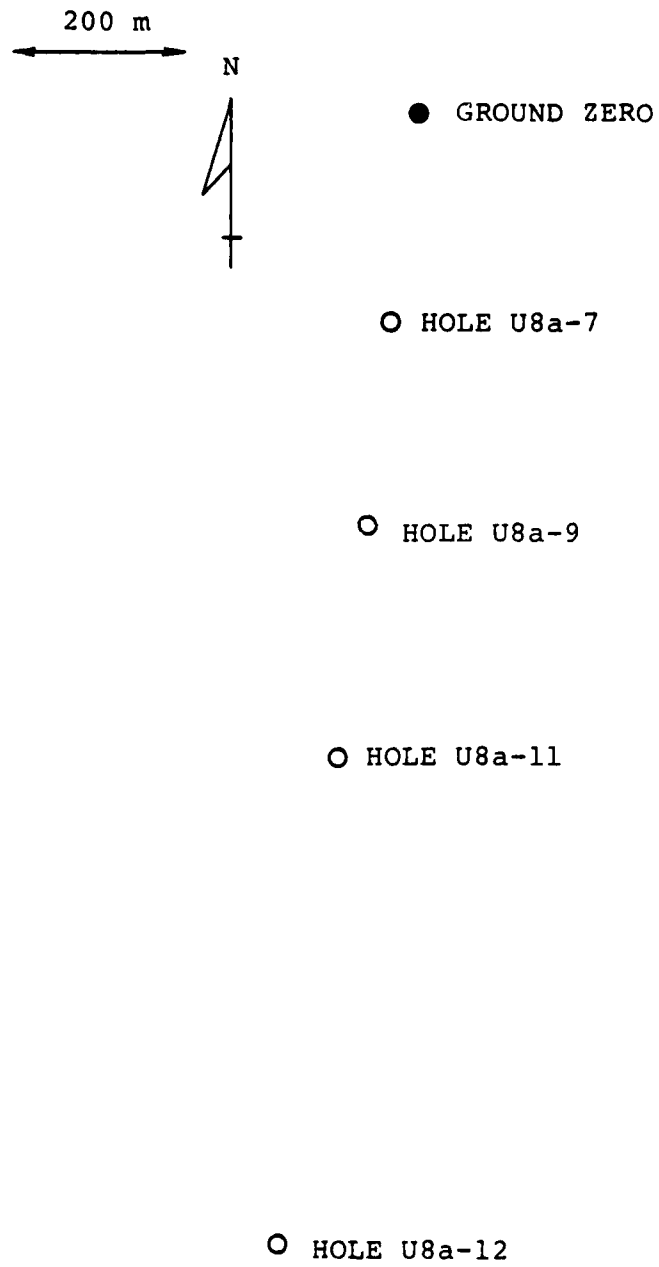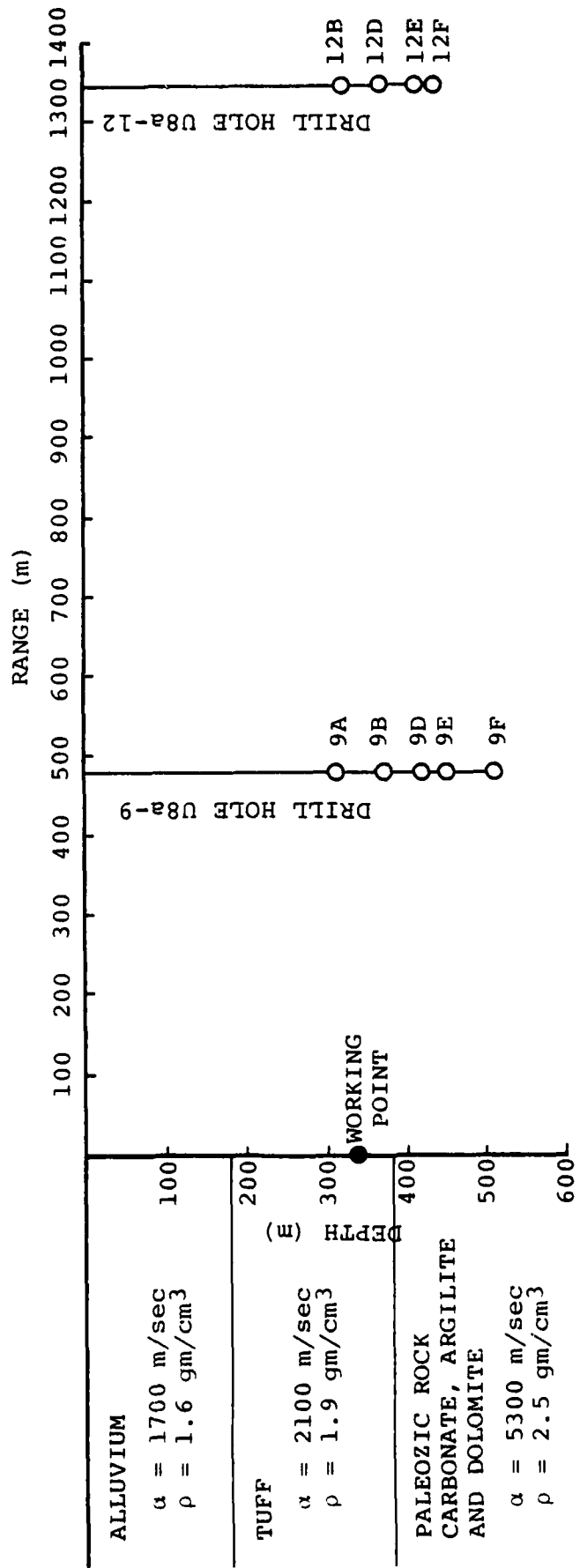Figure 2.42.   Surface Map of the Handcar Site.

Figure 2.43. Vertical Section Through the Handcar Detonation Point Showing the Relationship Between the Instrument Locations and the Subsurface Geology of the Site.

69

were estimated from propagation velocities of direct and re-
fracted arrivals for the Handcar and Mudpack events (Perret,
1970b,c). The densities shown are typical of values for NTS rocks
of the type shown here.

Peak radial vector ground motions for Handcar are shown
in Figure 2.44. Regression analyses were performed on the peak
acceleration, velocity and displacement data. These resulted
in:

$$a_r = 2.04 \times 10^6 \ R^{-2.13}$$

$$v_r = 3.38 \times 10^6 \ R^{-1.76}$$

$$d_r = 2.29 \times 10^7 \ R^{-2.55}$$

Perret (1970b) performed a similar regression analysis using only
data from stations located in shale or dolomite. His analyses
resulted in:

$$a_r = 2.69 \times 10^6 \ R^{-2.18}$$

$$v_r = 3.25 \times 10^6 \ R^{-1.75}$$

$$d_r = 8.23 \times 10^7 \ R^{-2.73}$$

In the range of the data these regression relations are practi-
cally equivalent.

Figures 2.45 through 2.47 show 11 RDP's which we derived
from the subsurface radial vector displacement time histories
for the Handcar event. The derived RDP's show substantial
variations between stations. Records from the station in holes
U10b-2 and U10b-4 above shot depth result in unusually large
RDP amplitudes. The level of the RDP's derived from records
obtained in hole U10b-5 and at the shot depth station in hole
U10b-4 are approximately a factor of 3 lower. Reasons for these
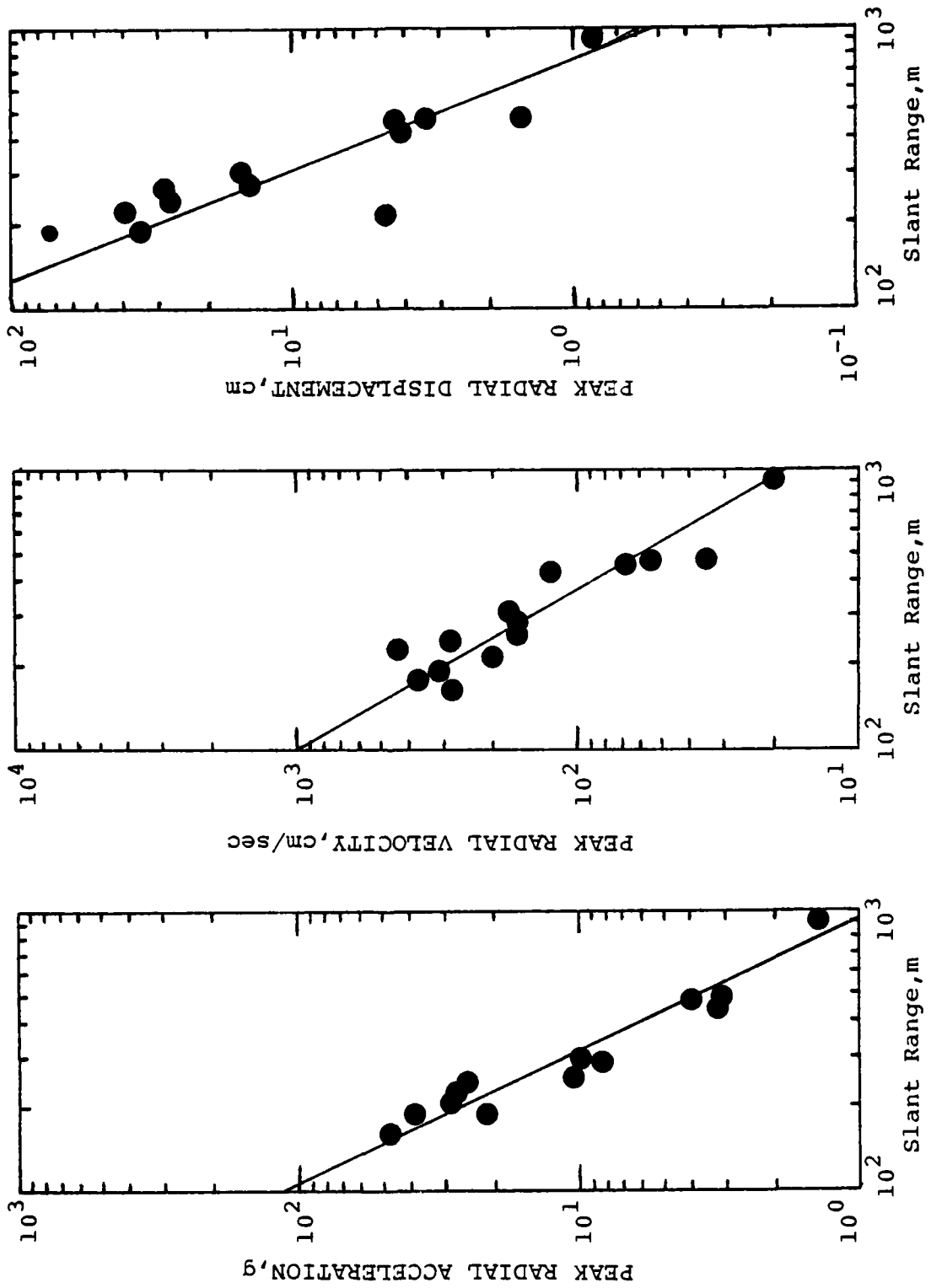
Figure 2.44 Observed Handcar Peak Motion Data as a Function of Range.

71
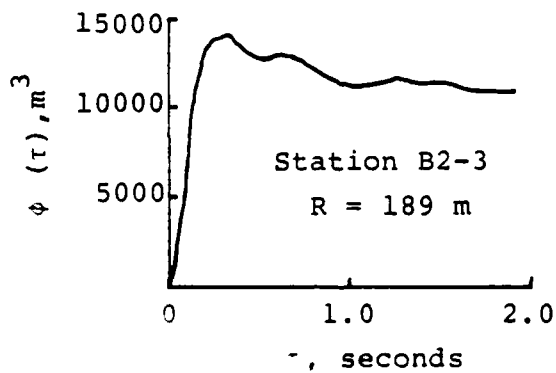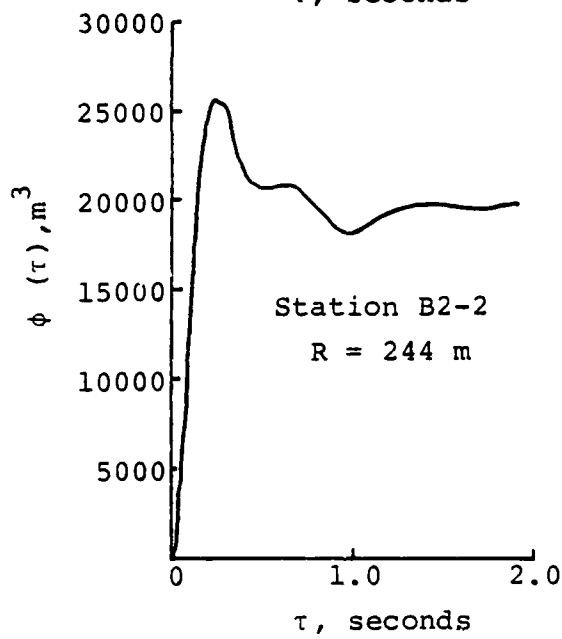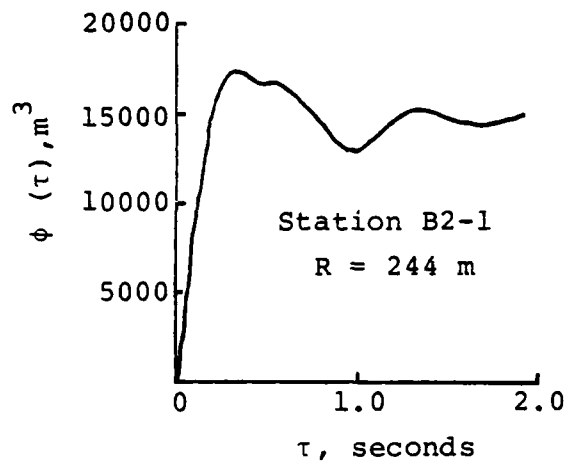
Observed Handcar Reduced Displacement
Potentials Stations B2-1, B2-2 and B2-3.
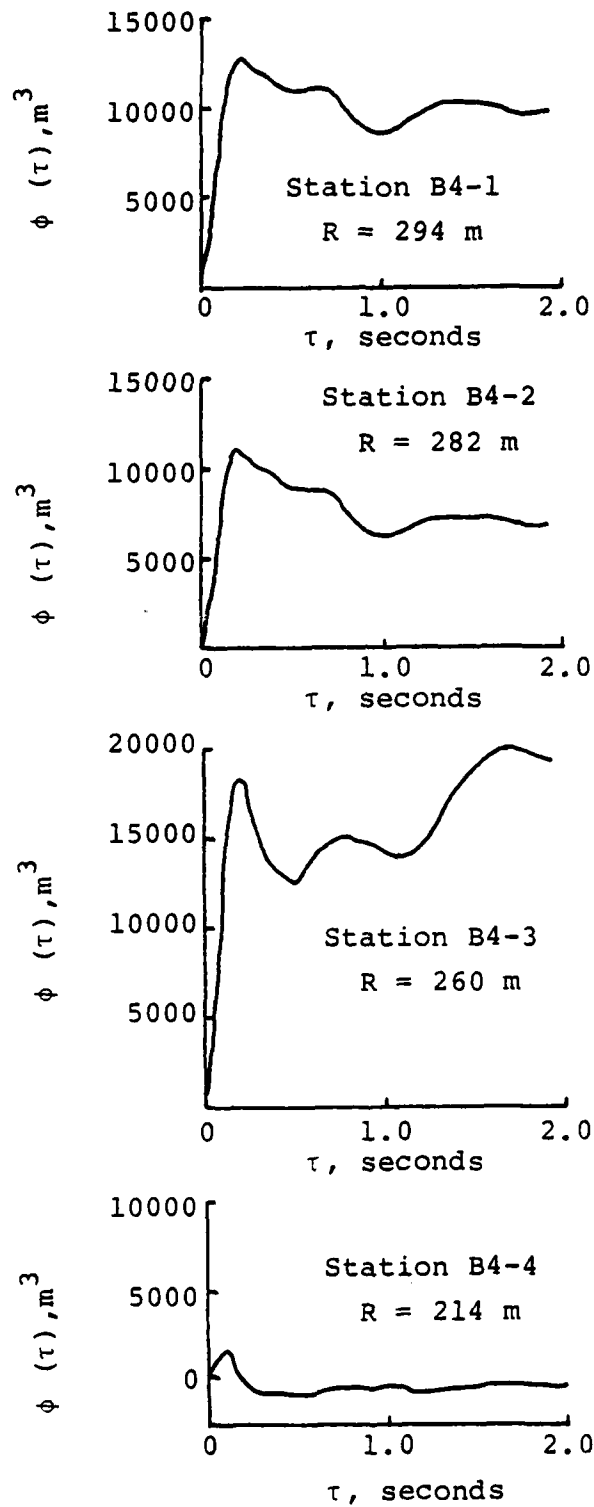
Figure 2.46   Observed Handcar Reduced Displacement
                Potentials Stations B4-1, B4-2, B4-3
                and B4-4.
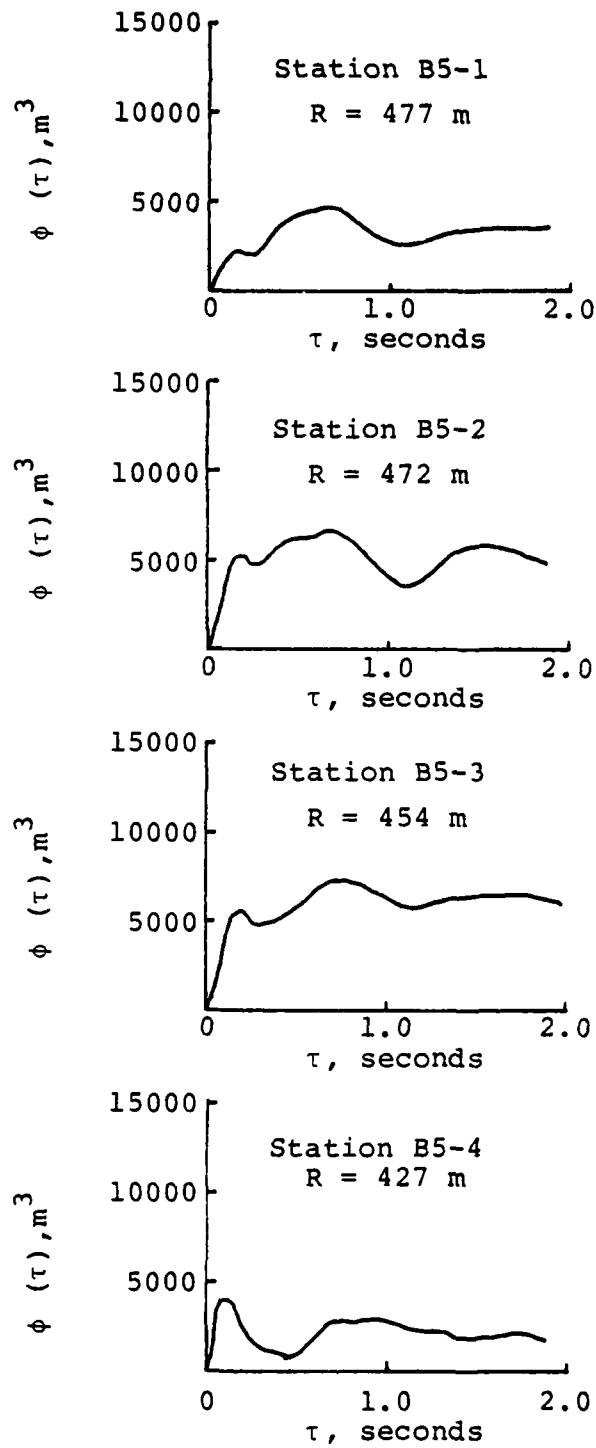
Figure 2.47   Observed Handcar Reduced Displacement Potentials
Stations B5-1, B5-2, B5-3 and B5-4.

differences are not clear but the effects of transmission in
the layered media and possible influences of the fault zone
found in hole U10b-4 seem to be obvious areas for investigation.
The RDP's derived for Handcar will be discussed in more detail
in Chapter III.

2.12   Gasbuggy

The Gasbuggy event was a 29 kt contained explosion which
was detonated at a depth of 1292 m (h/W$^{\frac{1}{3}}$ = 421 m/kt$^{\frac{1}{3}}$) in a
sandstone-shale sequence in the San Juan basin of northern New
Mexico on December 10, 1967. Instrumentation for the event was
positioned near shot depth in a drill hole 457 m from the shot
emplacement hole and was the responsibility of Sandia Corpora-
tion (Perret, 1970a). Four stations were located in the instru-
ment hole at distance ranges between 468 and 556 m from the
source. Each station included instrumentation to record three
components of acceleration and three components of velocity.
Radial vector ground motion was computed from the resolution of
the vertical and horizontal components of motion along the
radial direction from the source to the station. Accelerations
and velocities were measured directly and displacement records
were computed by integrating the velocity time histories.

Figure 2.48 is a surface map of the site (Perret, 1970a)
showing the location of the instrument hole relative to ground
zero. Figure 2.49 shows the locations of recording stations on
a vertical plane through the shot point. An approximate sub-
surface geologic profile is shown on the left side of the figure.
The geologic section consists of a sequence of sandstone and
shale layers (Perret, 1970a). Our simplified model depicts this
as the San Jose formation extending from the ground surface to
near 570 m overlying the Nacimiento formation extending to about
1060 m; compressional wave velocities and densities within these
formations are not readily available. Underlying the Nacimiento

75

N

100 m

● GROUND ZERO

HOLE GB-D
○

Figure 2.48.   Surface Map of the Gasbuggy Site.

RANGE (m)

100	300	500

SANDSTONE AND SHALE SAN
JOSE FORMATION

SANDSTONE AND SHALE
NACIMIENTO FORMATION

DEPTH (m)

```
100
200
300
400
500
600
700
800
900
1000
1100
1200
1300
1400
1500
```

DRILL HOLE GB-D

○ U32

○ U36

CRETACEOUS SANDSTONE AND
SHALE α = 3700 m/sec
           ρ = 2.3 gm/cm^3

SANDSTONE α = 4300 m/sec
           ρ = 2.5 gm/cm^3

○ U41

● WORKING
  POINT

SHALE

α = 4000 m/sec
ρ = 2.6 gm/cm^3

○ U46

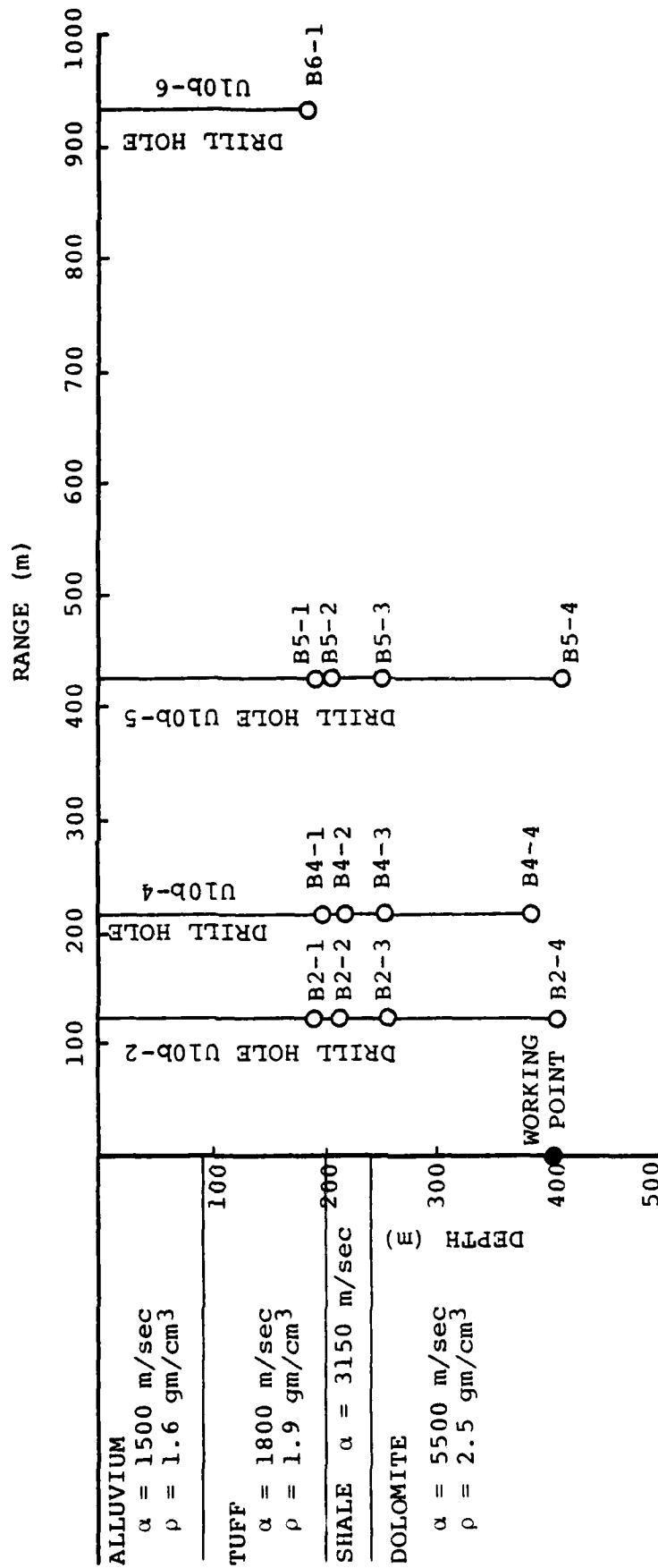Figure 2.49.   Vertical Section Through the Gasbuggy Detona-
               tion Point Showing the Relationship Between
               the Instrument Locations and the Subsurface
               Geology at the Site.

77

formation is a Cretaceous sandstone and shale sequence which overlies a 100 m thick section of Pictured Cliffs sandstone which extends to near shot depth. The emplacement medium for the shot is the Lewis shale which extends to well below shot depth. Compressional velocities and densities were estimated from geophysical logs of the instrument emplacement hole; propagation velocities observed from the shot are generally slightly larger.

The available peak radial vector ground motion data are shown in Figure 2.50. Regression analyses were performed on these data resulting in:

$$a_r = 6.17 \times 10^{15} \ R^{-5.40}$$

$$v_r = 7.94 \times 10^{10} \ R^{-3.20}$$

$$d_r = 1.15 \times 10^{9} \ R^{-3.10}.$$

Although not much reliance can be placed on the derived relationship because of the limited range of distances for which it was derived and the paucity of data points, the calculated attenuation rates are very large. Perret (1970a) did not perform regression analysis on these data but also noted rapid attenuation as a function of range. These apparent rapid attenuation rates can possibly be explained by the layering in the vicinity of the source and the location of the recording instruments within different layers, but additional study will be needed to verify this hypothesis.

Perret (1970a) published four RDP's which were derived from the radial vector displacement time histories from the Gasbuggy event; these are shown in Figure 2.51. Maximum and steady-state levels of these RDP's show variation between stations of only about 20 to 25 percent. The source of this variation is unexplained at this time but it could result from the effects of layering cited above.
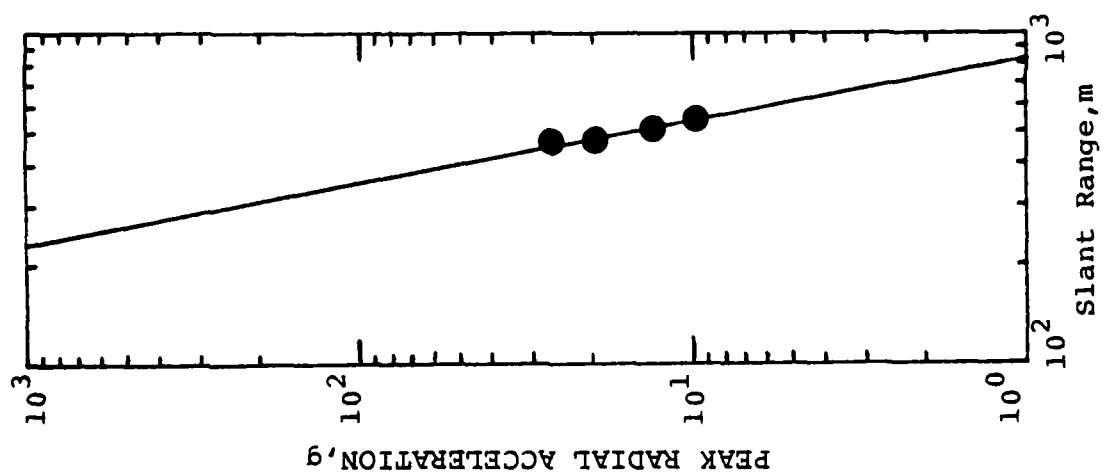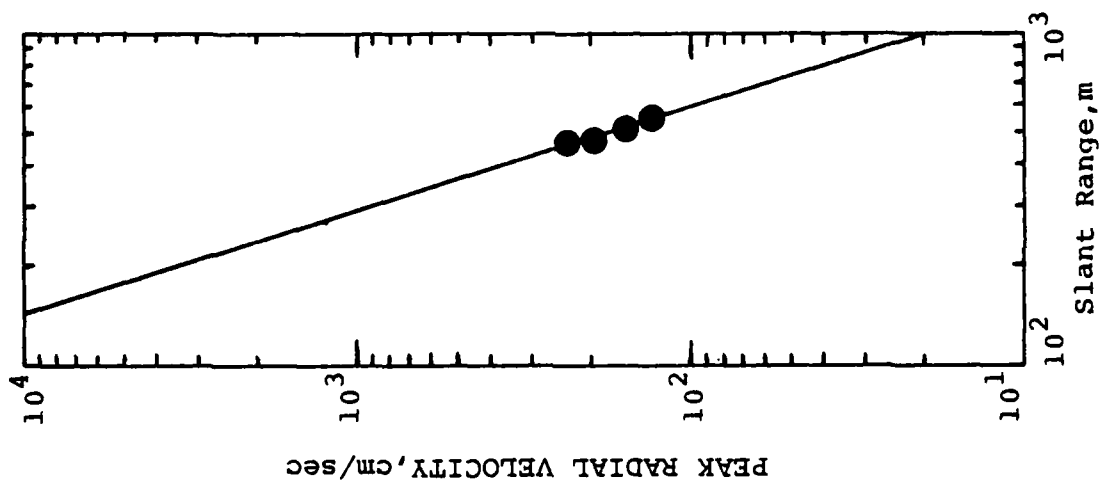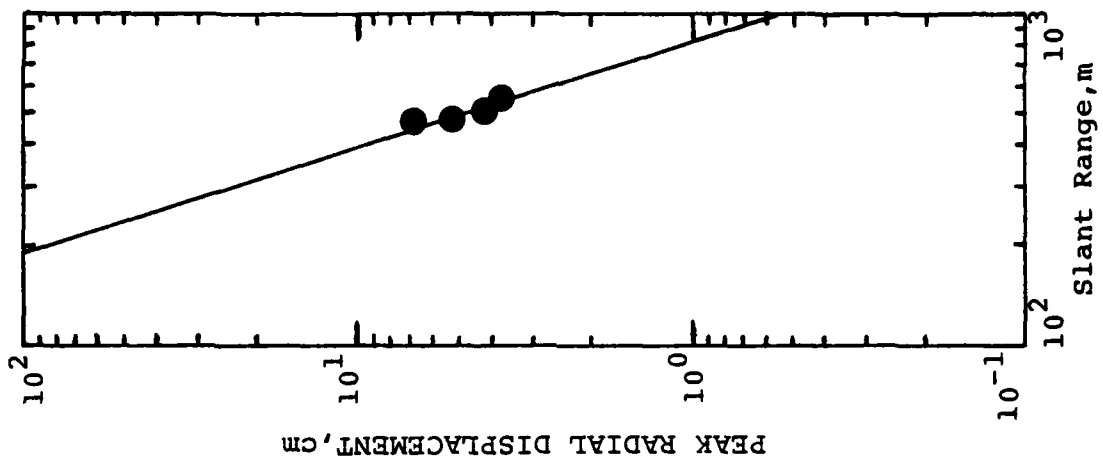
Figure 2.50 Observed Gasbuggy Peak Motion Data as a Function of Range.

79
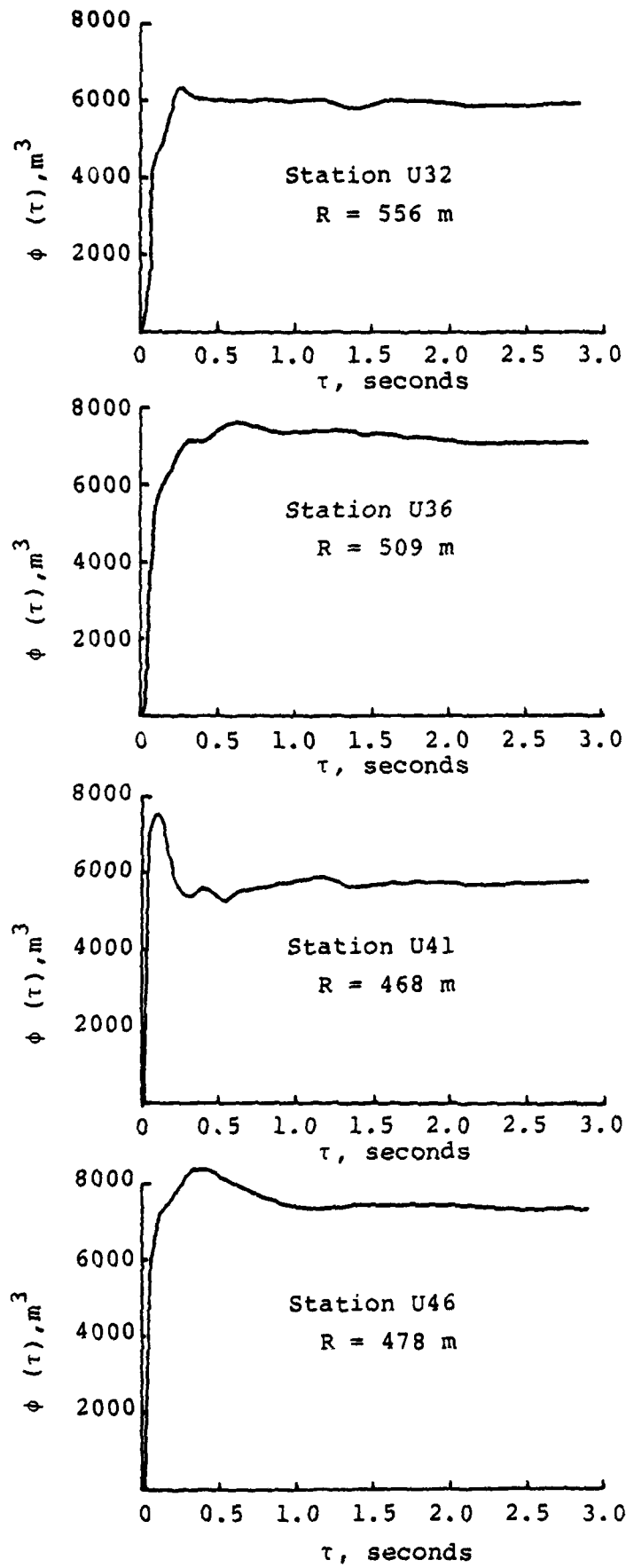
Figure 2.51   Observed Gasbuggy Reduced Displacement
             Potentials Stations 32, U36, U41 and U46.

80

2.13 Milrow

The Milrow event was an approximately 1000 kt contained explosion which was detonated at a depth of 1220 m ($h/W^{1/3}$ = 122 m/kt$^{1/3}$) in pillow lava at the Aleutian Test Site on October 2, 1969. Though no ground motion measurements were made at shot depth, several instruments were located in a drill hole offset 91 m from the shot hole; these were the responsibility of Sandia Corporation (Perret and Breding, 1972). Stations reported here were located at three depths within the drill hole at slant ranges between 616 and 919 m from the shot. Each station was equipped with an accelerometer and a velocity gage oriented to respond to vertical motion which in this case is nearly radial. Two of the three stations were equipped to record accelerations at high and low gains. Accelerations and velocities were measured directly; in one case a velocity was derived by integrating the acceleration time history.

Figure 2.52 is a surface map of the site showing the location of the instrument hole relative to ground zero. Figure 2.53 shows the locations of the stations on a vertical plane through the shot point. An approximate subsurface geologic profile is shown on the left side of the figure. The geologic section is quite complex consisting of a sequence of breccia, sandstone, andesite, basalt, siltstone and pillow lava. The section we show is simplified in consideration of the compressional velocities and densities of the rock layers which were obtained from geophysical logs of the instrumentation hole (Perret and Breding, 1972).

The peak ground motion data for the Milrow event are presented in Figure 2.54. Regressions were performed on the peak accleration and velocity measurements; these resulted in:
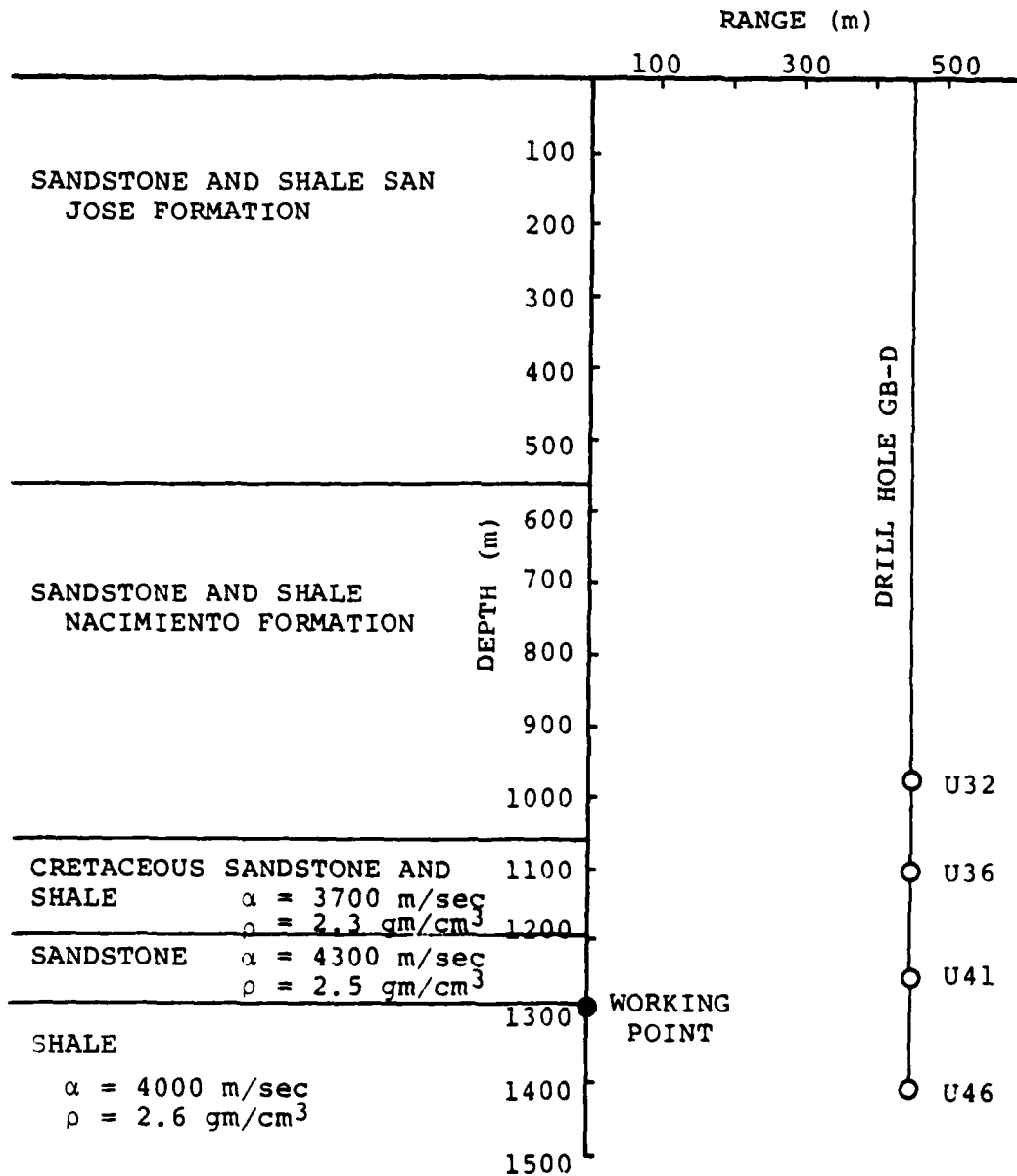
81
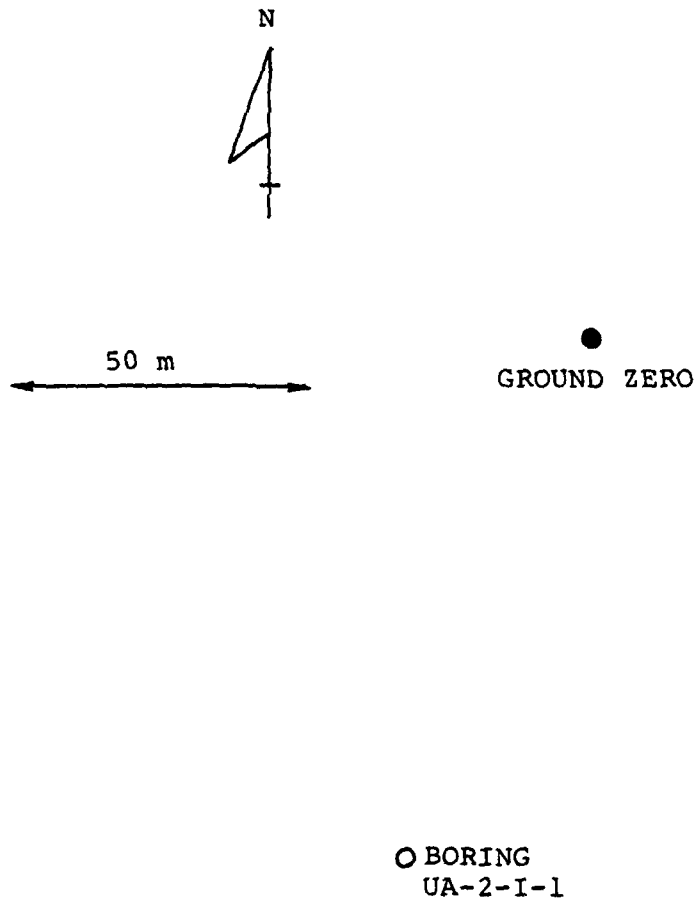
Figure 2.52.   Surface Map of the Milrow Site.
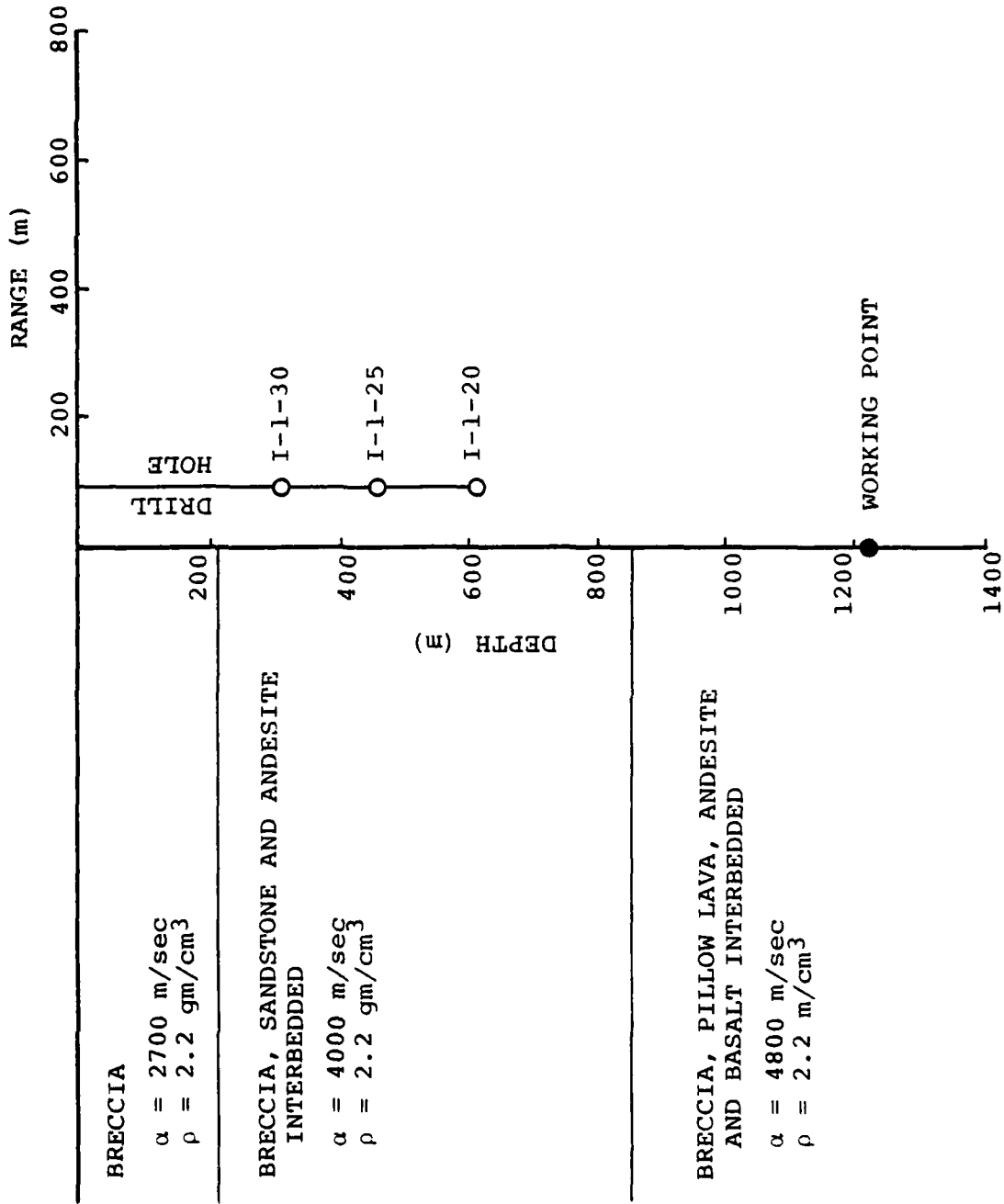
Figure 2.53. Vertical Section Through the Milrow Detonation Point Showing the Relationship Between the Instrument Locations and the Subsurface Geology at the Site.

83
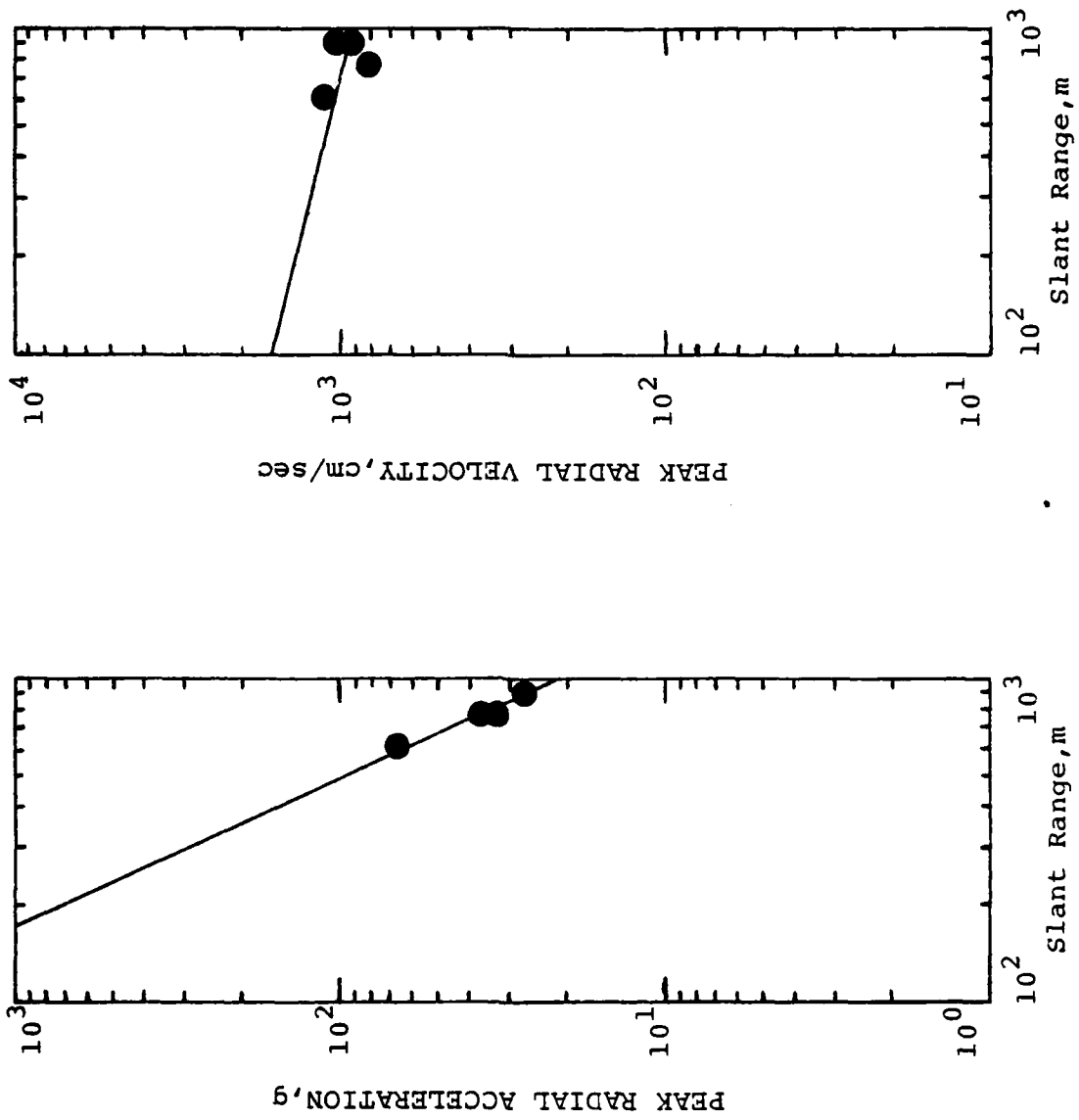
Figure 2.54 Observed Milrow Peak Motion Data as a Function of Range.

$$a_r = 7.24 \times 10^7 \, R^{-2.17}$$

$$v_r = 5.62 \times 10^3 \, R^{-.26}.$$

The attenuation of acceleration with distance seems reasonable but the attenuation of velocity appears low. Displacement time histories do not peak until after arrival of the reflection from the free surface.

No RDP's are available for this event.

2.14 Cannikin

The Cannikin event was an approximately 5000 kt contained explosion which was detonated at a depth of 1791 m ($h/W^{\frac{1}{3}} = 105$ $m/kt^{\frac{1}{3}}$) in pillow lava at the Aleutian Test Site on November 6, 1971. No ground motion measurements were made at shot depth, but several instruments were located in a deep drill hole off-set 91 m from the shot hole; these were the responsibility of Sandia Corporation (Perret, 1973). Stations reported here were located at five depths within the drill hole at slant ranges between 754 and 1477 m from the shot. Each station was equipped with an accelerometer and a velocity gage oriented to respond to vertical motion which in this case is nearly radial. Three of the stations recorded accelerations at both high and low gains. Accelerations and velocities were measured directly; velocities were also derived by integrating the acceleration time histories.

Figure 2.55 is a surface map of the site showing the location of the instrument hole relative to ground zero. Figure 2.56 shows the locations of the stations on a vertical plane through the shot point. An approximate subsurface geologic profile is shown on the left side of the figure. The actual geologic section is quite complex consisting of inter-bedded breccia, siltstones, basalts, sandstone, andesite and

85

N

50 m

●
GROUND ZERO

O HOLE UAe-1
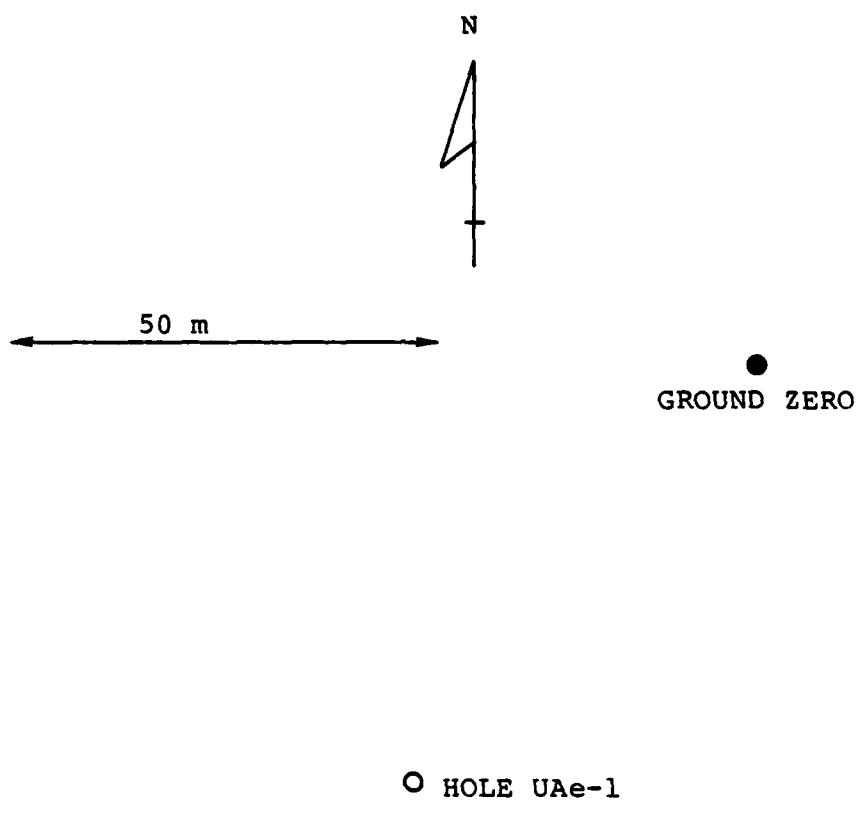
Figure 2.55. Surface Map of the Cannikin Site.

RANGE (m)

200   400

BRECCIA AND SILTSTONE INTERBEDDED

α = 3000 m/sec
ρ = 2.3 gm/cm^3

BRECCIA AND BASALT INTERBEDDED

α = 3700 m/sec
ρ = 2.4 gm/cm^3

BRECCIA AND BASALT INTERBEDDED

α = 4200 m/sec
ρ = 2.4 gm/cm^3

BRECCIA, BASALT AND PILLOW
  LAVA INTERBEDDED
α = 4700 m/sec
ρ = 2.4 gm/cm^3

ANDESITE

α = 5500 m/sec
ρ = 2.6 gm/cm^3

DRILL HOLE

I50

I45

I40

I30

I25

WORKING POINT

DEPTH (m)

200
400
600
800
1000
1200
1400
1600
1800
2000

Figure 2.56.   Vertical Section Through the Cannikin Detona-
               tion Point Showing the Relationship Between
               the Instrument Locations and the Subsurface
               Geology at the Site.

pillow lava. We have simplified the section shown here in consideration of the compressional velocities and densities of the rock layers which were obtained from geophysical logs of the instrument emplacement hole (Perret, 1973).

Peak ground motion data for the Cannikin event are presented in Figure 2.57. Regression analyses were performed on the peak accelerations and velocities; these resulted in:

$$a_r = 1.38 \times 10^{11} \, R^{-3.17}$$

$$v_r = 5.01 \times 10^8 \, R^{-1.85}.$$

Peak free-field displacements could not be determined either because of instrument failure prior to their occurrence or because the records were contaminated by reflection from the free surface.

No RDP's are available for this event.
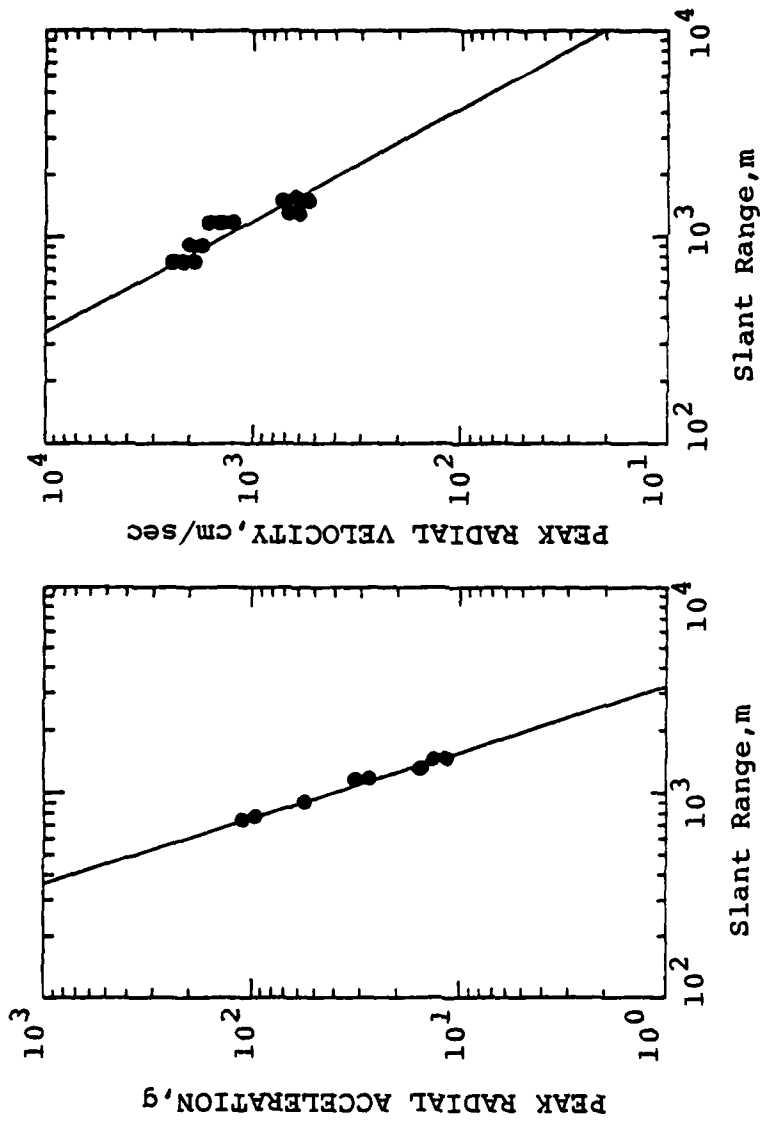
Figure 2.57. Observed Cannikin Peak Motion Data as a Function of Range.

89

III. ANALYSIS OF FREE-FIELD GROUND MOTION FOR THE HANDCAR, DISCUS THROWER AND MERLIN EVENTS

3.1 Overview

In compiling the ground motion data for Chapter II, we identified data for three events (Handcar, Discus Thrower and Merlin) which could have important bearing on outstanding issues concerning the definition of the nuclear seismic source function. In particular, the Handcar event was detonated in carbonate rock and was initially expected to result in high coupling efficiency because of the release of noncondensable gases in the emplacement medium. However, teleseismic data from Handcar indicated low coupling. The Discus Thrower event was emplaced near the geologic interface between tuff and underlying Paleozoic rock, and data from the event would be expected to reveal any nonlinear effects arising from proximity to this boundary. Ground motion measurements near shot depth for the Merlin event revealed the presence of a relatively low frequency signal delayed in time which appeared to be related to spall closure and which could be significant in the radiated seismic signal. In this chapter we will take a closer look at these three events focusing on what the free-field ground motion data reveal about their source characteristics.

3.2 Handcar

The Handcar event is of particular interest because it was detonated in dolomite and showed relatively low coupling based on the observed m_b. It was originally believed that the Handcar explosion would release permanent, noncondensable gases (i.e. CO and CO_2) at high pressure in the dolomite producing increased ground motion coupling efficiency (Perret, 1970b). In fact, however, just the opposite effect was observed and the m_b

value for Handcar was more than 0.15 magnitude units below the value expected for an event of the same yield detonated in a wet tuff emplacement medium. The available data from other detonations in carbonate rock are widely scattered. However, they do generally indicate low coupling and, in some cases, fall into the dry alluvium population. However, it is difficult to assess the significance of these data due to the fact that all these other events were detonated within about one cavity radius of the tuff/carbonate contact and thus may not be representative of detonations in carbonate rock. In any case, the Handcar teleseismic m_b data clearly indicate low coupling. A possible clue to the anomalous seismic coupling is the fact that the final cavity radius for Handcar, as measured by Boardman et al. (1966) is unusually small. This is documented below where the observed cavity radius for Handcar is compared with the average cavity radii expected for events of that yield and depth of burial in various other source media.

Observed Handcar	r_c = 22m
Granite	r_c = 27m
Salt	r_c = 30m
Alluvium	r_c = 31m
Wet Tuff	r_c = 33m

Now, the steady state value of the reduced displacement potential, $\phi\ (\infty)$, is related to r_c by the proportionality relationship

$$\phi\ (\infty) \sim \frac{r_c{}^3}{3} \ . \tag{3-1}$$

For wet tuff the proportionality constant in (3-1) has been found to be about 0.6. Then, even assuming that the dolomite is incompressible, we have for the Handcar yield and depth of burial:

$$\phi(\infty)\big|_{Handcar} \simeq 3550 \text{ m}^3$$

$$\phi(\infty)\big|_{Wet \ Tuff} \simeq 7450 \text{ m}^3.$$

Now for events in a given source region

$$m_b = C + \log\left[\alpha \cdot \hat{\psi} \ (1\text{Hz})\right] \qquad (3\text{-}2)$$

where C is a propagation path constant, $\hat{\psi}$ (1 Hz) is the Fourier transform of the reduced velocity potential evaluated at 1 Hz and α is the compressional wave velocity of the source medium. But, for yields less than about 50 kt,

$$\hat{\psi} \ (1 \text{ Hz}) \simeq \phi(\infty) \qquad (3\text{-}3)$$

and it follows that on the basis of the difference in cavity radii one would expect for the Handcar yield and depth of burial

$$m_{b \ wet \ tuff} - m_{b \ Handcar} \simeq \log\left[\frac{(7450) \quad (3500)}{(3550) \quad (5500)}\right] \simeq 0.13$$

$$(3\text{-}4)$$

where average compressional wave velocities of 3500 m/sec and 5500 m/sec have been assumed for wet tuff and dolomite respectively. This calculated value is remarkably close to the observed teleseismic magnitude residual of 0.16 magnitude units, suggesting that the observed coupling anomaly can be explained in terms of the observed cavity radius. Thus, contrary to the pre-shot expectation, the cavity radius for Handcar was unusually small, independent of the fact that a relatively large volume of permanent gas was produced by the explosion.

Since there was an abundance of ground motion measurements near shot level for this event, we decided to take a closer look at these data to determine what assistance they

could offer in explaining the observed anomaly. Considering the strong geologic layering of the Handcar site (cf. Figure 2.43), it was immediately apparent that stations at depths above shot level were likely to be contaminated by reflected phases generated at the interfaces between the dolomite and shale and between the shale and tuff layers. In fact, the RDP's derived for these stations, particularly for holes B2 and B4 (cf. Figures 2.45 through 2.47), show unusually large amplitudes. This may in part be attributable to some of the nearer stations being in the strongly inelastic region but appears to be mainly caused by wave interaction at the interfaces. This is the most obvious for the three stations nearest the interfaces in each hole where the derived RDP's differ by nearly a factor of two over a very small range in distance. The high levels of the RDP's at these stations are also inconsistent with the steady-state RDP derived for the small cavity radius measured for Handcar as described above, differing by about a factor of three to five. Stations at shot depth were less likely to contain such perturbations and, in fact, station B5-4 appeared to provide a fairly reasonable RDP (cf. Figure 2.47). However, even for this station some departures from the free-field condition were noted. The low levels of the RDP's for station B4-4 and for the other stations in hole B5 tend to corroborate the B5-4 observation. However, it should be noted that after about 0.2 seconds the RDP at station B4-4 has little validity since the original records indicate instrument failure at about this time.

Figure 3.1 shows the radial and vertical components of displacement measured at station B5-4 for Handcar. Because station B5-4 is located at shot depth, the vertical component of motion would be expected to vanish in the absence of layering or other departures from spherical symmetry. In fact, however, the magnitude of the vertical component of motion at Station B5-4 is comparable to that of the radial component. Moreover, the time history for the radial component of motion is unusual

93
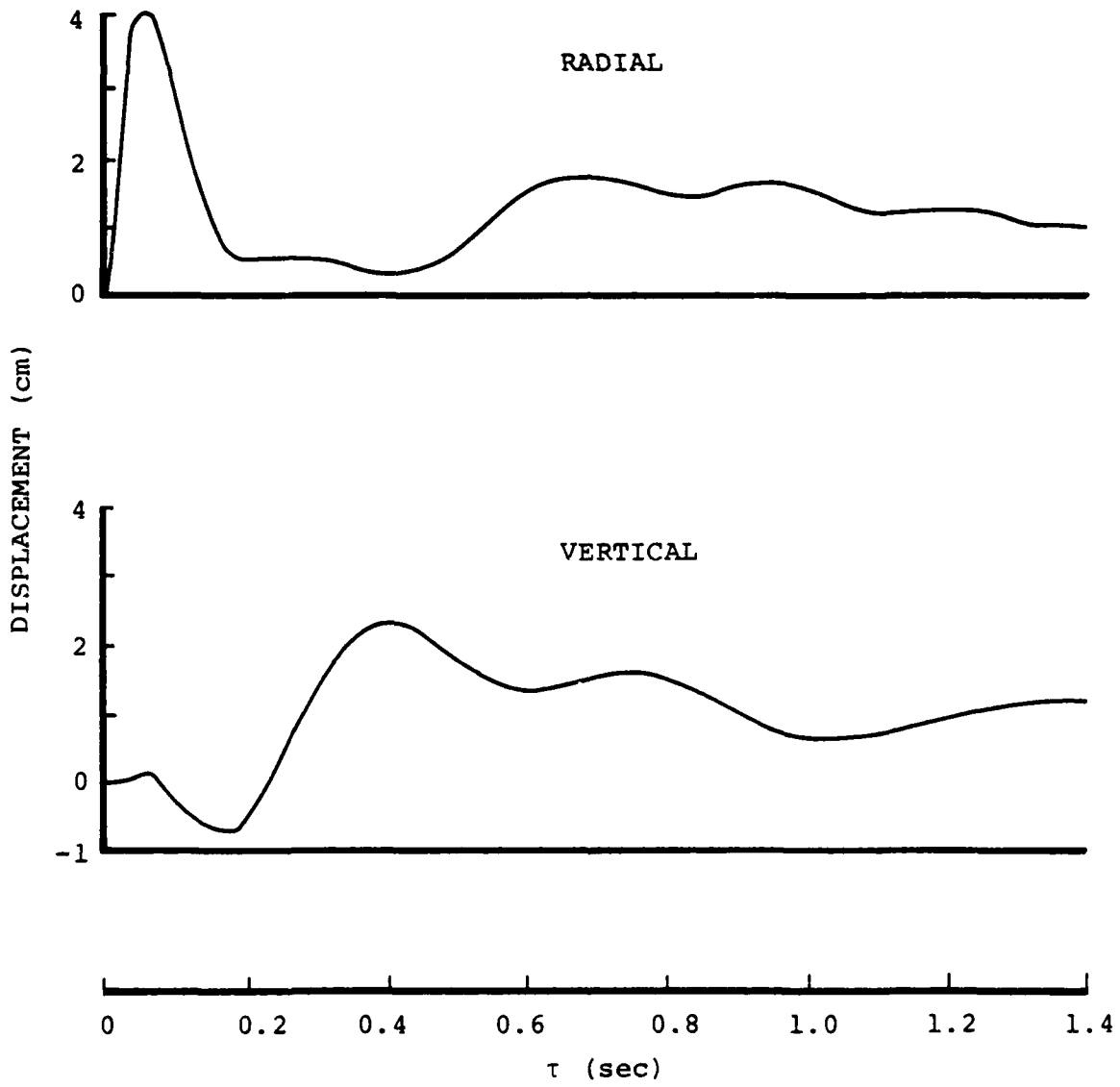
Figure 3.1. Radial and Vertical Components of Displacement
Observed at Station B5-4 for Handcar.

94

in that it exhibits a prolonged period of low displacement prior to rising to its "steady-state" level. These observations suggest that reflected arrivals must be modifying the observed radial displacement.

This condition can be crudely approximated by assuming that the motion recorded on the vertical component is due to reflected compressional wave arrivals of combined amplitude $\tilde{D}(t)$ which propagate at an angle θ with respect to the downward vertical. Then, denoting the amplitude of the radial displacement from the direct arrival as $D(t)$, it follows that the radial, $D_r(t)$, and vertical, $D_z(t)$, components of the total displacement can be written as

$$D_r(t) = D(t) + \tilde{D}(t) \sin \theta \qquad (3-5)$$

$$D_z(t) = \tilde{D}(t) \cos \theta \qquad (3-6)$$

and then

$$D(t) = D_r(t) - D_z(t) \tan \theta. \qquad (3-7)$$

This last relationship was used to correct the radial component of displacement observed at station B5-4. An angle of incidence of $\theta = 30°$ was assumed for the direction of propagation of the reflected compressional arrivals. Figure 3.2 shows a comparison of the observed radial displacement from station B5-4 with the computed "corrected" radial displacement. It can be seen that the "corrected" displacement more nearly resembles the radial displacement expected in a homogeneous medium in that it settles down to a "steady-state" level in a time frame which is reasonable in terms of the explosive process itself. In addition, the level of the steady-state radial displacement, about 2 cm, is consistent with a final cavity radius of 22 m (assuming incompressibility). This value closely matches the observed cavity radius
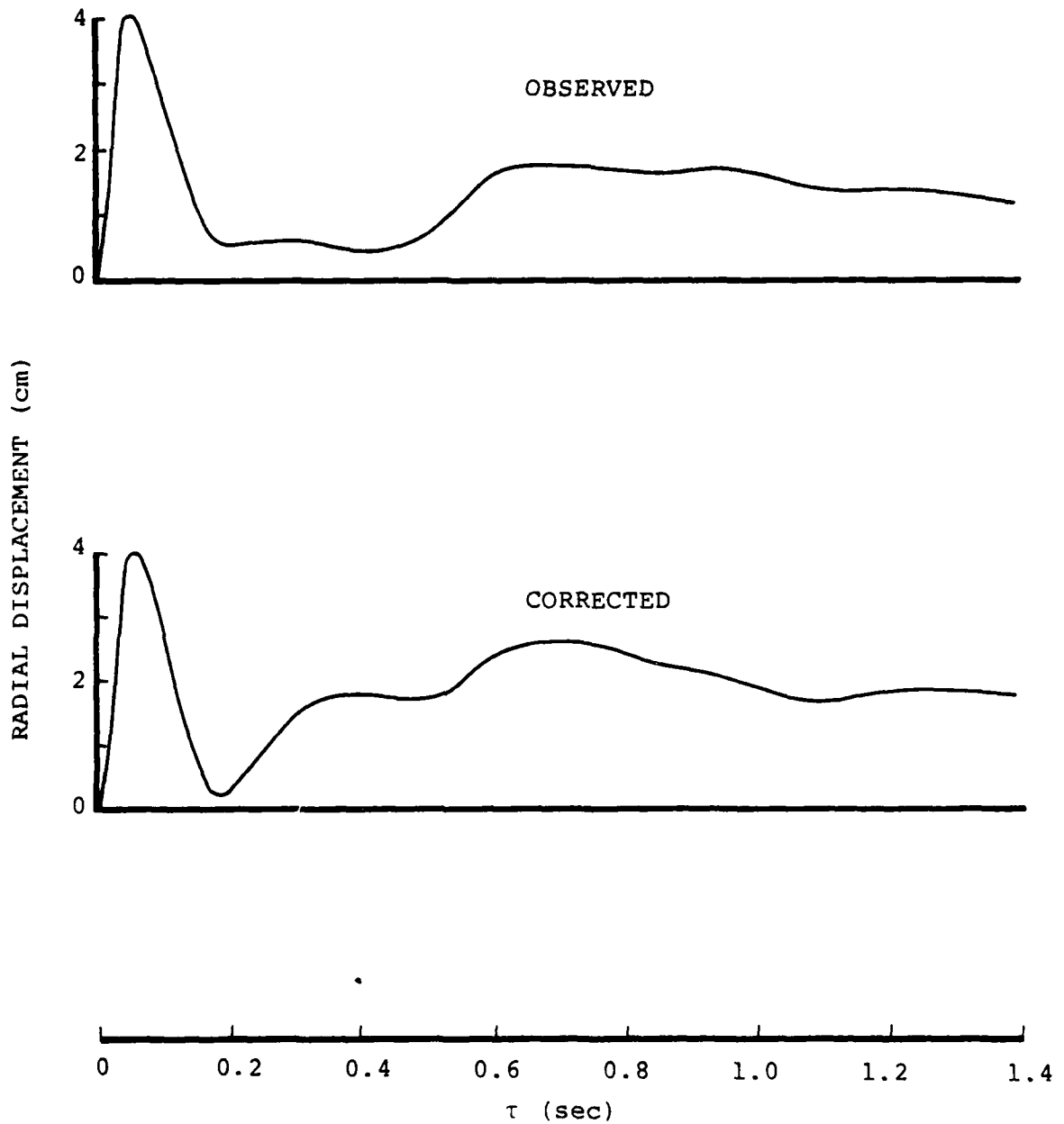
Figure 3.2.   Comparison of the Observed Radial Displacement
With the Corrected Radial Displacement at Station
B5-4 for Handcar.

from Handcar and thus tends to support the validity of the corrected displacement.

Assuming the pressure profile at the elastic radius, r_{el}, can be approximated by an analytic expression of the form

$$p(t) = \left| P_O e^{-\lambda t} + P_{OC} \right| H(t) \qquad (3-8)$$

where P_{OC} is the steady-state pressure determined from the cavity radius, $(P_O + P_{OC})$ is the peak shock pressure estimated from velocity data, $\lambda \simeq 2\alpha/r_{el}$, α is compressional wave velocity, and $H(t)$ is a step function, then the theoretical radial displacement at any range can be estimated. By matching the radial displacement calculated analytically for different values of the elastic radius with the corrected radial displacement described above for Handcar, we can determine the elastic radius for Handcar. Such a match is shown in Figure 3.3 for assumed elastic radii of 250 m and 350 m. The better match results for an assumed elastic radius of 250 m as the pulse width resulting from the 350 m elastic radius is clearly too long. The biggest discrepancy between the displacement derived analytically and that observed is the relatively low value occurring immediately following the initial peak. There is no obvious explanation for this. If the motion were due to reflected compressional waves, a strong vertical component would be expected. In this case, the vertical motion is close to zero at the time of the minimum radial displacement so that resultant motion at this time is nearly radial. SV waves propagating nearly vertically could produce motion of this type, but we have not considered this possibility in detail. A more likely explanation is that the actual pressure profile acting at the elastic radius is more complex than the simple approximation assumed in equation (3-8) above.

Figure 3.4 shows a comparison of the RDP observed for Handcar with one computed for the analytic model of the source
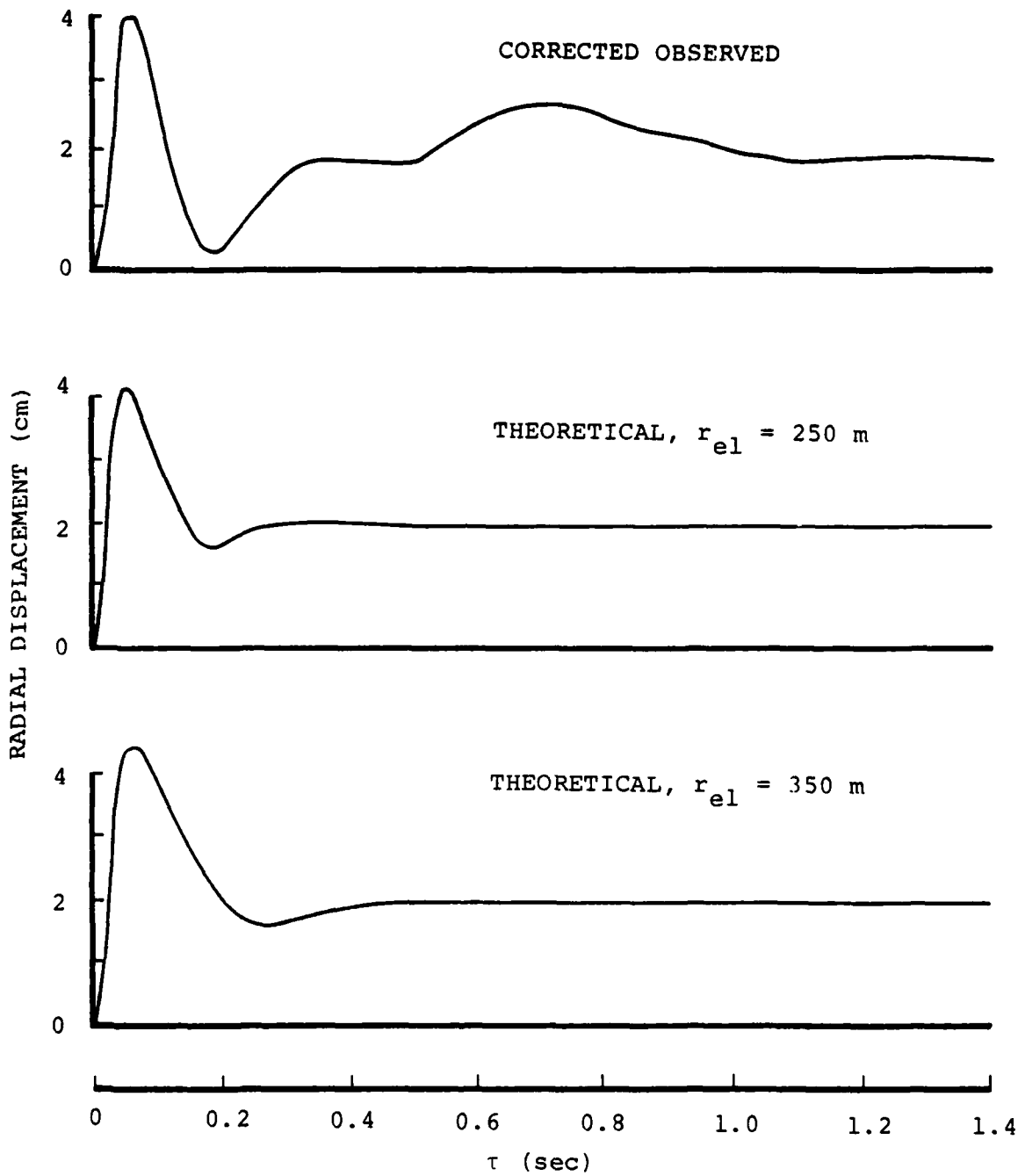
Figure 3.3. Comparison of the Observed Radial Displacement at Station B5-4 for Handcar With the Theoretical Radial Displacements Corresponding to Assumed Elastic Radii of 250 m and 350 m.
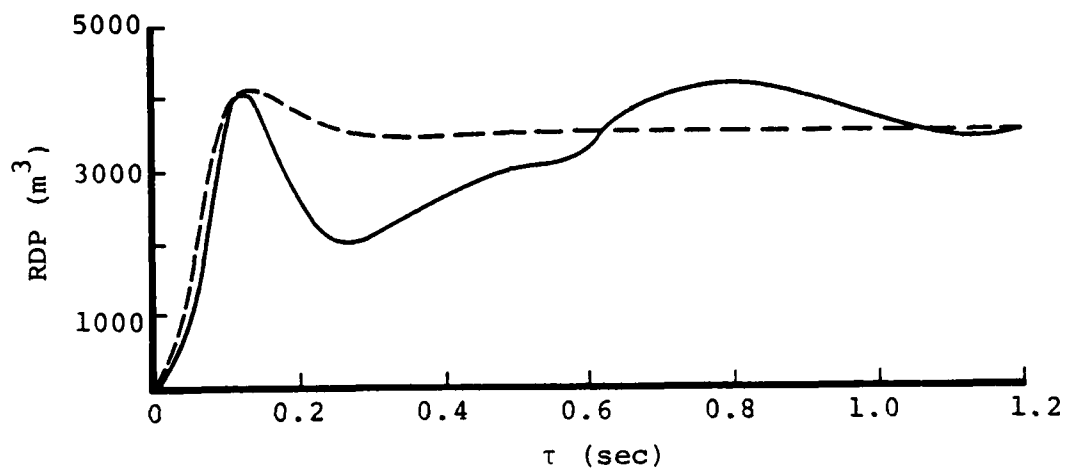
Figure 3.4.   Comparison of the Observed Reduced Displacement
Potential for Handcar With the Reduced Displace-
ment Potential Derived Using the Analytic Model
of the Source for an Elastic Radius of 250 m.

99

described above for an elastic radius of 250 m. As would be
expected from the earlier displacement comparison, the agree-
ment in amplitude level between the computed and observed poten-
tial functions is good. Thus, ground motion measurements in the
free-field at shot depth appear to be consistent with the small
cavity radius observed for the Handcar event.

Given the reasonableness of the RDP for Handcar determined
from station B5-4, we can compare it with potential functions
for explosions in other media to see better the relative coupling
of the Handcar event. Figure 3.5 shows a comparison of the Hand-
car RDP with predicted RDP's for events of equivalent yield (12
kt) in wet tuff and salt. The wet tuff curve is the predicted
potential for the Handcar yield and depth of burial while for
the salt potential observed Salmon data were simply cube-root
scaled to 12 kt. The comparison indicates that coupling in
Handcar was very low with respect to the other source media.

Finally, Figure 3.6 shows frequency domain relative cou-
pling functions (i.e. $\alpha \cdot \hat{\Psi} (\omega)$, cf. equation [3-2]) for Handcar
and for an explosion in wet tuff. As noted previously, the
difference in amplitude level at 1 Hz represents a teleseismic
magnitude, m_b, difference of about 0.13 units. However, the
Handcar spectrum shows considerably more overshoot of the DC
value than does the wet tuff spectrum. Assuming this difference
is not yield dependent, the observed body wave magnitude anomaly
could be significantly reduced at higher yields where the peak
of the dolomite spectrum moves into the teleseismic passband.
This effect could be contributing to the observed scatter in
m_b data from other dolomite events.

In conclusion, the available evidence continues to indi-
cate that dolomite is a low coupling medium for low yield events.
Both free-field and teleseismic ground motion data from Handcar
can be explained by the unusually small cavity radius for that
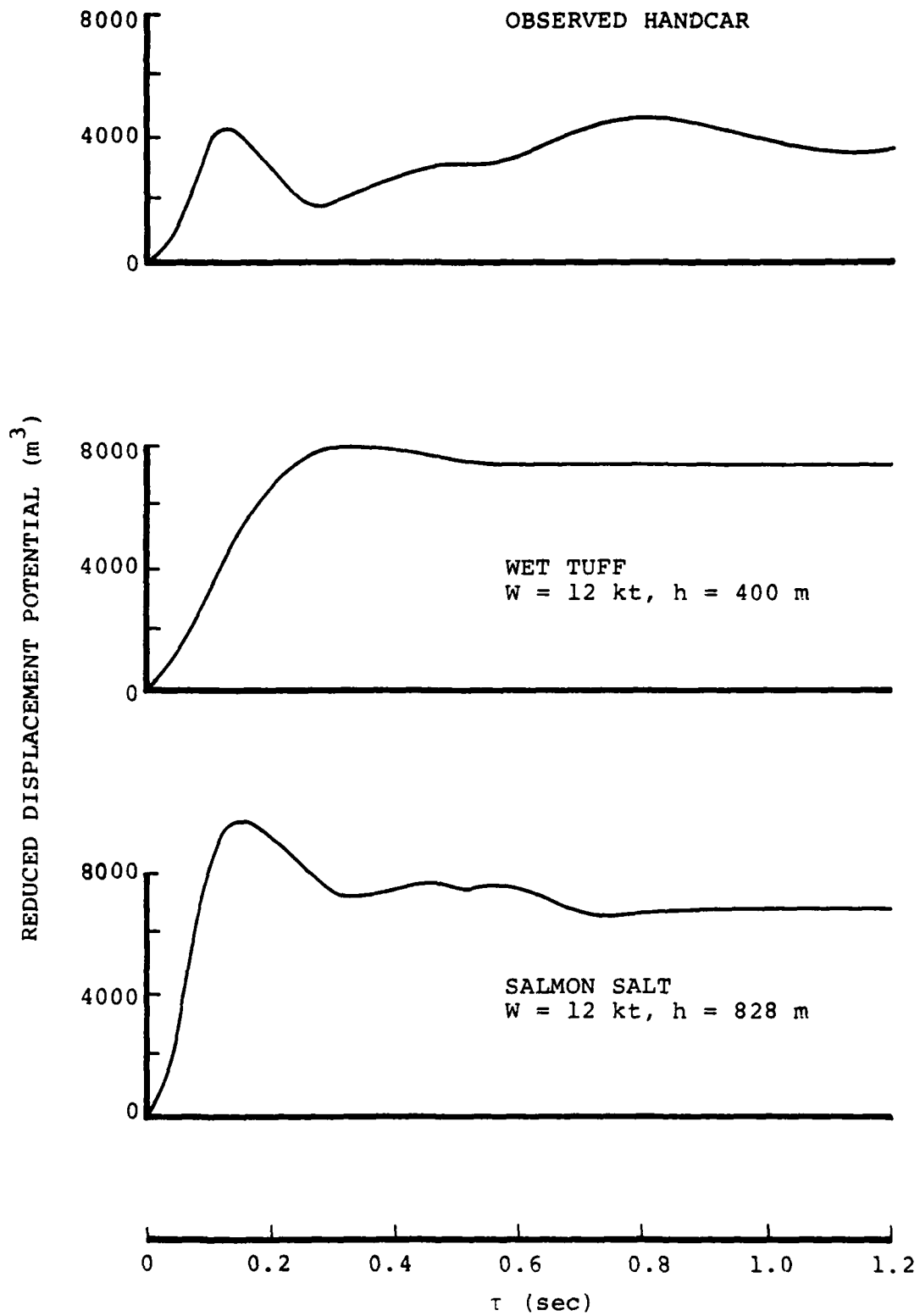
Figure 3.5. Comparison of the Handcar Reduced Displacement
           Potential With the Reduced Displacement Poten-
           tials for Events of Equivalent Yield in Wet
           Tuff and Salt.
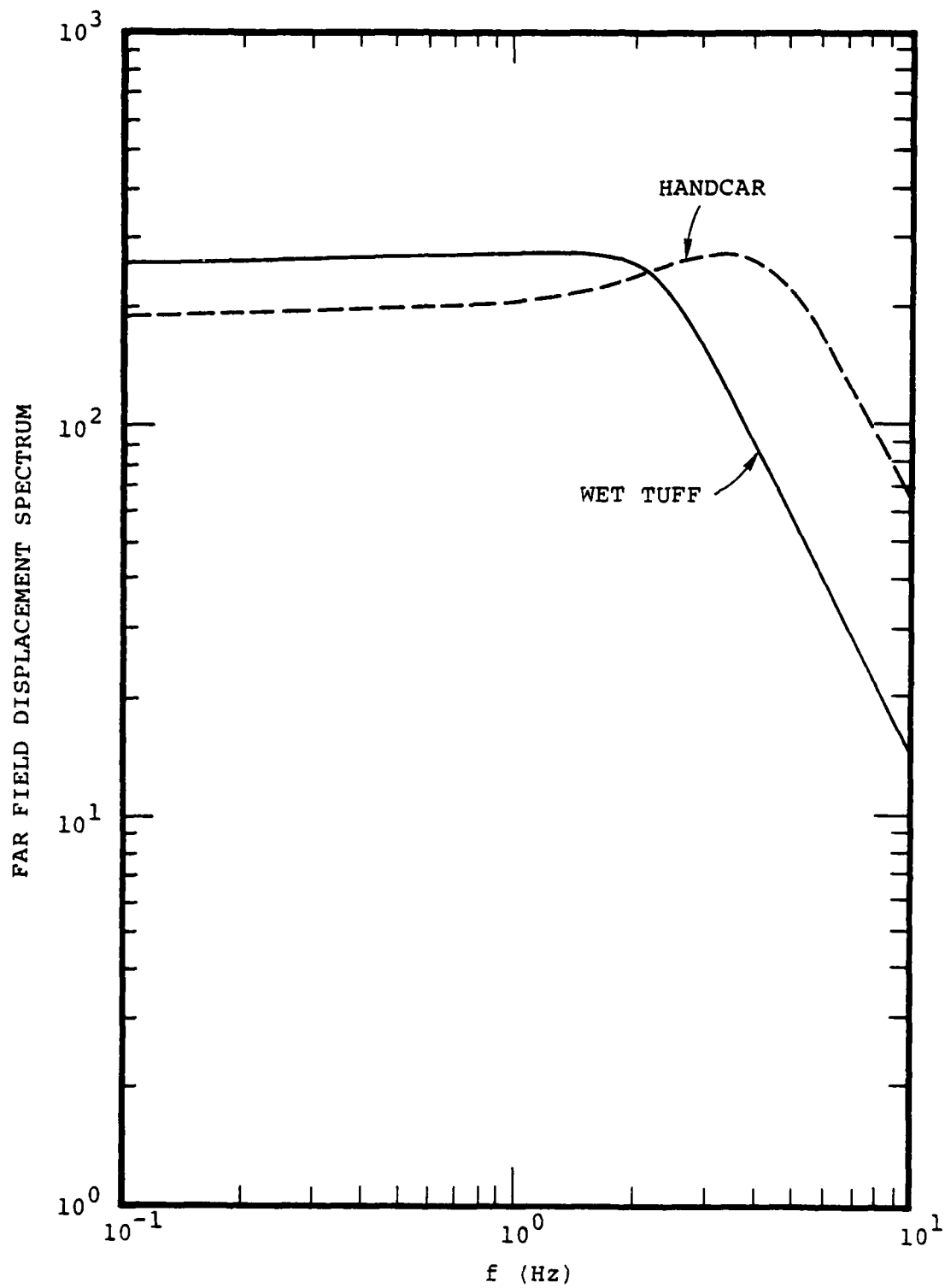
Figure 3.6. Comparison of the Handcar Relative Coupling
Function With the Relative Coupling Function
for an Event of Equivalent Yield in Wet Tuff.

102

event. Additional research is needed to define the effects of permanent gases on cavity growth and, ultimately, on seismic coupling.

3.3   Discus Thrower

The Discus Thrower event is of special interest because it was detonated very close (i.e. within about one cavity radius) to the underlying tuff/Paleozoic boundary. Such events have always posed a problem from a coupling point of view in that it is not clear whether the teleseismic P wave should be expected to be similar to those from comparable events in either tuff or Paleozoic rock source media. The Discus Thrower data are well suited to addressing this question inasmuch as ground motions were measured at several different ranges both above and below the tuff/Paleozoic boundary. It has already been noted in Chapter II above that the RDP functions derived from some of the ground motion data recorded below this interface are quite different from those derived from data recorded at the same range in the overlying tuff. The objective of the present investigation is to determine to what extent these differences can be explained by linear reflection and refraction processes and, ultimately, to try to assess the significance of any nonlinear interaction at the tuff/Paleozoic boundary on the character of the P wave signal radiated to teleseismic distances.

The RDP functions (resultant) derived from the ground motion data recorded in Borings 9 and 12 (cf. Chapter II) are reproduced in Figures 3.7 and 3.8 respectively. Considering first the Boring 9 data of Figure 3.7 which were recorded at a horizontal range of 488 m, it can be seen that the RDP functions derived from the data recorded at the tuff stations 9A and 9B are quite consistent and have the general character expected for a free-field measurement in the elastic regime. The RDP functions
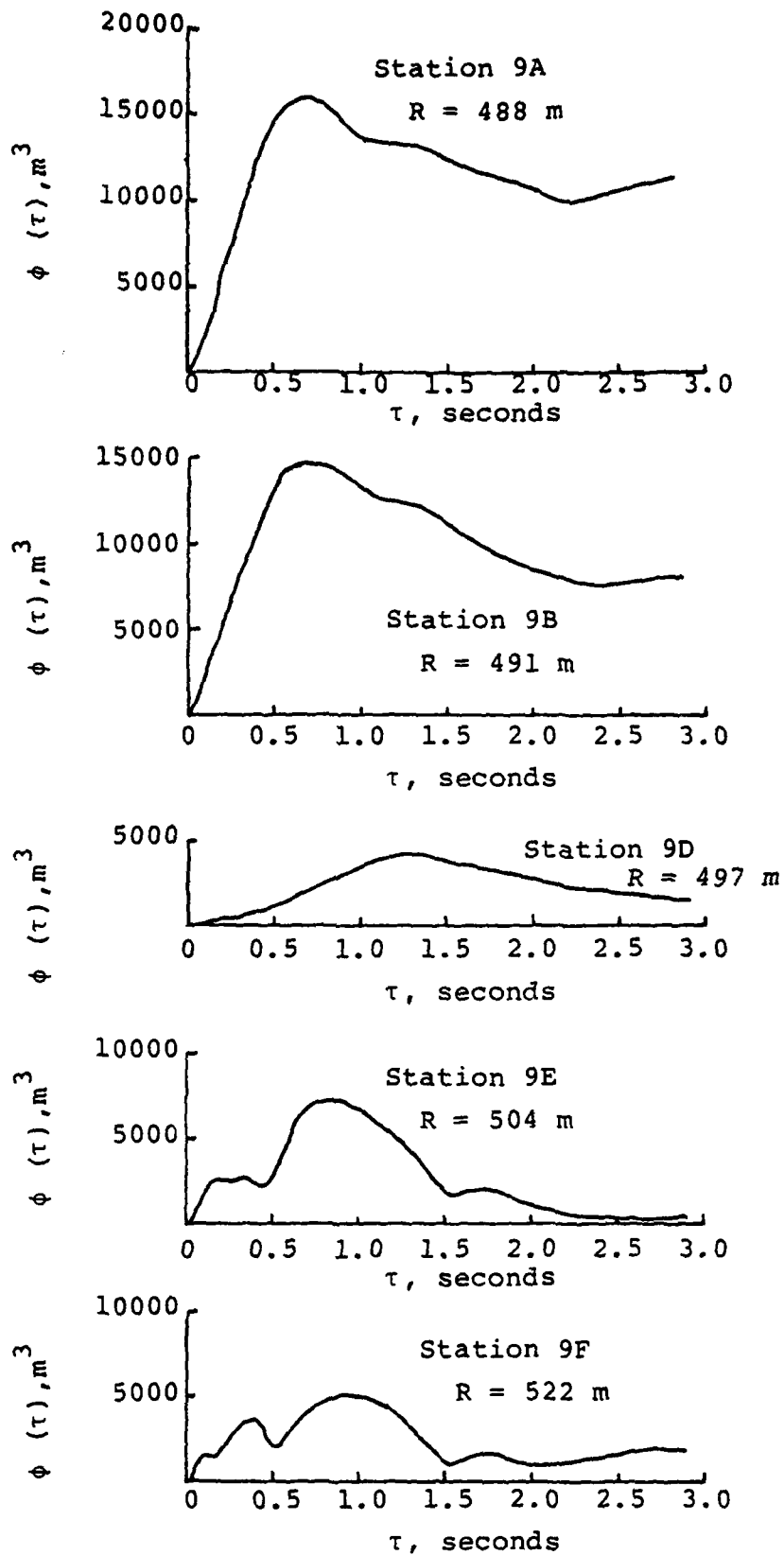
Figure 3.7   Observed Discus Thrower Reduced Displacement
Potentials Stations 9A, 9B, 9D, 9E and 9F.

104
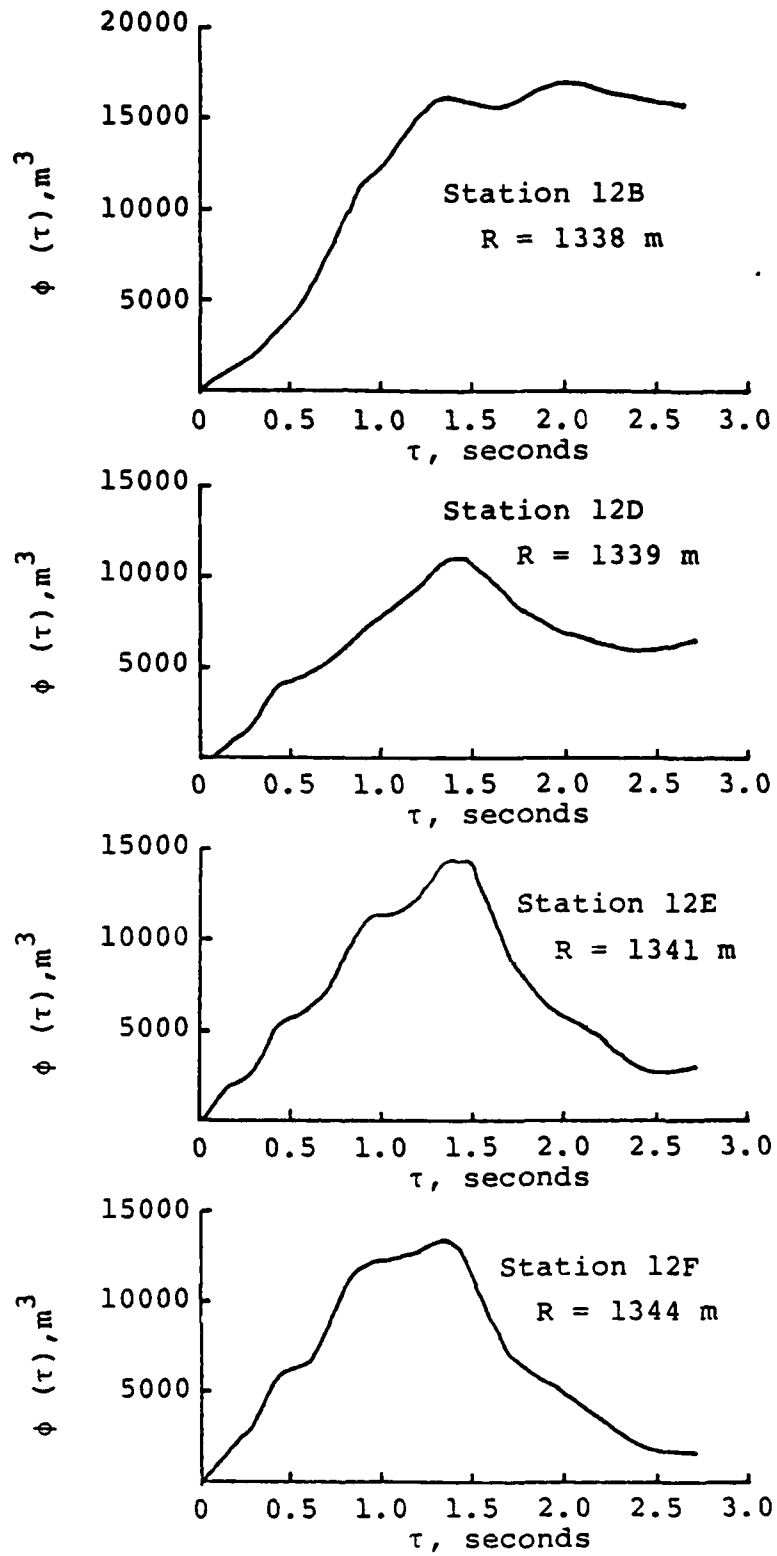
Figure 3.8   Observed Discus Thrower Reduced Displacement
              Potentials Stations 12B, 12D, 12E and 12F.

derived from the dolomite stations 9D, 9E and 9F, on the other
hand, are much more complex and of significantly lower ampli-
tude, indicating that the ground motion observed below the tuff/
Paleozoic interface has been significantly modified by either
linear or nonlinear interaction between the primary outgoing
wave and this boundary. The Boring 12 data of Figure 3.8, on
the other hand, which were recorded at a horizontal range of
1341 m are fairly consistent, showing about the same amplitude
level and general shape (out to times on the order of two seconds)
independent of whether the receiver is located in tuff (12B and
12D) or Paleozoic rock (12E and 12F). Moreover, the maximum
value of the RDP functions from the Boring 12 stations are re-
markably consistent with those observed at stations 9A and 9B,
suggesting that these latter two RDP functions are representative
of propagation in the linear, elastic regime. Consequently, we
have proceeded by assuming that Discus Thrower can be modeled as
a point source with a source time function consistent with the
RDP functions observed at 9A and 9B and then used this source
to attempt to model the Paleozoic observations assuming linear,
elastic interaction at the tuff/Paleozoic boundary. Thus, in
this approach, discrepancies between calculated and observed
ground motions are interpreted as possible indications of non-
linear response. In order to facilitate these calculations,
the observed RDP has been approximated using an analytic repre-
sentation of the form (Haskell, 1967)

$$\phi(\tau) = \phi(\infty) - \phi(\infty) \ e^{-k\tau} \left[1 + k\tau + \frac{k^2}{2} \tau^2 + \frac{k^3}{6} \tau^3 - Bk^4 \tau^4 \right]$$

Figure 3.9 shows a comparison of the average observed RDP for
stations 9A and 9B with the selected analytic approximation
(i.e. $B = 0.2$, $k = 9 \ sec^{-1}$, $\phi(\infty) = 10,000 \ m^3$).

Attempts to model the observations have focused on the
particle displacement data for Boring 9 which are shown in
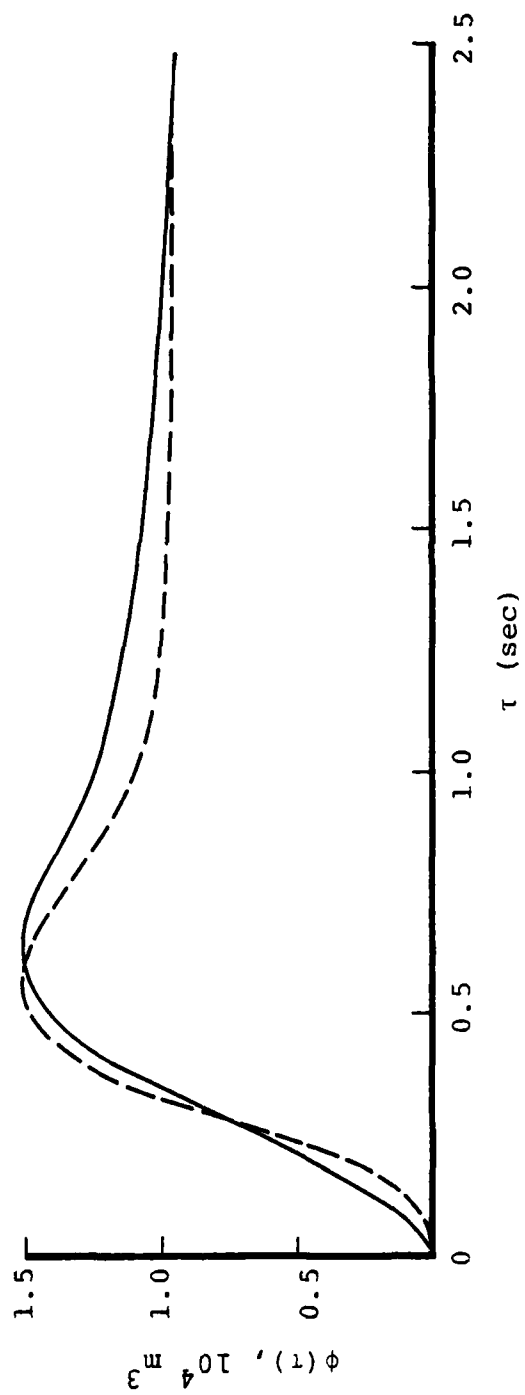
Figure 3.9. Comparison of the Observed Discus Thrower Reduced Displacement Potentials (Stations 9A and 9B) With the Haskell Analytic Approximation of the Reduced Displacement Potential.

107

Figure 3.10. As would be expected from the corresponding RDP functions of Figure 3.7, the motion at the tuff stations 9A and 9B is fairly simple and predominantly horizontal while at the Paleozoic stations the vertical component of motion is at least as large as the horizontal. The present attempt to model the motion at the Paleozoic stations will of necessity involve a number of rough approximations to the actual field conditions. In the first place, the idealized, plane-layered geologic section of Figure 2.35 will be used to represent the actual sub-surface geology at the site which more nearly corresponds to that shown in Figure 3.11. Given this complexity, including the presence of a fault in the immediate vicinity of the stations of interest, an elaborate modeling study is probably not warranted initially and we have proceeded by summing the contributions from a relatively few rays, the amplitudes of which have been computed using the simple plane wave reflection and transmission coefficients. Thus diffraction effects are not included nor are any near-field terms which may be pertinent at these close distances, especially for the lower frequency components of the motion.

Figure 3.12 shows the travel paths associated with the eight rays which should dominate the early-time response at the Paleozoic stations. The results of the simulation are summarized in Figure 3.13. The left-hand column in this figure shows the displacement components recorded at stations 9A, 9E and 9F, again contrasting the horizontal motion levels above and below the tuff/Paleozoic boundary. The right-hand column shows the results of two different ray summations designed to simulate the early time response at shallow depths in the Paleozoics (i.e. 9E and 9F are not distinguished here because of the complexity of the interface). The upper figure in this column corresponds to the addition of the eight rays of Figure 3.12 and gives a fair match to the observed amplitude level and wave shape. However, it can be seen that the predicted initial motion of the

108
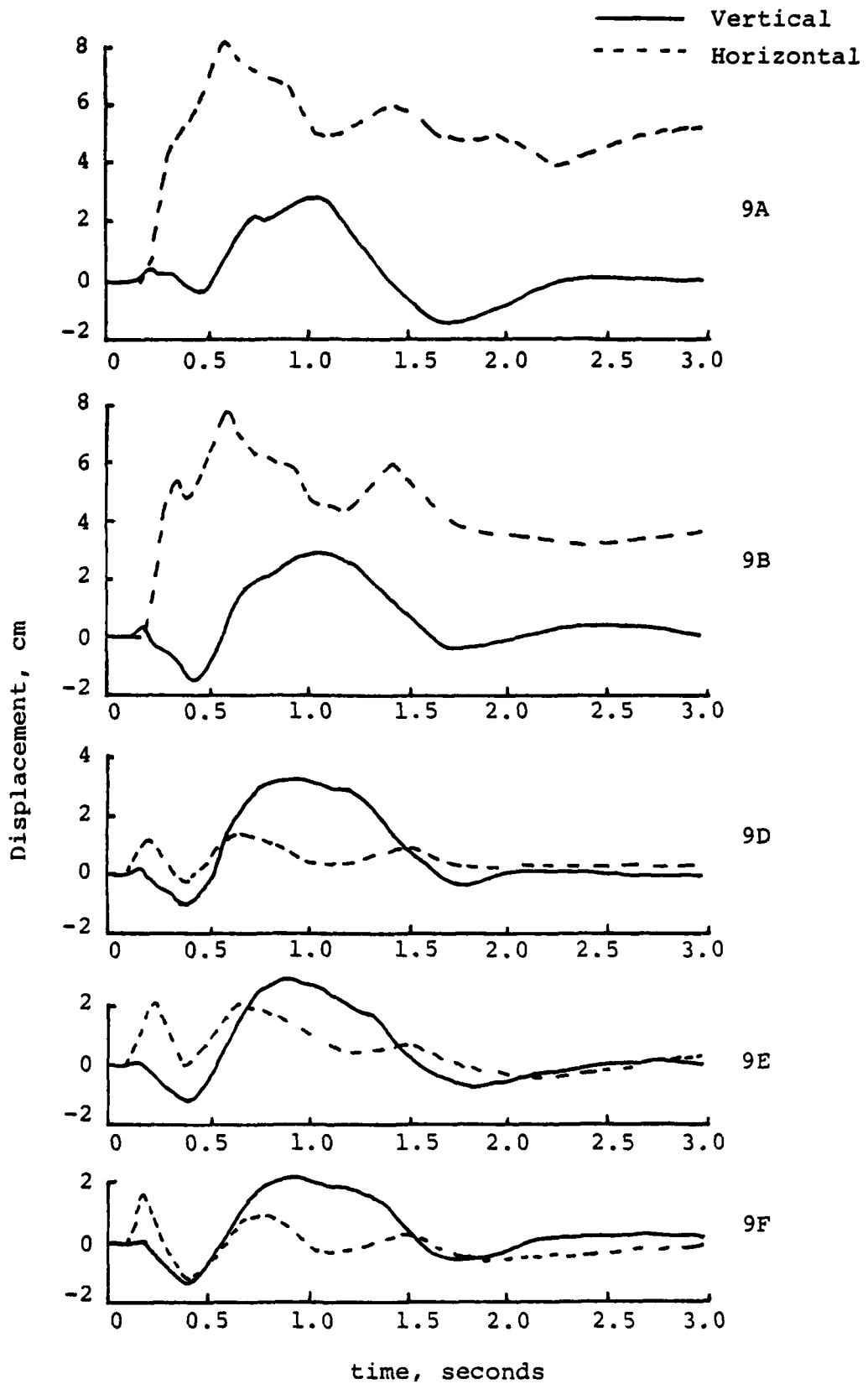
Figure 3.10   Observed Discus Thrower Displacement Time
               Histories for the Stations in Boring 9.

Ground Surface

Alluvium

Discus   Tuff
Thrower

• 9A

• 9B

9D

• 9E

• 9F

Dolomite

100 m

100 m
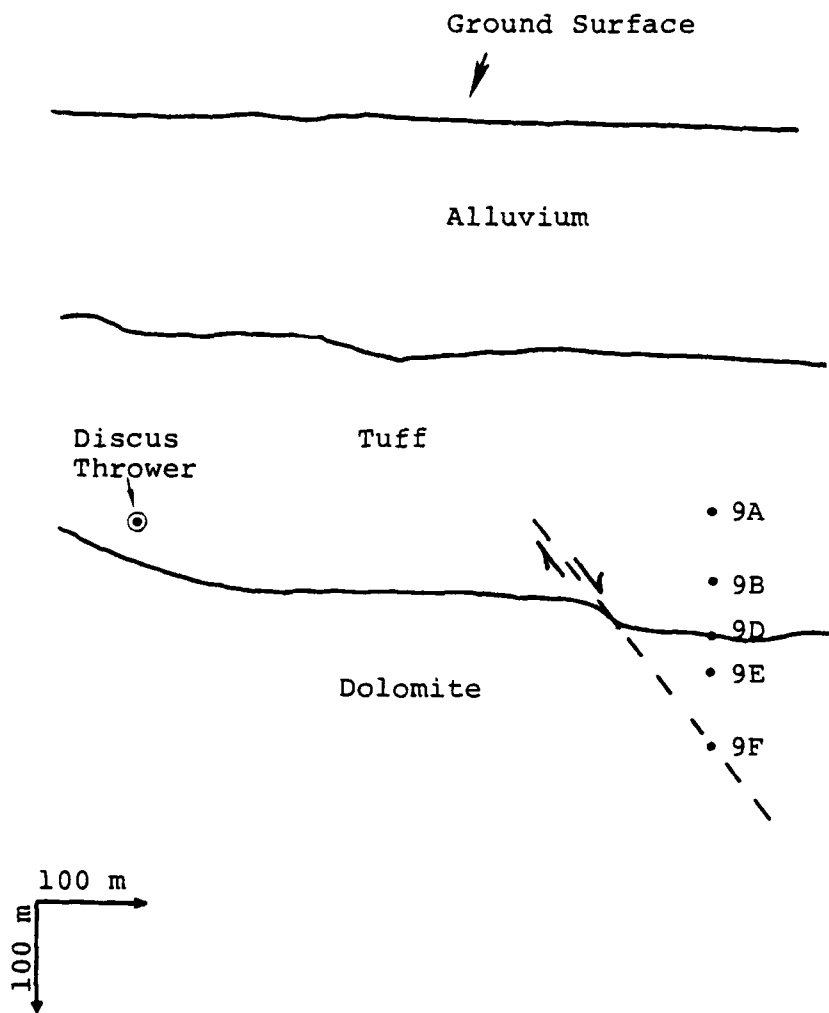
Figure 3.11   Vertical Section of the Discus Thrower Site
Showing the Locations of Stations in Boring
9 Relative to the Detonation Point and Cer-
tain Complexities in the Geologic Structure.

110
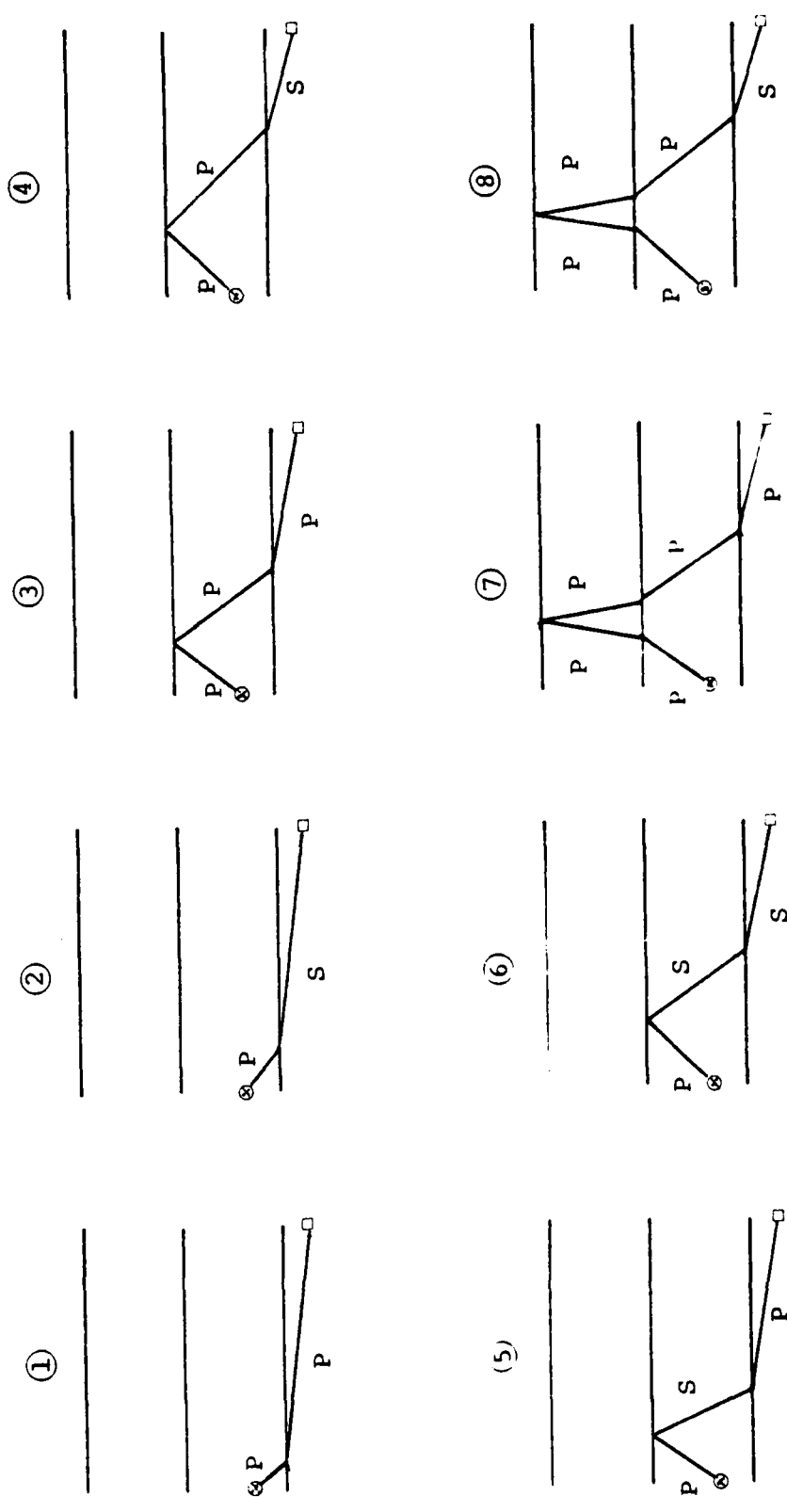
Figure 3.12 Schematic Diagram Showing Travel Paths for Eight Rays Which Should be Prominent at Early Times on the Discus Thrower Records from the Paleozoic Stations.

111
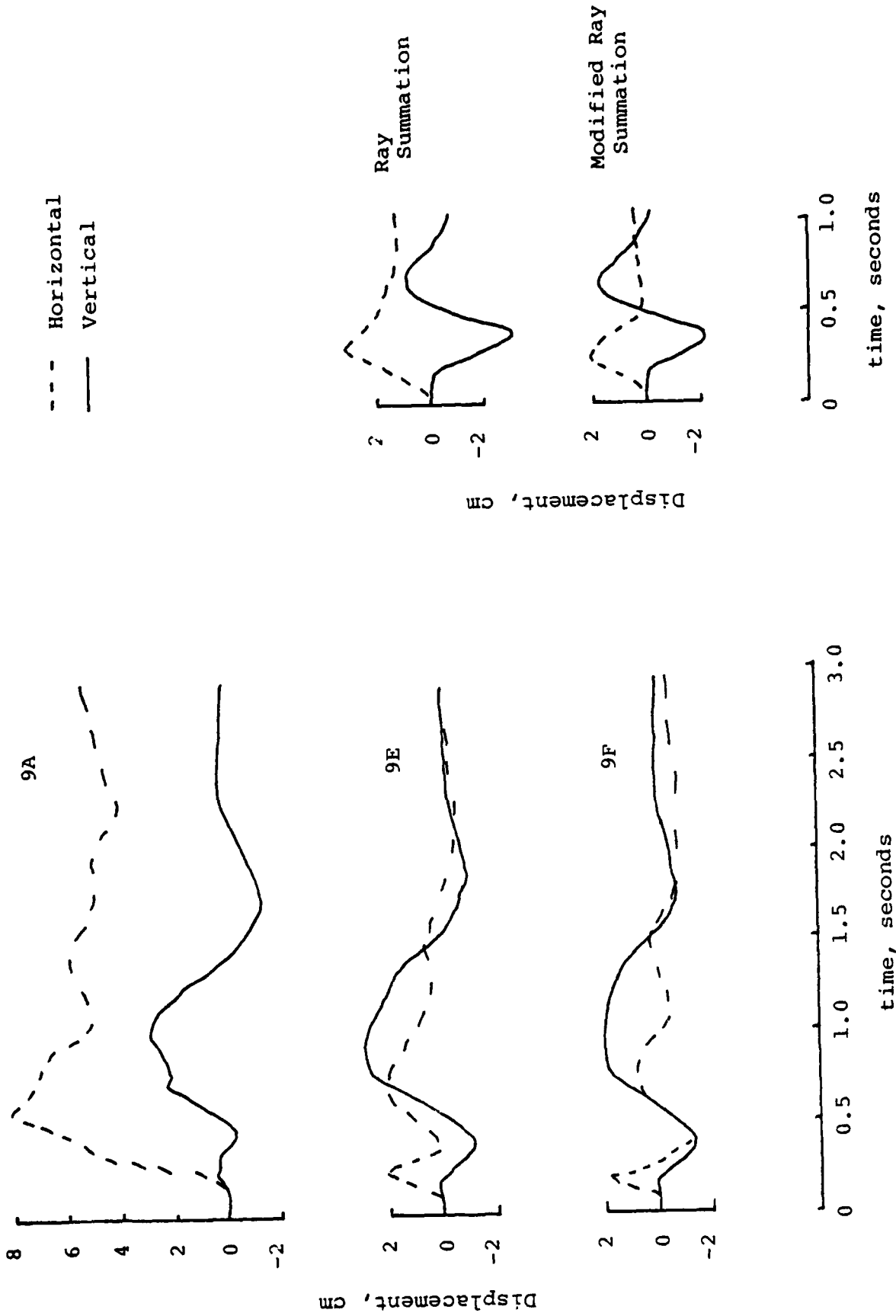
Figure 3.13 Comparison of the Discus Thrower Displacements Recorded Above and Below the Tuff/Paleozoic Interface (left column) with the Simulated Displacements De-rived by Summing Ray Contributions (right column).

vertical component is too large. This pulse is due primarily
to the P to S conversion at the interface (i.e. ray (2) in
Figure 3.12) which according to the plane layer model, should
arrive nearly horizontally at the stations of interest and
thus contribute predominantly to the vertical component of
motion. The lower simulation in this column shows the effect
of changing the angle of incidence of this one ray to 45 de-
grees. This has the effect of reducing the initial amplitude
on both the vertical and horizontal components of motion, bring-
ing them into somewhat better agreement with the observations.
The only serious discrepancy is that the period of the initial
pulse on the computed horizontal component of motion is clearly
too long. This may be an indication that diffracted arrivals
from the fault zone which have been neglected in the simplified
calculation are contributing significantly to the observed motion.
In any case, the agreement is good enough to conclude that the
differences in the motion above and below the tuff/Paleozoic
interface at this range can be largely explained by linear re-
flection and refraction effects at the boundaries. It should be
noted, however, that this does not necessarily imply that the
teleseismic P wave will be typical of an explosion in tuff, since
the take-off angle to teleseismic distances is quite a bit
steeper than the one analyzed in the above simulations. However,
the continuity in the motion measured above and below the inter-
face at Boring 12 suggests that departures from spherical sym-
metry cannot have been too great in this case.

An interesting side light to the modeling effort des-
cribed above has been the definitive identification of a low
frequency pP pulse on the records from several different shot
depth stations. Figure 3.14 shows a comparison of the observed
and theoretical pP particle velocity for the shot depth level
station at a range of 488 m. The observed motion here corresponds
to a projection of the observed horizontal and vertical components

113

Figure 3.14 Comparison of the Particle Velocity Time History Observed for Discus Thrower at Station 9D with the Theoretical pP Pulse Computed at Shot Depth at a Range of 488 m Using the Source Function of Figure 3.9.

114

of motion onto the expected pP ray path (i.e. take-off angle
of about 33°; Perret and Kimball, 1971). Positive motion here
corresponds to motion out along the raypath, and thus the
arrival indicated by the vertical arrow is a dilatation. The
lower trace in this figure shows the theoretical pP pulse com-
puted for this range using the source function of Figure 3.9
together with the plane wave reflection and transmission co-
efficients. It can be seen that the predicted arrival time,
dominant frequency content and absolute amplitude level agree
quite well with the observation, confirming that the identified
arrival is pP. Similar comparisons for the shot depth station
at a range of 1341 m are shown in Figure 3.15. Here again the
predicted and observed dominant frequency content and amplitude
level agree quite well, although the predicted arrival time is
somewhat early in this case. This is probably due to lateral
variations in the subsurface structure which is being modeled
using a plane layered approximation. Figure 3.16 shows that
the pP travel paths to the two shot depth stations sample sub-
stantially different portions of the near surface geology. In
any case, the evidence strongly indicates the existence of a
classical pP pulse at these two locations. However, as is
demonstrated in Figure 3.16, these observations can not be used
to conclusively infer the existence of a classical pP arrival
in the teleseismic P waveforms, due to differences in the take-
off angle at the free surface. In fact, the reflection point
for teleseismic pP in this case lies within the spalled region.
It is interesting to note that the spall radius for Discus
Thrower was anomalously small (Perret and Kimball, 1971) and
this may explain the apparently unique clear observation of
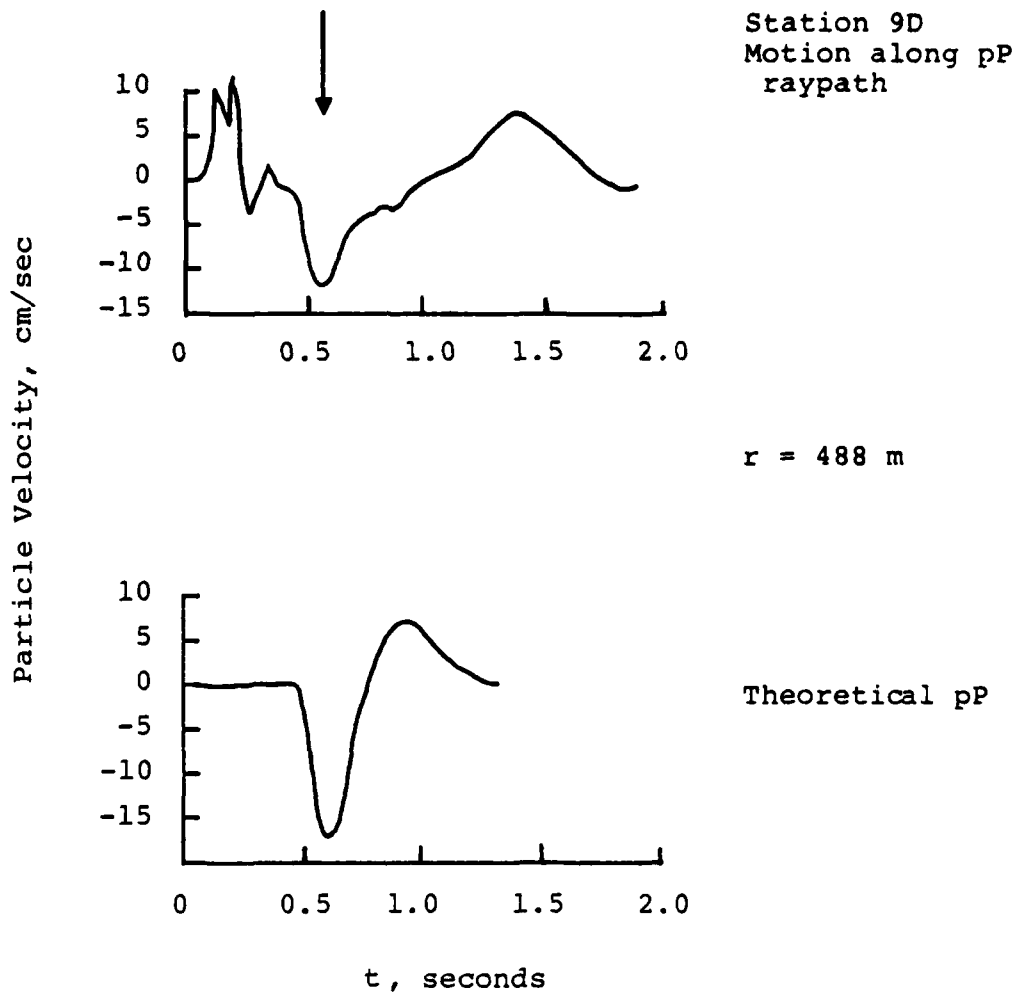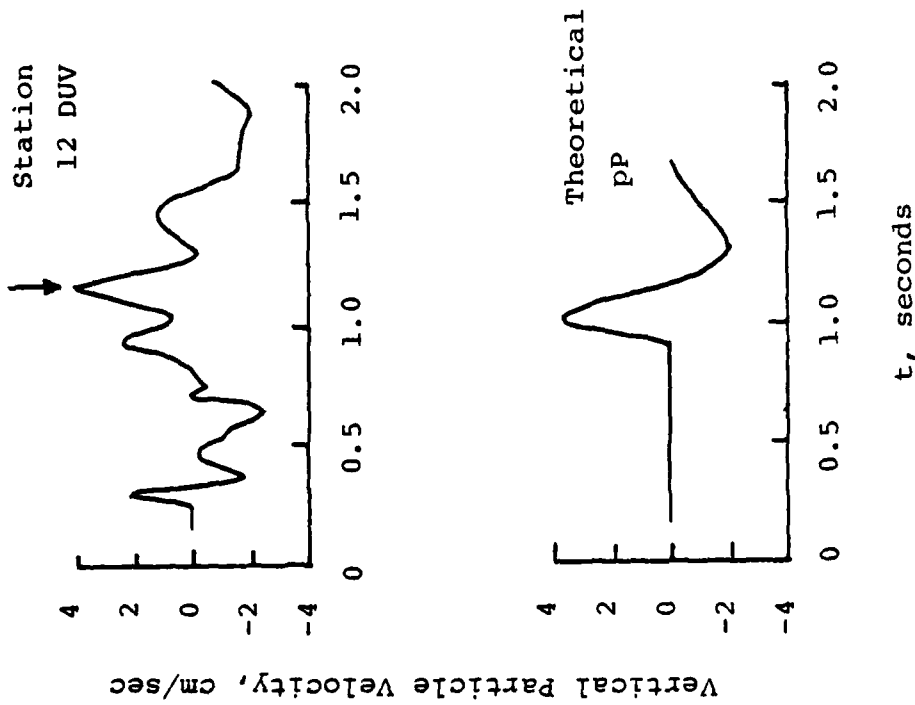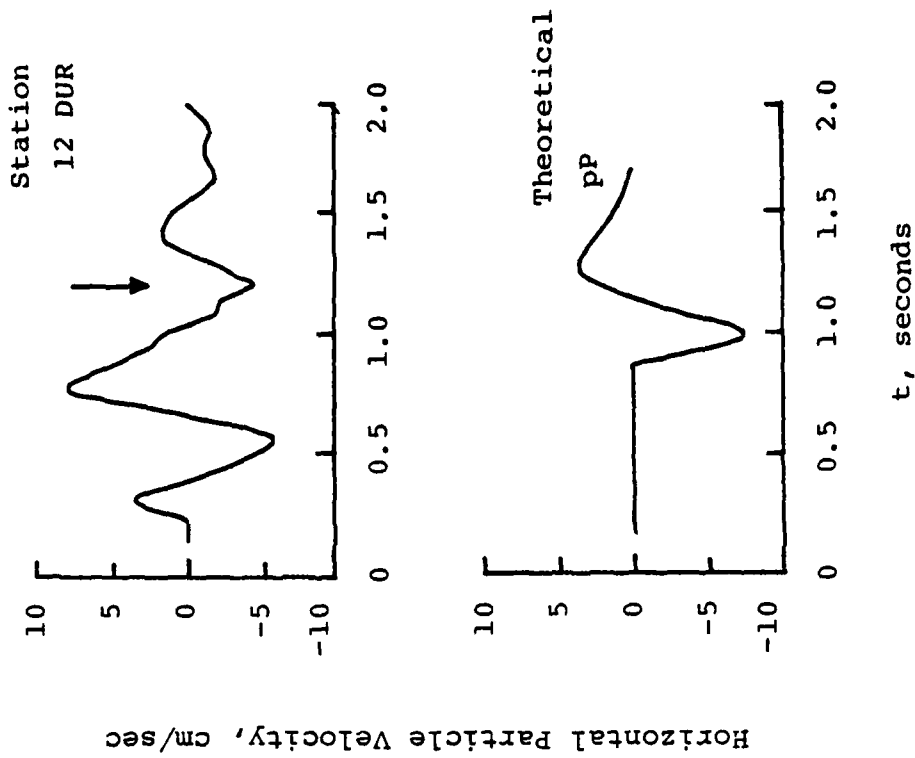pP on the shot depth stations used to monitor this event.

Figure 3.15 Comparison of the Particle Velocity Time Histories Observed for Discus Thrower at Station 12 with the Theoretical pP Pulse Computed at Shot Depth at a Range of 1341 m Using the Source Function of Figure 3.9.
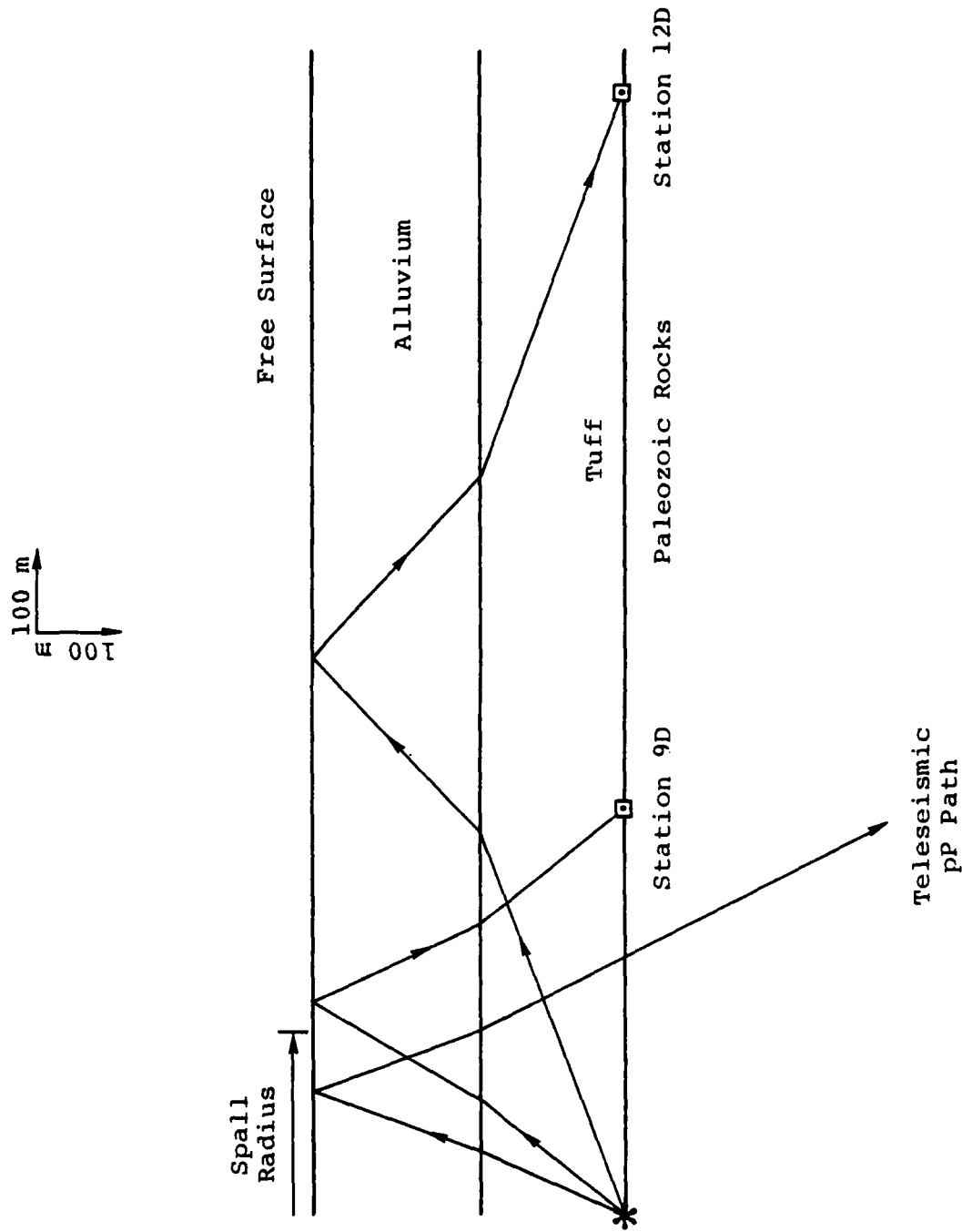
Figure 3.16   Comparison of Ray Paths for the pP Phase in the Near-Surface Geologic Structure at the Discus Thrower Site.

117

3.4   Merlin

Shot level stations for the Merlin event recorded an unusual low-frequency signal at late time which increases in prominence relative to the direct signal at large distances from the source. Because this signal could affect the radiated seismic field, we have attempted to identify its cause. Figures 3.17 through 3.20 show the ground motion records at shot depth for the Merlin event; the stations (cf. Figure 2.14) were equipped with only radial component instruments as noted above. Several prominent phases appear on the records; the late time, low-frequency phase which is of interest in the current study is identified by dashed lines. Notice that because of its low frequency character, the signal is barely evident on the acceleration traces, but becomes increasingly important with each successive integration. The most diagnostic characteristics of this pulse appear to be: (a) late arrival time ($\sim$ 1.5 seconds), (b) relatively low frequency ($\sim$ 1 Hz), (c) moderate horizontal phase velocity ($\sim$ 1,800 m/sec), and (d) nearly constant amplitude over the range of observation (note that amplitude scales for Figures 3.17 through 3.20 change with range). We have considered three possible sources of this arrival: (1) free surface reflected phases (i.e. pP or pS), (2) reflections from a deep interface and (3) signals generated by spall closure. Figure 3.21 shows a comparison of the observed arrival times with hypothetical arrival times of pP and pS. The estimate of pP arrival time is straightforward and involves merely doubling the P wave arrival time observed near the appropriate surface reflection point. Thus, it is clear that this secondary arrival is not pP. The pS arrival time on this figure, on the other hand, are more speculative in that they were computed using the average observed uphole P wave velocity together with an assumed Poisson's ratio of 1/4. In fact, if Poisson's ratio is taken to be 0.47, then the observed arrival time can be fit fairly well by pS. However, there are other problems with this interpretation.

118

Figure 3.17 Ground Motion Time Histories for the Merlin Event
Recorded at Station U4, R = 213 m; Positive Re-
presents Outward Radial Motion.

119

Figure 3.18 Ground Motion Time Histories for the Merlin Event Recorded at Station U5, R = 335 m; Positive Represents Outward Radial Motion.

120

Figure 3.19   Ground Motion Time Histories for the Merlin Event
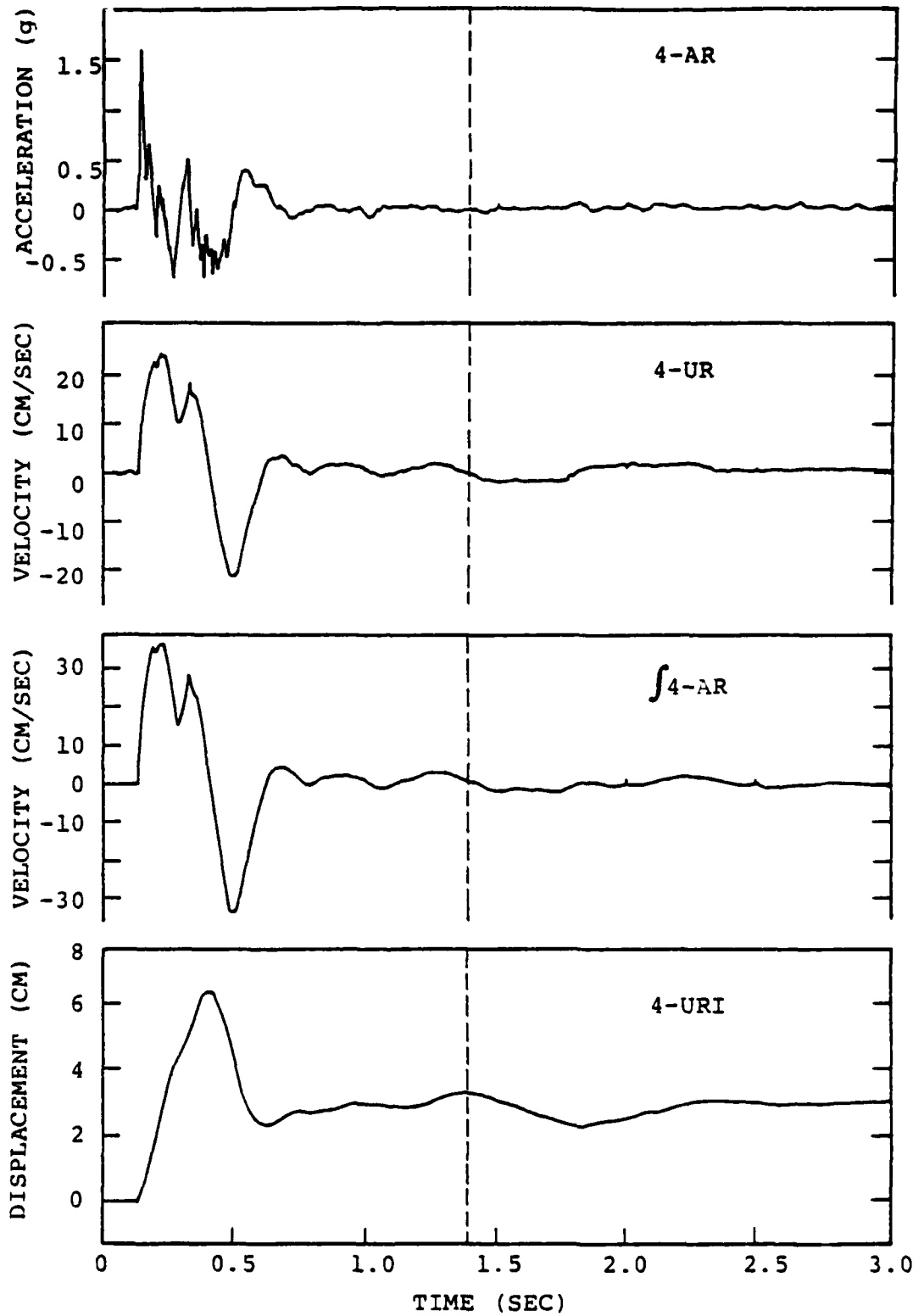Recorded at Station U6, R = 488 m; Positive Re-
presents Outward Radial Motion.

121

Figure 3.20   Ground Motion Time Histories for the Merlin Event
Recorded at Station U7, R = 762 m; Positive Re-
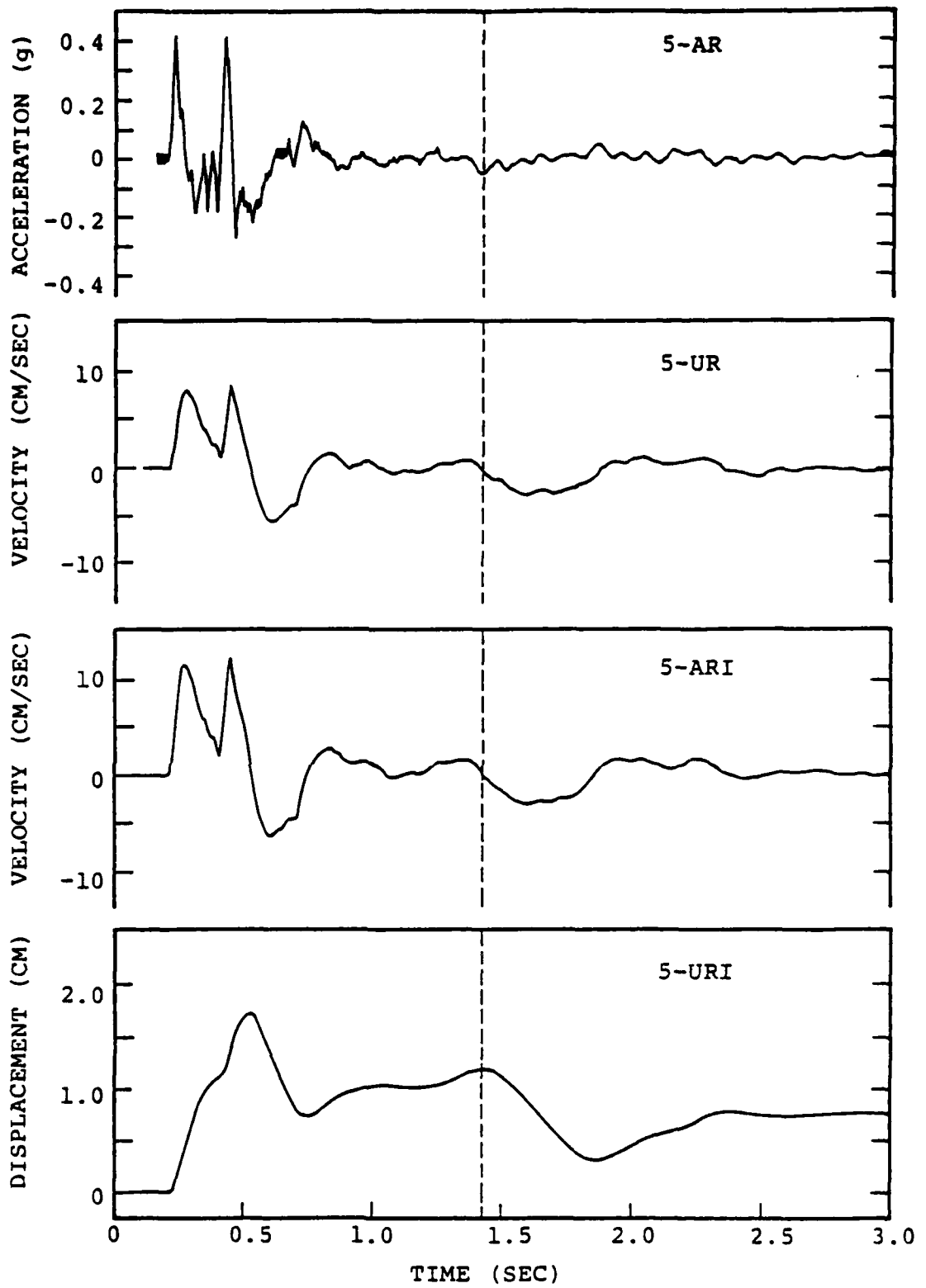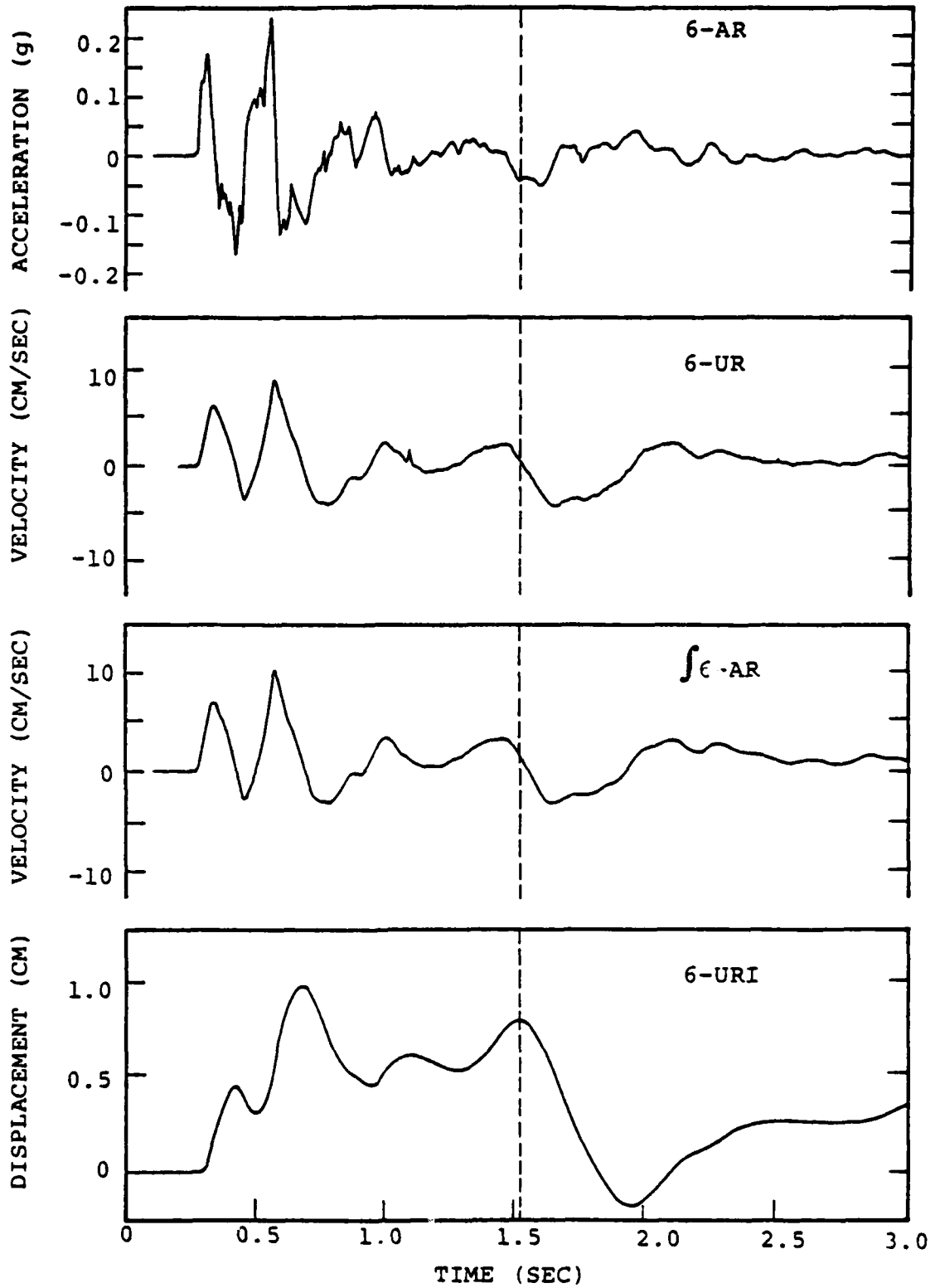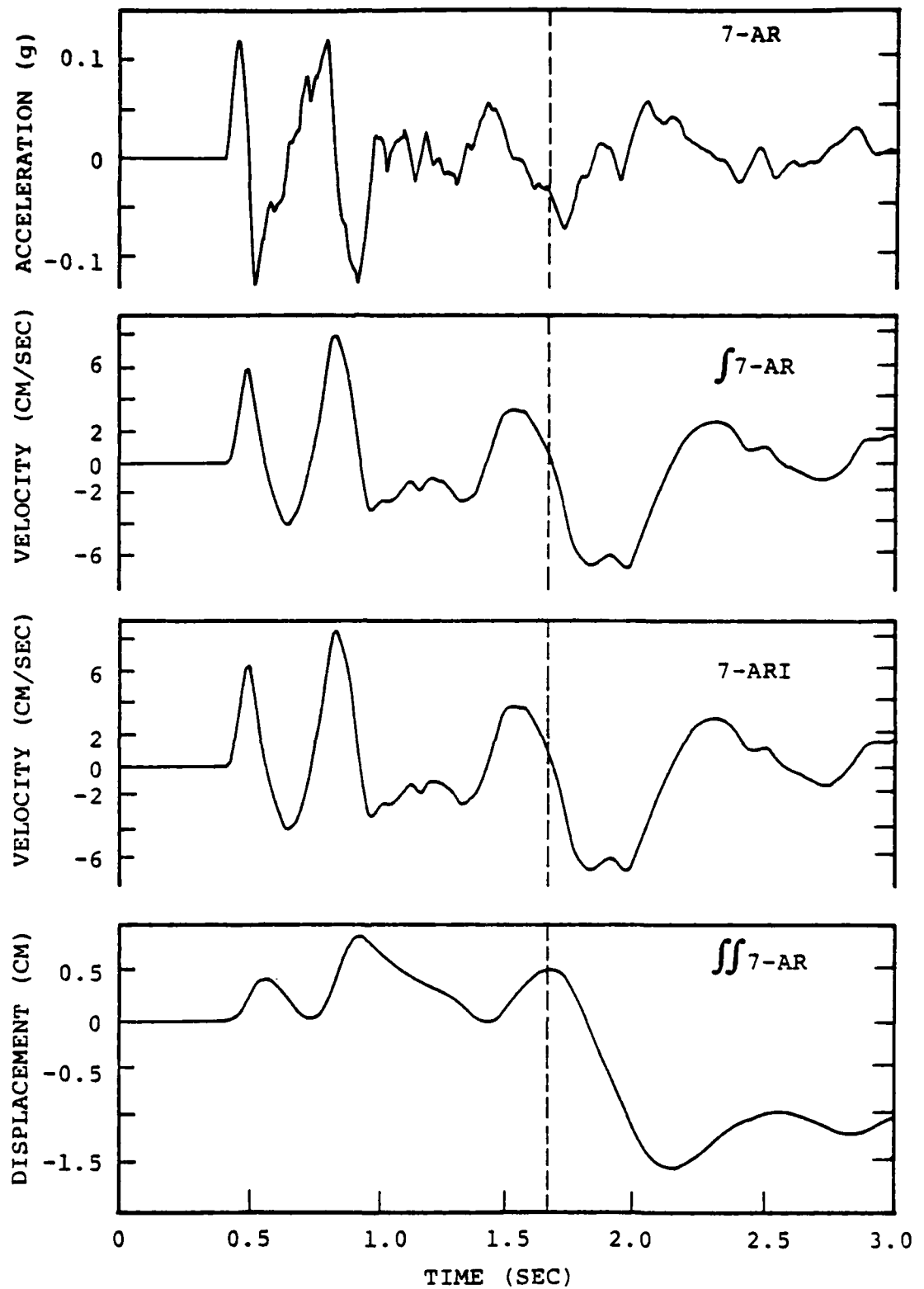presents Outward Radial Motion.

122
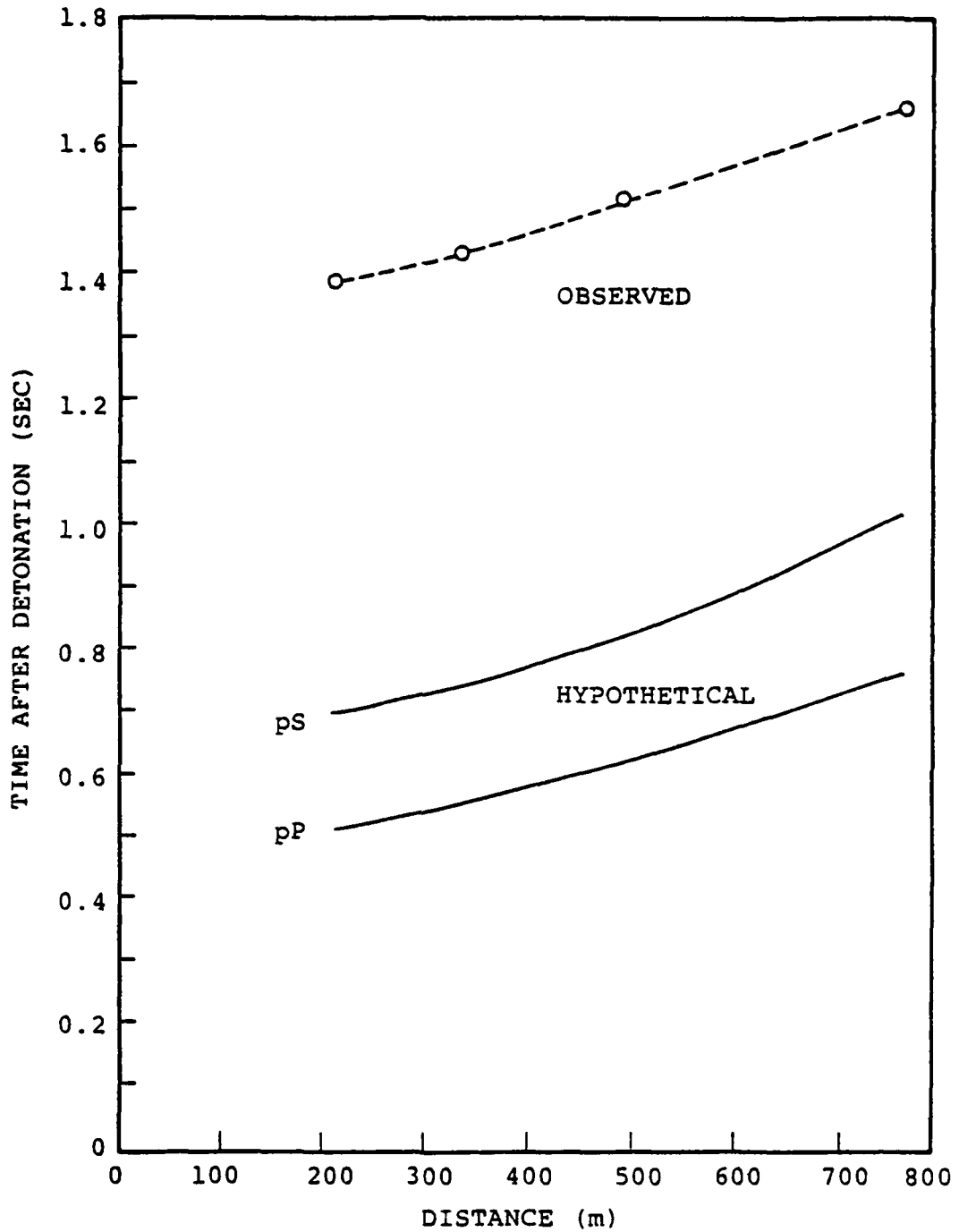
Figure 3.21   Comparison of Arrival Times of Low-Frequency,
Late-Time Phase from Merlin with Hypothetical
Arrival Times of pP and pS Phases.

First, a Poisson's ratio of 0.47 together with the observed uphole P wave velocity ($\sim$ 1,250 m/sec) gives an average S wave velocity between the surface and a depth of 300 m of only about 275 m/sec. This is at least a factor of three lower than the values commonly quoted for Yucca Flat alluvium. Moreover, the amplitude expected for pS at these stations are not consistent with the observations. That is, while the observed pulse amplitudes are essentially constant over this distance range, the pS amplitude would be expected to decrease by more than a factor of two considering changes in the reflection coefficient and geometrical factors. Even more decisive is the fact that for the assumed high value of Poisson's ratio required to fit the arrival times, the expected amplitude of pS at say the 335 m station would be expected to be only about 1/20 that of the direct arrival, when, in fact, they are observed to be of nearly comparable amplitude. Thus, although the evidence is less definitive than it is for pP, we conclude that the arrival in question *is not pS.*

We have also considered the possibility that the observed phase represents a reflection from a deep interface. However, in order to explain the late arrival time, the interface would have to be located about 1 km below the shot and the apparent velocity across the shot depth stations from a reflection at this depth would be expected to be much greater than the observed apparent velocity of about 1,800 m/sec. Moreover, because of losses along the relatively long ray path, the amplitude of a reflection from this depth would be expected to be much smaller than the observed amplitudes which are comparable to that of the directly induced motion at the three more distant stations.

Having eliminated surface reflections and deep reflections as explanations of the observation, we are left with the spall closure source mechanism. Figure 3.22 shows the vertical acceleration time histories recorded on the surface at distances from

124

Figure 3.22   Free Surface Acceleration Time Histories for the
Merlin Event. The Dashed Line Indicates the
Assumed Time of Spall Closure.

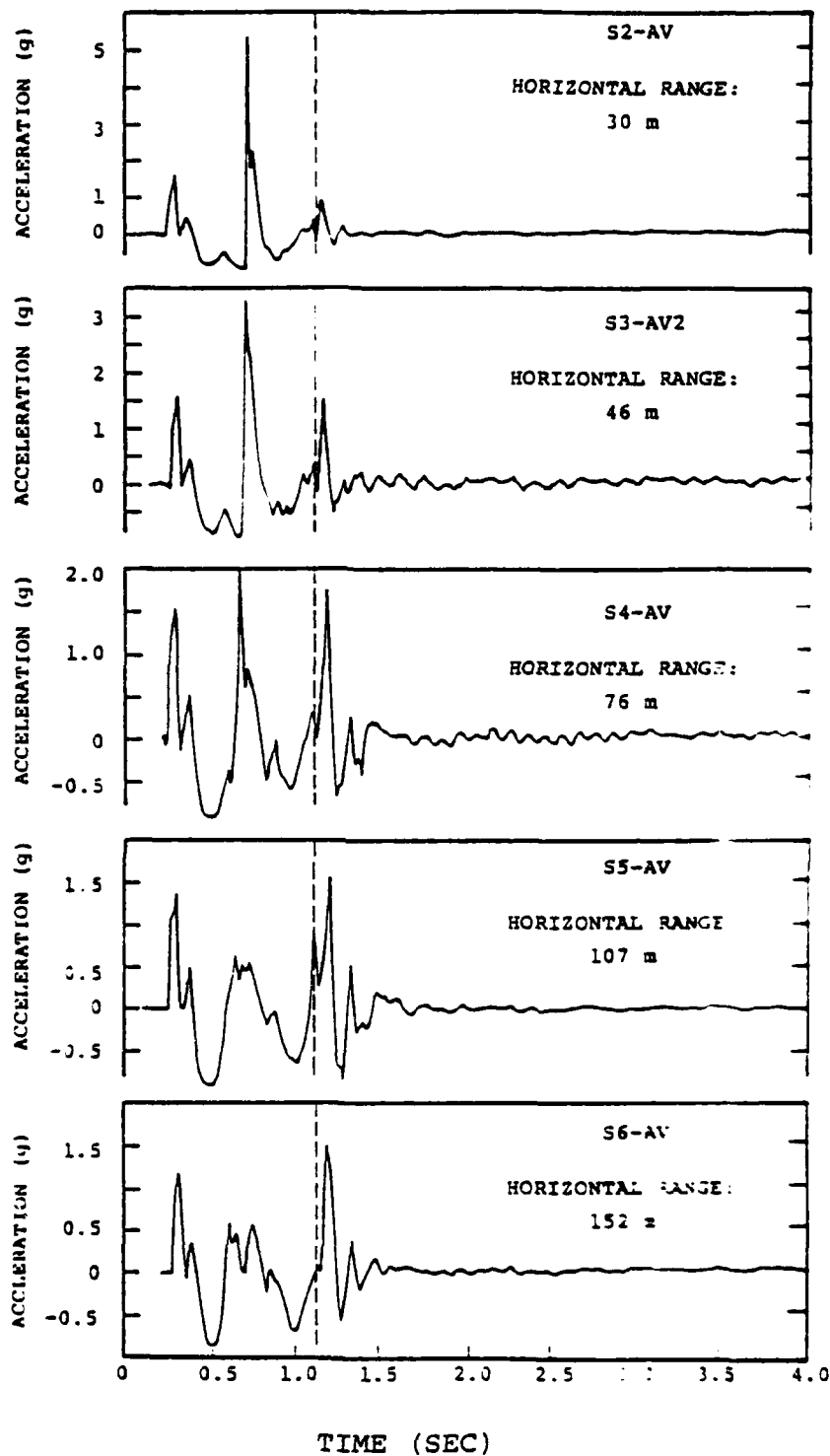30 to 152 meters from ground zero. It can be seen that these records are complex, showing evidence of multiple spall events. In general, there seem to be two prominent rejoin or stopping phases, the later of which becomes more prominent with increasing range. We interpret this phase as the time of closure at the deepest depth of significant spall and have read the closure times indicated by the dashed vertical lines on these figures. These closure times are fairly constant over this distance range and average about 1.15 seconds. A simple calculation indicates that a P wave originating at this time from the spall region would be expected to arrive at the shot level stations at times very close to the observed arrival times of the phase under investigation. This observation has prompted a more detailed analysis of the near field displacements generated by spall closure.

A series of simple elastodynamic calculations were undertaken to simulate the near field spall closure waveform.[*] The explicit finite element code SWIS (Frazier and Petersen, 1974) was employed for these calculations. Spall closure was modeled by assigning to a cylindrical region of radius r_0 and depth h_0 an initial vertical velocity V, given as a function of radial distance r by

$$V = \left[V_0 + V_1 \left(1 - \frac{r}{r_0} \right) \right] H \ (r_0 - r).$$

where V_0 and V_1 are constants and H $(r_0 - r)$ is a step function. Thus, V is a constant plus a linearly varying function of radial distance, going to zero at $r = r_0$. With V_0 set to zero, this corresponds to the conical profile suggested by Eisler and Chilton (1964). This spall plate is embedded at the surface of a geologic structure appropriate to Yucca Flat: a layer of alluvium overlying a halfspace of tuff. The layer thickness,

---

[*]The finite element analysis described in the following paragraphs was performed by Steven M. Day of S[3].

126

as well as the P wave velocities assigned these two materials were based on an analysis by Perret (1971) of travel times observed for the Merlin event. These are given in Table 3.1, along with the densities and Poisson's ratios which were assumed. Only elastic behavior was permitted.

The first four rows of Table 3.2 summarize four models of spall for which computations were performed; for comparison, the fifth row describes the spallation parameters which would be inferred for a 10 kt event from the empirical relations suggested by Viecelli (1973). Figure 3.23 is a schematic of the four computational models. Model I consists of a spall plate of 150 m radius, impacting at uniform velocity; Model II is the same as Model I, but with the impact velocity decreasing linearly to zero at 150 m radius; Model III consists of a spall plate of 300 m radius, impacting at uniform velocity, Model IV is the same as Model III, but with a linearly decaying impact velocity. In all four calculations, the spall thickness has been fixed at 60 m. In addition, a fifth calculation was performed to test the sensitivity of the computed waveforms to details of the geologic structure. In this case Model I spall parameters were used, but the thickness of the alluvium layer was increased from 330 m to 390 m. However, this change in geologic structure had little effect on the computed waveforms.

The quantities V_0 and V_1 in Table 3.2 were obtained by scaling the computed waveforms so as to match the peak-to-peak displacement amplitude observed for the late arriving pulse on the radial component at shot depth at 335 m range (Figure 3.18). We can see from column seven that the total impulse required to match the observed amplitude is a factor of 2 to a factor of 4 less for these models than the impulse inferred from Viecelli's empirical curves for a 10 kt event.

Figures 3.24 through 3.27 show the computed radial displacements at shot level for the four models. In each case, the pulse shapes resemble those of the observed phases to the

TABLE 3.1

ELASTIC PARAMETERS FOR SPALL CLOSURE CALCULATIONS

Rock Type	Thickness (m)	P Wave Speed (m/sec)	S Wave Speed (m/sec)	Density (kg/m³)	Poisson's Ratio
Alluvium	330	1,533	766	1,800	0.33
Tuff	∞	2,110	1,055	2,100	0.33

128

TABLE 3.2

DESCRIPTION OF MODEL PARAMETERS FOR SPALL CLOSURE CALCULATIONS

Model	Spall Radius (m)	Spall Thickness (m)	V_0 (m/sec)	V_1 (m/sec)	Maximum Height of Spall (m)	Total Impulse (Nt–sec)
Model I	150	60	1.28	0.0	0.084	0.98×10^{10}
Model II	150	60	0.0	3.07	0.48	0.78×10^{10}
Model III	300	60	0.54	0.0	0.015	1.65×10^{10}
Model IV	300	60	0.0	1.28	0.084	1.30×10^{10}
Viecelli (1973)	230	50	0.0	5.6	1.6	2.79×10^{10}
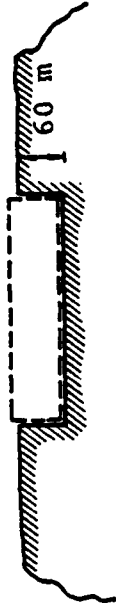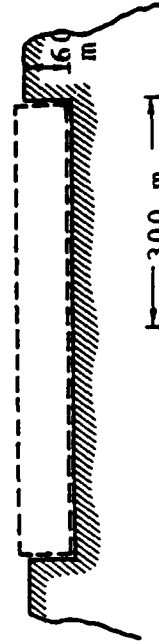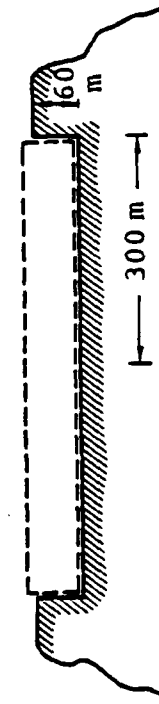
Figure 3.23   Schematic Diagram Showing the Four Computational Models Used to Represent Spall Closure.
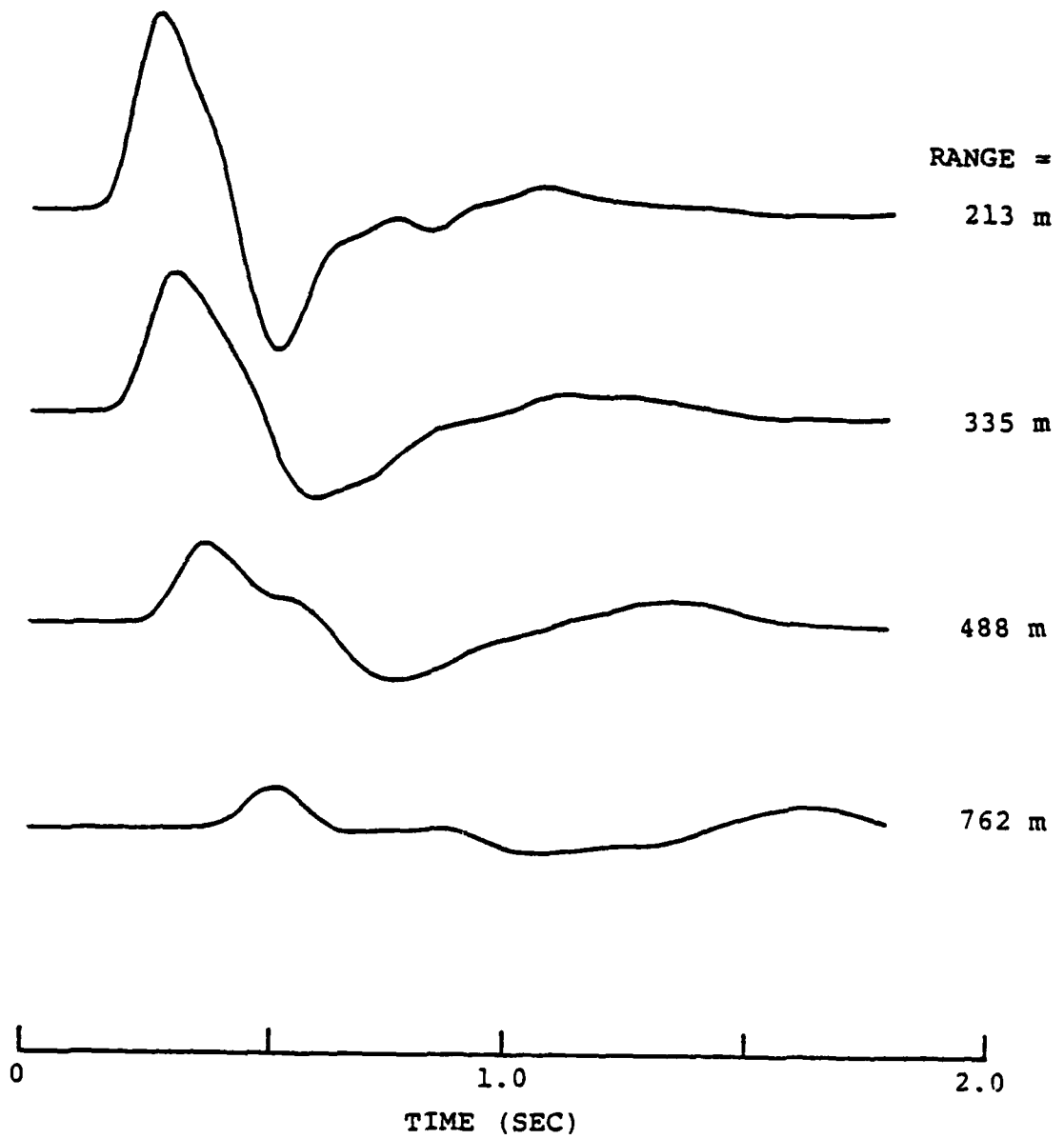
Figure 3.24 Computed Radial Displacements at Shot Level
Generated by Spall Closure Model I. Spall
Closure is Assumed to Occur at Time Equal 0.

131
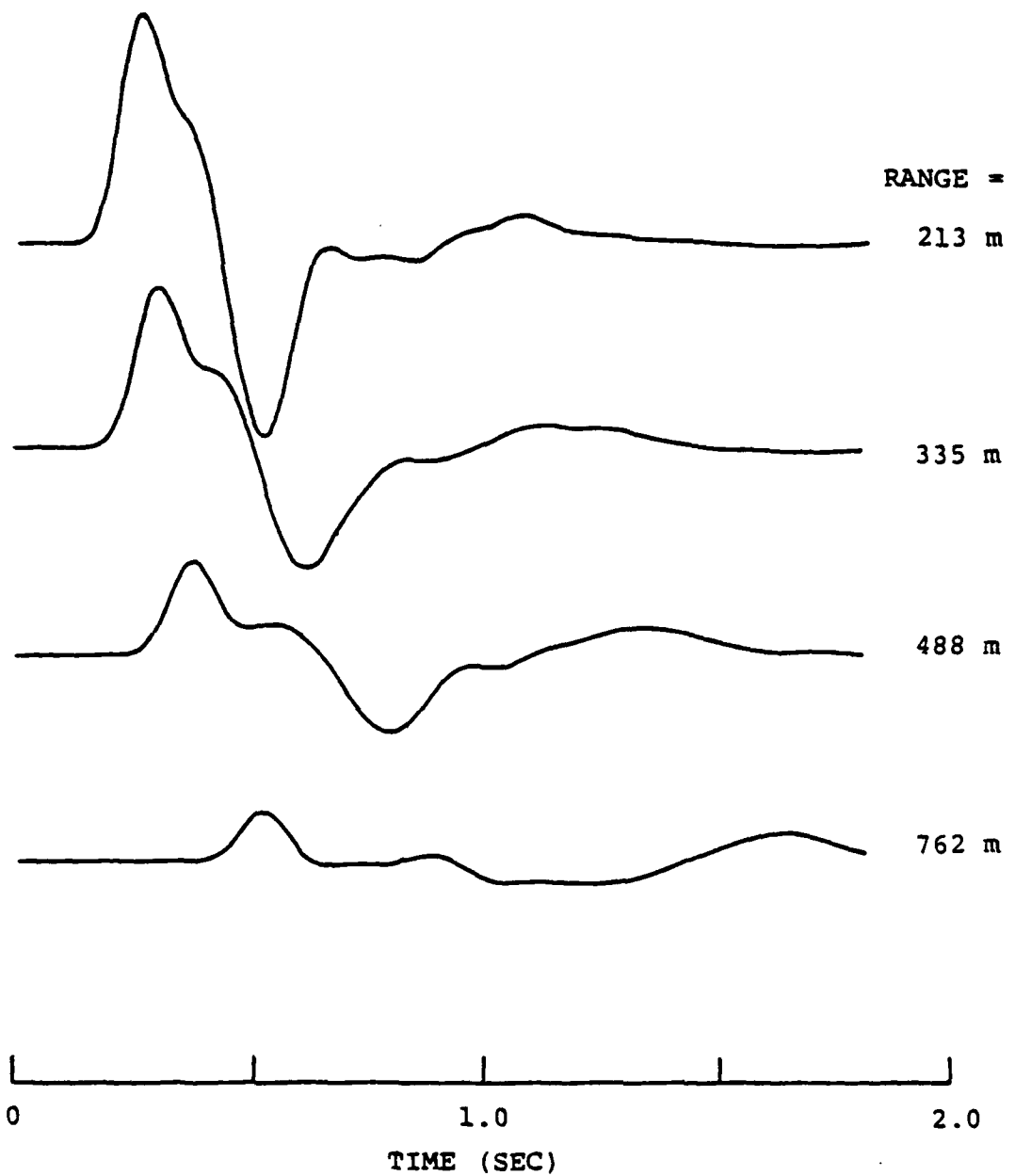
Figure 3.25   Computed Radial Displacements at Shot Level
             Generated by Spall Closure Model II.   Spall
             Closure is Assumed to Occur at Time Equal 0.

132
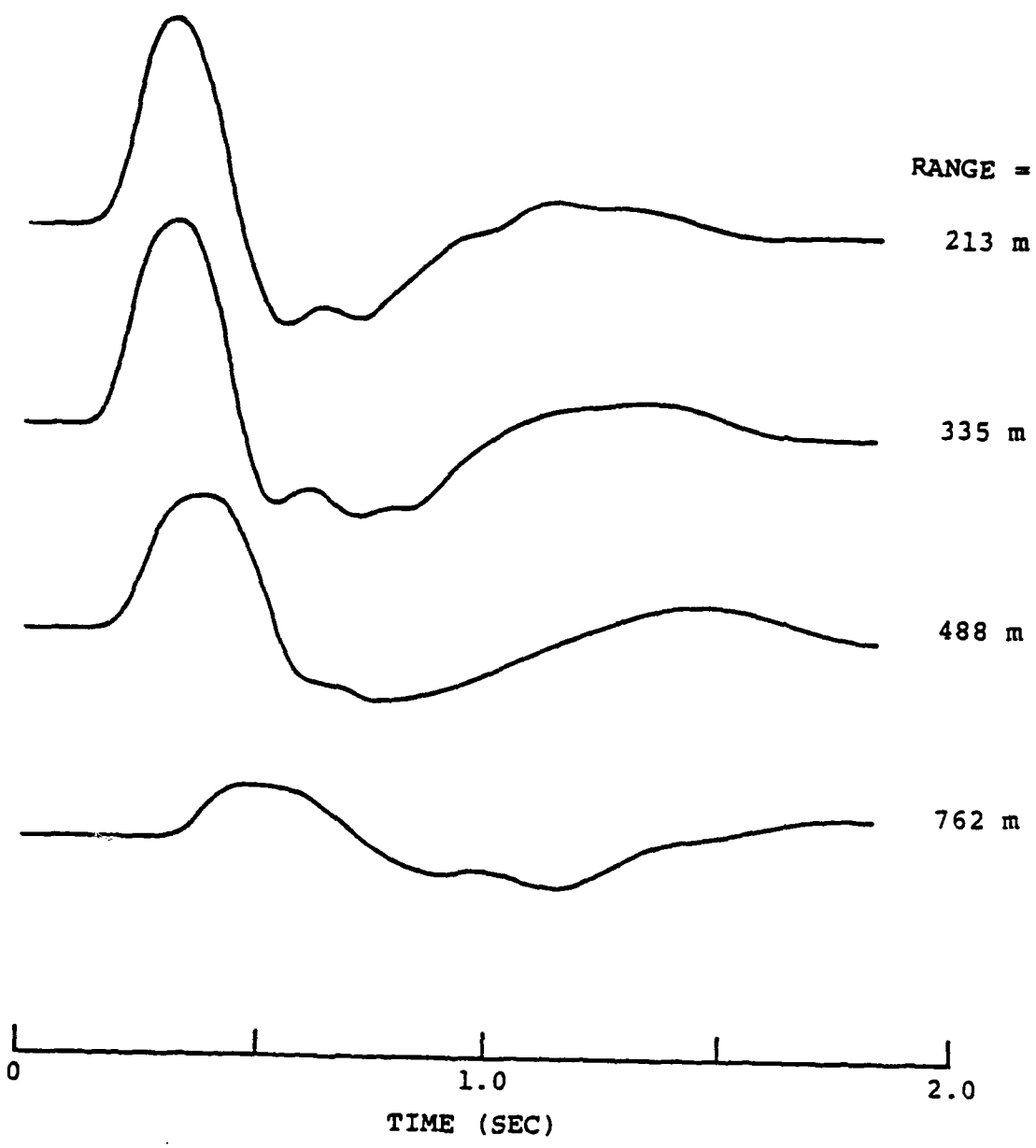
Figure 3.26   Computed Radial Displacements at Shot Level
Generated by Spall Closure Model III. Spall
Closure is Assumed to Occur at Time Equal 0.

133
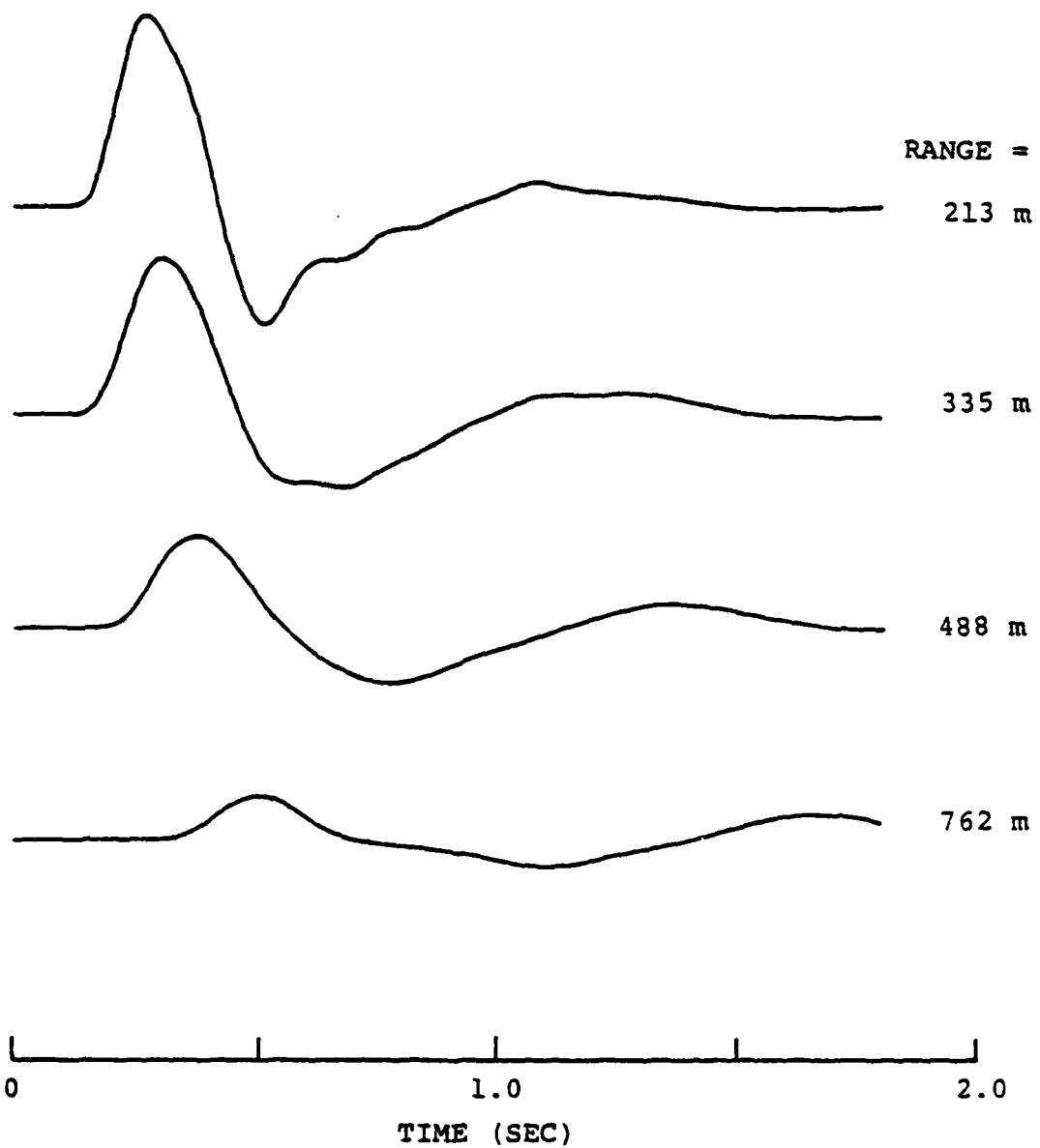
Figure 3.27   Computed Radial Displacements at Shot Level
Generated by Spall Closure Model IV.   Spall
Closure is Assumed to Occur at Time Equal 0.

extent that they consist of an outward motion followed by a rather slowly decaying inward motion. Figure 3.28 is a plot of arrival times of the positive and negative peaks for both Model I and the observations. As Figure 3.28 shows, the apparent velocity of the initial outward phase is correctly replicated in the computed signal. At ranges of 213 m and 335 m, this phase consists of the direct P wave from the spall closure source; and, at ranges of 488 m and 762 m, it is a mixture of direct P and refracted P, with both arriving within a few hundredths of a second of each other.

However, Figure 3.28 demonstrates the inability of our simple model to account for the behavior of the observed negative phase. The observed negative phase travels at precisely the velocity of the initial phase, with a constant delay of about 0.42 seconds, whereas the computed negative phase travels at a lower velocity than the initial phase. The computed negative phase is predominantly a direct S wave generated by the spall closure, complicated by the presence of the Rayleigh wave. (The second positive peak evident in the computation at 488 m and 762 m is the free surface-diffracted phase PS.) The discrepancy between the observed and computed apparent velocity of the negative phase persists for all the models examined; it does not seem to be sensitive to details of the geology or the radius of the spall up to the maximum considered, 300 m. Larger spall radii seem to be precluded by the surface accelerometer data presented by Perret (1971).

Two less serious discrepancies between the data shown in Figures 3.17 through 3.20, and the Model I computation shown in Figure 3.24 are (1) the positive phase is too large relative to the negative phase in the computed signals, and (2) relative peak-to-peak amplitudes among the four free field stations are poorly modeled -- i.e. the observed peak-to-peak amplitudes are nearly identical at 213 m, 335 m and 488 m, and the amplitude
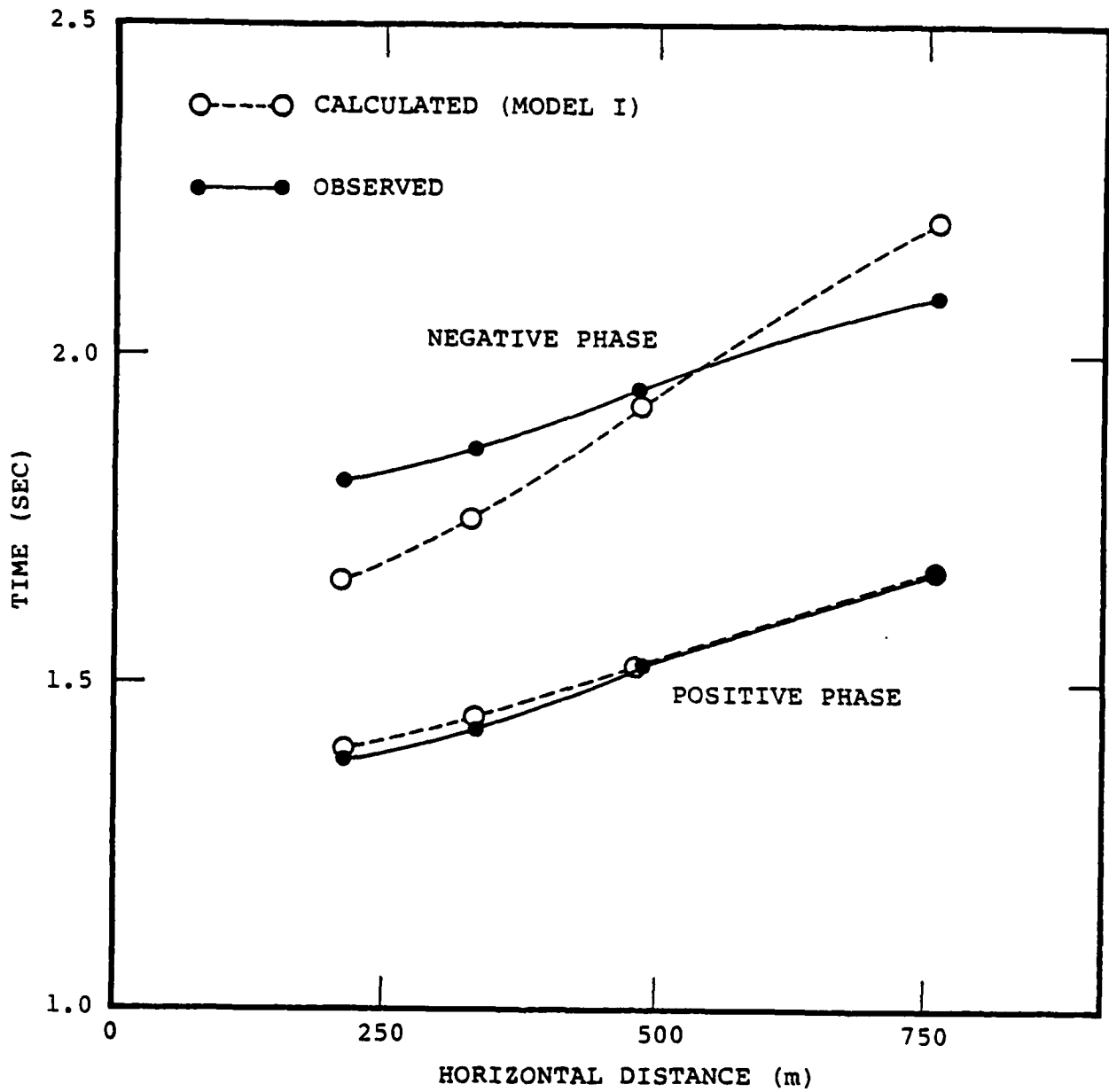
Figure 3.28   Comparison of Arrival Times of Positive and
Negative Peaks Computed for Model I with
Observations for the Low-Frequency, Late-Time
Phase from Merlin.

136

at 762 m is actually higher, whereas the computed signal decays slowly but uniformly with distance. The first discrepancy was improved slightly for the calculations in which the impact velocity of the spall decreased with radial distance (Models II and IV). Figure 3.29 compares the displacements at a range of 335 m for Models I and II. The improvement in relative amplitude for Model II is small, but occurs consistently at all but the most distant station (762 m).

The second discrepancy was substantially improved in the case of Model III, in which r_0 was increased to 300 m and impact velocity kept uniform. In that case, the peak-to-peak amplitude is nearly identical among the stations at 213 m, 335 m and 488 m (Figure 3.26). The large amplitude observed at 762 m cannot be replicated, however, without even further increasing the spall radius. As pointed out earlier, larger spall radii are apparently ruled out by the surface acceleration data.

As a compromise between fitting the various amplitude data and selecting a physically plausible model, Model IV (Figure 3.27) is preferred. It is successful to the extent that first arrival times are correct, amplitudes at the near stations are reasonable, and the pulse shapes roughly resemble the observed pulses. It is physically acceptable in that the spall radius does not exceed the 300 m permitted by the surface observations, the initial spall momentum is conically distributed with respect to radius, and the total spall momentum is within slightly more than a factor of two of that inferred from Viecelli's empirical curves.

In attempting to match the Merlin data some shortcomings of the model persist, however. First, the apparent velocity of the negative phase is too low in the synthetics. Second, the amplitude at the most distant station (762 m) is an order of magnitude too low in the synthetics. We have been unable to account for these two features of the data with our simple models.
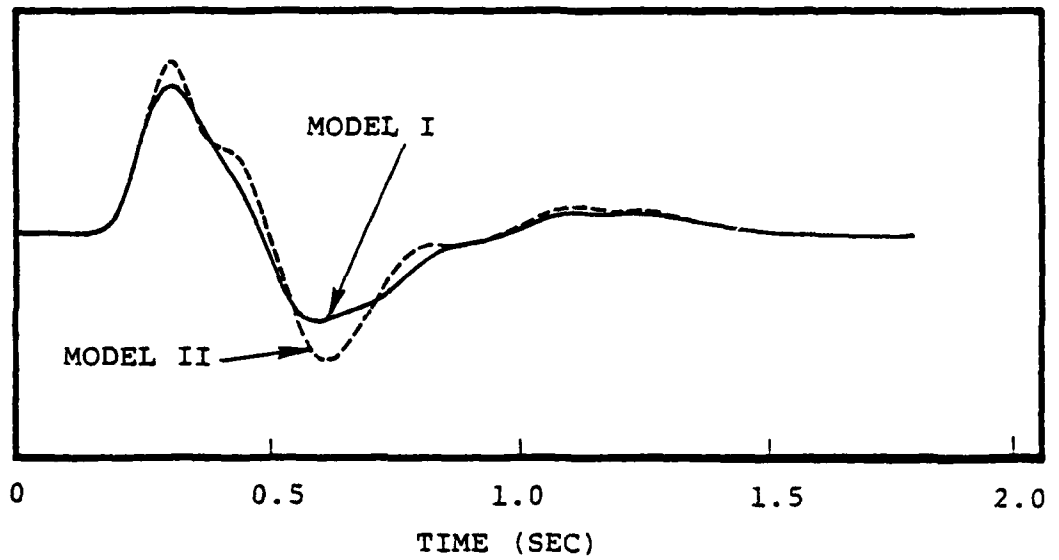
137

Figure 3.29   Comparison of the Radial Displacement Time
Histories at a Range of 335 m Computed for
Models I and II.

138

Third, the negative phase in the synthetics is consistently too small relative to the positive phase. This feature seems to have some sensitivity to details of the model, and we might expect to improve the synthetic waveforms in this respect with more experimentation.

Since the observed pulse behaves much like a plane wave, its shape and amplitude being almost invariant with distance, our modeling has relied on fortuitous phase interference in order to match the data with a local source, with only partial success. Either a more complex representation of the spall closure mechanism is needed, or a physical mechanism other than spall closure is contributing to the observed motion. In fact, the surface ground motions (cf. Figure 3.18) are indicative of a more complex spall closure physics than has been modeled here.

Therefore, considering that even a simple spall closure model adequately explains several features of the observed late-time ground motion for the Merlin event, it seems reasonable to conclude that spall closure is the probable cause of such motion. However, additional study is needed to discern details of the spall closure mechanism as well as other potential mechanisms which could contribute to such motion.

139

IV.   SUMMARY AND RECOMMENDATIONS FOR FURTHER STUDY

The investigation summarized in this report has centered
on the collection and organization of the available free-field
ground motion data from U.S. nuclear tests emplaced in alluvium,
tuff, dolomite, sandstone-shale and interbedded lava flows.
The primary objective of the study has been to reformat the
published data into a homogeneous form which will serve as a
useful reference for researchers who are attempting to define
theoretical seismic source functions for contained explosions
in these media.

In Chapter II the available free-field data were summarized
for 13 events: the Fisher, Hognose, Haymaker, Merlin, Hupmobile
and Packard events in alluvium; the Rainier, Mud Pack and Discus
Thrower events in tuff; the Handcar event in dolomite; the Gas-
buggy event in sandstone-shale; and the Milrow and Cannikin
events in interbedded lava flows. Subsurface geologic profiles
were presented for each event to illustrate the environment in
which the measurements were made. A total of 53 RDP's were
presented: 14 for sources in alluvium, 24 for sources in tuff,
11 for the source in dolomite and four for the source in sandstone-
shale. Many of these RDP's were affected by arrivals from the
media boundaries and therefore only approximate free-field
motions. Certain others appeared to be derived from measure-
ments within the strongly inelastic region and would not accur-
ately represent the radiated seismic field.

Chapter III presented a closer look at the free-field data
for the Handcar, Discus Thrower and Merlin events in an effort
to discern additional information about the seismic source
characteristics of these events. As a result of these studies,
we found that the free-field data for the dolomite event,

Handcar, were consistent with low seismic (i.e. m_b) coupling efficiency and the corresponding small cavity radius observed for the event. Free-field ground motion from Discus Thrower could be reasonably explained by elastic wave propagation theory and showed little evidence of significant nonlinear effects due to proximity of the source to the tuff-Paleozoic boundary. A late time, low frequency signal on the free-field records for Merlin appeared to be caused by spall closure though simple analytic models were not able to fully explain the observations.

In the course of our investigations we have identified some additional "free-field" data which have not been published though ground motion records exist. These data could serve to supplement the rather meager free-field data base for certain emplacement media. It is therefore recommended that these data be collected and put into a format consistent with these first two reports. We further recommend that additional efforts be expended in the analyses of the problems described in Chapter III. Additional "free-field" data bearing on the problems of non-linear effects at media interfaces and spall closure signals should be identified and subjected to detailed analyses to determine their significance to seismic signals at regional and tele-seismic distances.

REFERENCES

Boardman, C. R., G. L. Meyer, and D. D. Rabb, 1966, "Macro-deformation Resulting From the Handcar Event," UCRL-50149.

Day, J. D. and M. A. Vispi, 1969, "Free-Field and Surface Ground Motion Measurements, Project 1.1b/1.2b, Operation Flint Lock, Discus Thrower Event," POR-6401.

Eisler, J. and F. Chilton, 1964, "Spalling of the Earth's Surface by Underground Nuclear Explosions," J. Geophys. Res. 69, 5285.

Frazier, G. A. and C. M. Petersen, 1974, "3-D Stress Wave Code for the ILLIAC IV," Systems, Science and Software Report SSS-R-74-2103.

Haskell, N. A., 1967, "Analytic Approximation for the Elastic Radiation From a Contained Underground Explosion," J. Geophys. Res. 72, 2583.

Murphy, J. R., 1978, "A Review of Available Free-Field Seismic Data From Underground Nuclear Explosions in Salt and Granite," CSC-TR-78-0003.

Perret, W. R., 1961, "Subsurface Motion From a Confined Underground Detonation - Part I, Project 26.4b, Operation Plumbbob, Rainier Event," WT-1929.

Perret, W. R., 1965, "Ground Motion Near Nuclear Explosions in Desert Alluvium, Projects 1.1 and 1.2, Vela Uniform Program, Operation Nougat, Fisher, Ringtail, Hognose and Haymaker Events," VUF-2000.

Perret, W. R., 1970a, "Gasbuggy Seismic Source and Surface Motion," Plowshare Program, Gasbuggy Event," PNE-1002.

Perret, W. R., 1970b, "Ground Motion in a Multilayered Earth, Part I, Nuclear Explosion in Hardrock, Project 1.1/1.2, Operation Whetstone, Handcar/Painted Pony Event," POR-2800.

Perret, W. R., 1970c, "Ground Motion in a Multilayered Earth, Part II, Nuclear Explosion in Tuff, Project 1.1/1.2, Operation Whetstone, Mud Pack Event," POR-2900.

Perret, W. R., 1971, "Free-Field and Surface Motion From a Nuclear Explosion in Alluvium: Merlin Event," SC-RR-69-334.

REFERENCES (Cont'd)

Perret, W. R., L973, "Ground Motion in the Vicinity of the Cannikin Nuclear Explosion," SLA-73-0043.

Perret, W. R. and R. C. Bass, 1975, "Free-Field Ground Motion Induced by Underground Explosions," SAND-74-0252.

Perret, W. R. and D. R. Breding, 1972, "Ground Motion in the Vicinity of an Underground Nuclear Explosion in the Aleutian Islands: Milrow Event," SC-RR-71-0668.

Perret, W. R. and K. B. Kimball, 1971, "Ground Motion Induced by a Contained Nuclear Explosion, Project 1.1a/1.2a, Operation Flint Lock, Discus Thrower Event," POR-6400.

Preston, R. G. and V. E. Wheeler, 1969, "Response of the Line-of-Sight Pipe to Ground Shock in the Hupmobile Nuclear Effects Test," UCRL-50662.

Viecelli, J., 1973, "Spallation and the Generation of Surface Waves by an Underground Explosion," J. Geophys. Res. 78, 2475.

Werth, G. C. and R. F. Herbst, 1962, "Comparison of Amplitudes of Seismic Waves From Nuclear Explosions in Four Media," UCRL-6962.

Wheeler, V. E. and R. G. Preston, 1971, " Response of the Pipe and Ground in the Packard Nuclear Effects Test," UCRL-51112.